Diese Dissertation haben begutachtet:

_____ _____

DISSERTATION

THE INTERACTION OF HIGHLY CHARGED IONS WITH INSULATING MATTER: CAPILLARY GUIDING AND RELATED PHENOMENA

ausgeführt zum Zwecke der Erlangung des akademischen Grades eines
Doktors der technischen Wissenschaften
unter der Leitung von

Univ. Prof. Dr. Friedrich Aumayr
E134
Institut für Angewandte Physik

eingereicht an der
Technischen Universität Wien

Fakultät für Physik

von
Dipl.-Ing. Gregor Kowarik
Matr.Nr. 0026333
Liechtensteinstraße 24/6a, A-1090 Wien

Wien, am 28. Juni 2011 _____

KURZFASSUNG

Die vorliegende Arbeit beschäftigt sich mit der Wechselwirkung von (ein- und mehrfach geladenen) Ionen mit Oberflächen. Das betrachtete Energie-regime reicht dabei von etwa 100 eV bis zu einigen 10 keV, sowohl was die kinetische, als auch die potentielle Energie der Ionen anlangt. Dabei versteht man unter der potentiellen Energie von Ionen im Wesentlichen die Summe der Ionisationsenergien, die notwendig war um den endgültigen Ladungszustand des Ions zu erreichen. Diese kann, im Fall von hoch geladenen Ionen, durchaus einigen 10 keV ausmachen und die kinetische Energie in den betrachteten Fällen auch übertreffen.

Besonderes Augenmerk der Arbeit liegt auf der Untersuchung des 2002 erstmals in der Literatur erwähnten „capillary guiding" Effektes, der sich kurz wie folgt zusammenfassen lässt: Trifft ein geladenes Teilchen, in diesem Fall ein mehrfach geladenes Ion, unter einem Kippwinkel auf eine isolierende Kapillare, wird es vor dem Auftreffen auf die innere Oberfläche neutralisiert. Bei diesem Prozess verbleibt eine Nettoladung an der Oberfläche, die erst allmählich durch Ladungstransport abgebaut werden kann. Nachfolgende Projektile werden von dem erzeugten elektrischen Feld abgelenkt und treffen an einer anderen Stelle auf die Oberfläche. Es zeigt sich nun, dass in einer Art selbstorganisiertem Prozess, Ladungsansammlungen entstehen, die letzten Endes zur Transmission der Projektile durch die Kapillare führen. Interessanter Weise, zeigen die mehrfach geladenen Primärteilchen nach dem Durchtritt durch die verkippte Kapillare noch immer den gleichen Ladungszustand wie zu Beginn, was eindeutig zeigt, dass die transmittierten Ionen nie in direkten Kontakt mit der inneren Oberfläche der Kapillare gekommen sind. Die ursprünglichen Arbeiten verwendeten dabei Nano-Kapillaren, d.h. eine große Zahl an parallelen ‚Röhren' durch eine PET-Folie, mit Durchmessern in der Größenordnung von 100 nm.

In dieser Arbeit liegt das Augenmerk nun auf makroskopischen Kapillaren, also einem einzelnen Glasröhrchen, etwa 1 cm lang. Dabei wird der fundamentale Guiding Prozess untersucht und anschließend der Möglichkeit nachgegangen, die Stärke des Guidings zu verändern, indem die Leitfähigkeit des Materials variiert wird. Dies geschieht durch Temperaturänderung innerhalb eines Bereiches von rund 100°C, die, wie sich letztendlich herausstellte, den Guiding Effekt massiv beeinflusst.

Neben dem Effekt des Capillary Guiding, werden in dieser Arbeit verschiedene weitere Aspekte der Wechselwirkung von Ionen mit Oberflächen untersucht. Dabei liegt ein Fokus auf der beschussinduzierten Emission von Elektronen für verschiedenste Projektile, sowie dem möglicherweise interessantesten Anwendungsfall für den „Capillary Guiding Effect", der Erzeugung von wohldefinierten Defekten an einer Oberfläche durch den Beschuss mit hoch geladenen Ionen. Vor kurzem wurde diesbezüglich entdeckt, dass Ionen, die eine ausreichend hohe potentielle Energie durch entsprechend hohe Ladungszustände tragen, einzelne Defekte an Oberflächen erzeugen können, die möglicherweise für lithographische Zwecke verwendet werden können. Die Besonderheit liegt hierbei auf der Vermeidung von Stoßkaskaden in der Probe, da sehr langsame Ionen verwendet werden könne. Schließlich könnten sich nach vorne verjüngende Glaskapillaren ein nützliches Werkzeug sein, um einen entsprechend hoch geladenen Ionenstrahl direkt auf einer Probe zu platzieren.

ABSTRACT

This work deals with the interaction of (singly- and multiply-charged) ions with surfaces. The respective energy regime, kinetic and potential, respectively, ranges from about 100 eV up to several 10s of keV. Potential energy, in this respect, is equivalent to the sum of ionisation energies, spent to ionise the ion to its final charge-state. This potential energy can reach considerable values of more than 10 keV for highly charged ions, even higher than the kinetic energy.

This work especially focuses on the so-called capillary guiding effect, first mentioned in the literature in 2002. This effect can be understood by the following simple description: Whenever a charged particle impinges a capillary, which is tilted with respect to the beam axis, it becomes neutralised when hitting the inner surface. Thus, the missing electrons at the surface cause a net positive charge remaining at the impact site. In an insulator, the weak charge transport causes these charges to remain at the surface for some time. During this period, following projectiles are being deflected by the remaining electric field and hit the surface at a slightly different position. It turns out, charge-patches are forming in a self-organised way, such that the beam is eventually transmitted. Interestingly, multiply charged ions (to large extent) do not undergo any charge exchange, thus are transmitted in their initial charge-state. This shows, that the transmitted projectiles do not get into close contact to the inner wall of the capillary. Pioneering work has been done using nano-capillaries, i.e. a large number of parallel 'tubes' through a PET foil, with diameters in the 100 nm regime.

In this work, however, the focus lies on macroscopic capillaries, thus, a single glass tube, about one cm long. The fundamental process of guiding is investigated and especially the question, whether this effect can be varied in its strength by changing the material's conductivity. This is done via variation of the temperature within a range of about 100°C. Finally it turned out, that this variation has major impact onto the guiding phenomenon.

Besides the guiding effect, other aspects of the interaction between ions and surfaces are investigated as well. One important phenomenon is electron emission upon ion impact, or the creation of well-defined surface defects due to the interaction with highly-charged ions. The latter could well lead to an interesting application for the capillary guiding effect, due to the possibility using tapered capillaries with a very small outlet diameter to position the ion beam precisely. It was only recently, one has found, that the high potential energy carried by a highly-charged ion can lead to the formation of a single defect on the surface at each individual impact site. Depending on the sample material, this defects can be of a different nature, like holes or hillocks. Such very slow highly-charged ions could possibly be used for lithographic purposes, because of the advantage of producing no collisional cascade in the bulk. As mentioned, a capillary might be a proper tool for such a purpose.

ABBREVIATIONS

ADC	**A**nalogue to **D**igital **C**onverter
AES	**A**uger **E**lectron **S**pectroscopy
AFM	**A**tomic **F**orce **M**icroscopy
BS	**B**ack **S**cattered
CAMAC	**C**omputer **A**utomated **M**easurement **A**nd **C**ontrol
CM	**C**ontact **M**ode
EBIS	**E**lectron **B**eam **I**on **S**ource
EBIT	**E**lectron **B**eam **I**on **T**rap
ECRIS	**E**lectron **C**yclotron **R**esonance **I**on **S**ource
EE	**E**lectron **E**mission
GANIL	**G**rand **A**ccélélerateur **N**ational des **I**ons **L**ourdes
FFT	**F**ast **F**ourier **T**ransformation
HCI	**H**ighly **C**harged **I**on
HV	**H**igh **V**oltage
MCI	**M**ultiply **C**harged **I**on
MCP	**M**ulti **C**hannel **P**late
MIM	**M**etal-**I**nsulator-**M**etal Junction
PC	**P**ersonal **C**omputer
PET	**P**oly**E**thylene-**T**erephtalate
PIPS	**P**assivated **I**mplanted **P**lanar **S**ilicon (Detector)
PSD	**P**osition **S**ensitive **D**etector
PSV	**P**lasma **S**heath **V**oltage
SCSI	**S**mall **C**omputer **S**ystem **I**nterface
SE	**S**econdary **E**lectrons
SPM	**S**canning **P**robe **M**icroscopy
STM	**S**canning **T**unnelling **M**icroscopy
UHV	**U**ltra **H**igh **V**acuum
XPS	**X**-Ray **P**hotoelectron **S**pectroscopy

"I wonder if I shall fall right through the earth!
How funny it'll seem to come out
among the people that walk
with their heads downward!"

Alice to herself in

Alice's Adventures in Wonderland
by Lewis Carroll, 1865

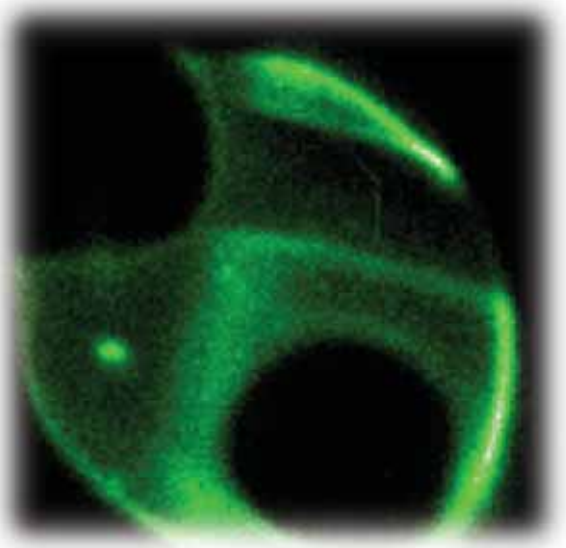

this was the last image obtained with our position-sensitive-particle-detector in its lifetime. R.I.P.

the alien is watching you…

TABLE OF CONTENTS

PREFACE

The presented work has been conducted under supervision of Prof. Friedrich Aumayr in his group at the Institute of Applied Physics (formerly General Physics) at Vienna University of Technology (Technische Universität Wien) in the years from 2008 until 2011.

During this time, several students have contributed to this work by means of Diploma(Master) theses, Bachelor theses, or project works, which is summarised right below. All of them were supervised by Prof. Friedrich Aumayr at the Institute of Applied Physics (formerly General Physics).

The work described in part II of this thesis was performed in collaboration with a Hungarian group. Réka Bereczky, a graduate student from ATOMKI Debrecen, produced the glass tubes, which were used in our experiment and also participated in several of the measurements performed in Vienna. She also helped with the preliminary evaluation of the experimental data together with Friedrich Ladinig.

Diploma Theses

- **Michael Brunmayr**
  Experimentelle Untersuchungen zur ioneninduzierten Elektronenemission aus Kernfusions-relevanten Oberflächen, 2008
- **Christopher Andrew Vasko**
  Systematic study of nano-structures on polymethyl-methacrylate induced by slow highly charged ions, 2009
- **Kai Iskratsch**
  New Design of an Ion Source Control Software and Investigations of Ion-Induced Electron Emission from LiF, 2009
- **Elisabeth Gruber**
  (Capillary Guiding), in progress

Bachelor Theses

- **Elisabeth Gruber**
  Experimentelle Untersuchung ioneninduzierter Elektronenemission von Isolatoren, 2009
- **Martin Thalhammer**
  Konstruktion einer Feldemissions-Elektronenquelle zur Untersuchung von Elektronen-guiding an metallischen Kapillaren, 2009
- **Sarah Gumpenberger**
  Irradiation of pmma-samples with singly and multiply charged argon ions through a µm-structure mask, 2009
- **Ralf Brüstl**
  AFM study of highly charged ion irradiation damage on PMMA-surfaces, 2009
- **Wilfried Mach**
  Technische Verbesserung einer Feldemmisions-Elektonenquelle zur Untersuchung von Elektronen-Guiding an metallischen Kapillaren, 2010
- **Robert Raab**
  Transmission von hochgeladenen Ionen durch Kapillaren, 2010
- **Roman Kreuzhuber**
  Elektronenemission von Isolatoren: Elektronenemissionsausbeute von LiF mit H^+- und H_2^+-Projektilen, 2010

- **Andreas Wartak**
  Conceptual Design and Sample Preparation of Electrode Covered Single Glass Macro-Capillaries for Ion Transmission Experiments, 2011
- **Friedrich Ladinig**
  Temperature dependence of ion guiding, in progress

Project Students / Internships:

- Alexander Fuchs-Fuchs (in progress)
- Benedikt Würkner (in progress)
- Jakob Anger (in progress)
- Armand Macé (2010)
- Romain Le Picard (2010)
- Fabian Germ (2010)
- Coline Lemaignan (2009)
- Josef Kamleitner (2009)

Publications

Parts of the present work have been published in international journals [1-13]:

- D. Kovacs, A. Golczewski, **G. Kowarik**, F. Aumayr, D. Diesing;
  "Low-energy ion-induced electron emission in metal-insulator-metal sandwich structures"
  Physical Review B 81 (2010) 075411
- R. Ritter, **G. Kowarik**, W. Meissl, A.S. El-Said, L. Maunoury, H. Lebius, C. Dufour, M. Toulemonde, F. Aumayr;
  "Nanostructure formation due to impact of highly charged ions on mica",
  Vacuum, 84 (2010) 1062 - 1065
- J. Lörincik, Z. Sroubek, M. Brunmayr, **G. Kowarik**, F. Aumayr;
  "Kinetic electron emission due to perpendicular impact of carbon ions on tungsten"
  Applied Surface Science, 255 (2009) 6303 - 6307
- **G. Kowarik**, R. J. Berecky, F. Aumayr, K. Tökési
  "Production of a microbeam of slow highly-charged ions with a single microscopic glass capillary"
  Nuclear Instruments and Methods in Physics Research Section B, 267 (2009) 2277 - 2279
- R. Bereczky, **G. Kowarik**, F. Aumayr, K. Tökési
  "Transmission of 4.5 keV Ar^{9+} ions through a single macroscopic glass-capillary"
  Nuclear Instruments and Methods in Physics Research Section B, 267 (2009), p. 317 - 320
- **G. Kowarik**, M. Brunmayr, F. Aumayr
  "Electron emission from tungsten induced by slow, fusion-relevant ions"
  Nuclear Instruments and Methods in Physics Research Section B, 267 (2009), 2634 - 2637
- S. Markin, D. Primetzhofer, S. Prusa, M. Brunmayr, **G. Kowarik**, F. Aumayr, P. Bauer
  "Electronic interaction of very slow light ions in Au: Electronic stopping and electron emission"
  Physical Review B 78 (2008) 1951221 – 1951226
- **G. Kowarik**, E. Gruber, K. Iskratsch and F. Aumayr
  "Using a current method for measuring ion-induced electron emission from LiF"
  Nuclear Instruments and Methods in Physics Research B, 269 (2011), 964 - 967
- R. Ritter, **G. Kowarik**, W. Meissl, L. Süss, L. Maunoury, H. Lebius, C. Dufour, M. Toulemonde, and F. Aumayr
  "Nano-structure formation due to impact of highly charged ions on HOPG"
  Nuclear Instruments and Methods in Physics Research B 268 (2010) 2897 – 2900
- R. Ginzel, S. G. Higgins, P. Mrowcynski, P. Northway, M. C. Simon, H. Tawara, J. R. Crespo López-Urrutia, J. Ullrich, **G. Kowarik**, R. Ritter, W. Meissl, C. Vasko, C. Gösselsberger, A. S. El-Said, and F. Aumayr
  "A deceleration system at the Heidelberg EBIT providing very slow highly charged ions for surface nanostructuring"
  Nuclear Instruments and Methods in Physics Research B 268 (2010) 2972 – 2976

- W. Meissl, R. Ginzel, R. Heller, A. S. El-Said, **G. Kowarik**, C. Vasko, C. Gösselsberger, R. Ritter, B. Solleder, M. Simon, S. Facsko, J. R. Crespo López-Urrutia, C. Lemell, R. M. Papaléo, W. Möller, J. Ullrich, J. Burgdörfer, and F. Aumayr
  „Potential energy - induced nanostructuring of insulator surfaces by impact of slow, very highly charged ions“
  Journal of Physics: Conference Series 194 (2009), 132027
- T. Peters, C. Haake, D. Diesing, D. Kovacs, A. Golczewski, **G. Kowarik**, F. Aumayr, A. Wucher, M. Schleberger
  "Hot electrons induced by slow multiply charged ions“
  New Journal of Physics 10 (2008) 0730191 – 0730198
- **G. Kowarik**, C. Vasko, C. Gösselsberger, R. Ritter, W. Meissl, A.S. El-Said, F. Aumayr, R. Ginzel, M. Simon, J.R. Crespo López-Urrutia, R. Ullrich, R. Heller, S. Facsko, R. Papaléo, W. Rupp, L. Maunoury, C. Dufour, H. Lebius, M. Toulemonde
  "Nanostructures on surfaces induced by slow highly charged ions"
  Book of Reports, 19th International Conference on Ion Surface Interactions, (2009) 159 – 164
- R. J. Bereczky, **G. Kowarik**, C. Lemaignan, F. Aumayr, and K. Tökési
  "Transmission of 4.5 keV Ar^{9+} ions through a single glass macrocapillary“
  Journal of Physics: Conference Series 194 (2009) 132019
- S. Facsko, W. Meissl, R. Heller, R. Wilhelm, A. S. El-Said, **G. Kowarik**, R. Ritter and F. Aumayr
  "Nanostructures induced by highly charged ions on CaF2 and Kbr“
  Journal of Physics: Conference Series 194 (2009) 012060

Talks

- Invited Talk: G. Kowarik, C. Vasko, C. Gösselsberger, R. Ritter, W. Meissl, A.S. El-Said, F. Aumayr, R. Ginzel, M. Simon, J.R. Crespo López-Urrutia, R. Ullrich, R. Heller, S. Facsko, R. Papaléo, W. Rupp, L. Maunoury, C. Dufour, H. Lebius, M. Toulemonde, „Nanostructures on surfaces induced by slow highly vharged ions“, 19th International Conference on Ion Surface Interactions (ISI), Zvenigorod/Russian Federation, 24.8.2009
- Invited Talk: G. Kowarik, "Charged particle guiding through macroscopic capillaries", 2nd Symposium on Ion-Insulator-Interactions (S3I), Platja d'Aro, Girona/Spain, 21.5.2009
- Short Oral: G. Kowarik
  "Tuning the efficiency of capillary guiding"
  7th Intern. Symposium on Atomic Level Characterizations for New Materials and Devices, (ALC'11), Seoul, Republic of Korea 26.05.2011
- Talk: G. Kowarik; „The effect of electrical conductivity on guiding of slow highly charged ions through mesoscopic glass capillaries“; 15th international conference on the physics of highly charged ions (HCI 2010); Shanghai/China; 30.08.2010
- Talk: G. Kowarik; „The effect of temperature on guiding of slow highly charged ions through mesoscopic glass capillaries“; 24th Intern. Conf. on Atomic Collisions in Solids (ICACS 24), Krakow/Poland, July 20th
- Talk: G. Kowarik, „The response of an insulating surface to the impact of slow highly charged ions“; SFB616 Summer school „Energy dissipation at surfaces“, Essen/Germany; 28.09.2009
- Talk: G. Kowarik, „The influence of external electric fields onto capillary guiding - ITS LEIF beam time proposal P09076A“; 4th Annual Meeting of the EU network ITS-LEIF, Platja d'Aro, Girona/Spain; 17.05.2009
- Talk: G. Kowarik, „Transmission of highly charged ions through a single glass capillary“; WTZ/KONTAKT Seminar, TU Wien, Vienna, Austria; 11.11.2008

Poster presentations at international conferences

- Poster: G. Kowarik, R.J. Bereczky, F. Ladinig, K. Tökesi, and F. Aumayr
  "Tuning the efficiency of capillary guiding"
  7th Intern. Symposium on Atomic Level Characterizations for New Materials and Devices, (ALC'11), Seoul, Republic of Korea 26.05.2011
- Poster: F. Aumayr, R. Ritter, G. Kowarik; „Highly charged ion-induced surface nanostructures“; 15th International Conference on the Physics of Highly Charged Ions (HCI-2010) Fudan University, Shanghai, China, 30.08.2010
- Poster: G. Kowarik, R. J. Bereczky, A. Macé, F. Ladinig, R. Raab, K. Tőkési, and F. Aumayr; „The effect of electrical conductivity on guiding of slow highly charged ions through mesoscopic

glass capillaries“; 15th International Conference on the Physics of Highly Charged Ions (HCI-2010) Fudan University, Shanghai, China, 30.08.2010

- Poster: G. Kowarik, E. Gruber, K. Iskratsch, and F. Aumayr; „Using a current method for measuring ion induced electron emission from LiF“; 24th Intern. Conf. on Atomic Collisions in Solids (ICACS 24), Krakow/Poland, 22.07.2010
- Poster: R. Ritter, G. Kowarik, Q. Shen, C. Teichert, R. Ginzel, J.R. Crespo López-Urrutia, J. Ullrich, L. Maunoury, H. Lebius, M. Toulemonde and F. Aumayr; „Slow highly charged ion irradiation of HOPG“; 24th Intern. Conf. on Atomic Collisions in Solids (ICACS 24), Krakow/Poland, 22.07.2010
- Poster: G. Kowarik, R. J. Bereczky, C. Lemaignan, A. Macé, F. Ladinig, R. Raab, K. Schiessl, C. Lemell, K. Tőkési and F. Aumayr; „Guiding of slow highly charged ions through mesoscopic glass capillaries“; 10th European Conference on Atoms Molecules and Photons (ECAMP X); Salamanca/Spain, 04.07.2010
- Poster: G. Kowarik, R. J. Bereczky, C. Lemaignan, A. Macé, F. Ladinig, R. Raab, K. Tőkési and F. Aumayr; „Transmission of 4.5 keV Ar^{9+} ions through a single glass macrocapillary“; 5th Annual Meeting of the EU network ITS-LEIF, Alghero, Sardinia, Italy, 12.05.2010
- Poster: C. Vasko, C. Gösselsberger, G. Kowarik, R. Ginzel, R. Heller, S.Facsko, L. Maunoury, J.R. Crespo López-Urrutia, R.M. Papaléo, J. Ullrich, W. Möller, M. Toulemonde and F. Aumayr, “Investigation of nanodefects induced by impact of slow highly charged ions on isolators”, ITS LEIF Annual Meeting 2009, Platja d'Aro, Girona/Spain, 20.5.2009
- Poster: G. Kowarik, E. Gruber, K. Iskratsch, F. Aumayr, “Using a current method for measuring ion induced electron emission from LiF”, ITS LEIF Annual Meeting 2009, Platjad'Aro, Girona/Spain, 20.5.2009
- Poster: F. Aumayr, S. Markin, D. Primetzhofer, M. Brunmayr, G. Kowarik, P. Bauer, “Electronic interaction of very slow light ions in Au: Electronic stopping and electron emission”; Symposium on Surface Science 2009 (3S09), St. Moritz/Switzerland; 10.03.2009
- Poster: R. Bereczky, G. Kowarik, F. Aumayr, K. Tökési, "Transmission of 4.5 keV Ar^{9+} ions through a single macroscopic glass-capillary"; 4th Conference on Elementary Processes in Atomic Systems (CEPAS) (2008)
- Poster: F. Aumayr, G. Kowarik and M. Brunmayr; “Electron emission from tungsten induced by slow, fusion-relevant ions”; 23rd Int. Conf. on Atomic Collisions in Solids (ICACS 23), Phalaborwa/South Africa, 19.8.2008
- Poster: F. Aumayr, R. Ritter, W. Meissl, G. Kowarik, L. Süss, L. Maunoury, H. Lebius, C. Dufour, I. C. Gebeshuber, M. Toulemonde Nano-hillock formation due to impact of HCI on lamellar materials 23rd Int. Conf. on Atomic Collisions in Solids (ICACS 23), Phalaborwa/South Africa, 19.8.2008

Awards

The ALC’11 poster award was granted for a poster about the capillary guiding effect:
G. Kowarik
"Tuning the efficiency of capillary guiding"
Poster, 7th Intern. Symposium on Atomic Level Characterizations for New Materials and Devices, (ALC’11), Seoul, Republic of Korea 26.05.2011

General Introduction

The interaction between ions and surfaces is important for technical applications. It has been widely studied in the last century. Yet, there still remain open questions concerning fundamental aspects. Albeit there exists profound knowledge about the interaction of ions with metallic or semiconducting surfaces, insulating target materials have been avoided for a long time, because of their unfavourable charging behaviour under ion impact, leading to erratic, non-reproducible results. But even for metallic surfaces, especially at low projectile velocities, not all processes are well understood.

In this work, the focus lies on several aspects of the interaction between ions and insulators. The main interest is the investigation of the recently discovered capillary guiding effect, which is discussed in part II of this work. Before that, in part I, other fundamental phenomena are looked at. Especially the interaction of highly-charged ions with surfaces is an important technological aspect, due to the possibility of producing nano-metre sized structures on a substrate. This nano-metre patterning is a contribution to possible future lithographic methods, making use of highly-charged ions. In this field, the major benefit stems from the possibly very slow velocity of the projectiles, avoiding any collisional damage of the bulk. But before allowing usage of those ions instead of faster singly-charged ones, the underlying processes have to be understood in detail. Especially the patterning of a photo-resist for later chemical etching of semi-conductors opens the way for future technological applications. We investigated such a typical photo-resist, polymethyl-methacrylate (PMMA), as it is widely used in semiconductor industry.

Furthermore, electron emission, occurring upon ion impact is of fundamental interest, since there are still open questions in the low velocity regime, where classical descriptions fail. These phenomena are also discussed in the first part of this work. An interesting way of reaching low impact velocities lies in the usage of clusters. Another interesting aspect of these clusters and their interaction with a surface is the fact, that one can study the transition from a single atom to the bulk. In this work, we reached impact velocities comparable to a rifle bullet and still observed the emission of electrons upon impact. First impressions are shown and open the way to further investigations.

A more application-oriented approach is started in the second part, where, as already mentioned, capillary guiding is studied. This is an effect, which occurs under certain circumstances, when an ion beam impinges capillaries made of insulating material. Without going into detail, this effect practically allows manipulation of a charged particle beam, especially of multiply charged ions, and could be an interesting future ion optical tool for using in highly-charged-ion lithography.

The various aspects of the interaction between ions and surfaces discussed in part I give an idea of the variety of important fundamental processes. This first part of the thesis tries to give a broad overview, whereas, as mentioned above, the second part then focuses onto more distinctive effects. Albeit the two parts are interlinked, because the more fundamental processes described in the beginning are of importance for the understanding of capillary guiding, they can be read also independently.

Part I: Aspects of Ion-Surface-Interaction

I.1 Interaction of slow ions with a surface – An Overview

Interaction of particles with solids covers a wide range of phenomena. Depending on the particle species and its kinetic and potential energy, completely different interaction mechanisms become predominant.

Among others, an ion interacting with a surface can give raise to lots of possible processes:

- The projectile is either
  - reflected,
  - adsorbed,
  - implanted, or
  - transmitted,
- whereas the target is subject to
  - excitation,
  - defect creation,
  - desorption,
  - sputtering, or
  - the emission of secondary ions and/or clusters, respectively.
- As secondary processes, the emission of
  - photons or
  - electrons can occur or even
  - defect mediated desorption.
- For completeness, also nuclear reactions should be mentioned, as possible processes. But those are irrelevant in this work.

Energies involved in the various processes, i.e. potential and kinetic energy of the projectiles can vary over many orders of magnitude. Primarily, in this work the covered energy ranges from about 100 eV to some 10s of keV, hence practically all mentioned phenomena, except the nuclear reactions and adsorption occur in the presented regime. Adsorption might come into play for the clusters (see chapter I.2.4), which are so slow, that they are believed to land softly on a substrate. In our velocity regime, transmission of projectiles is only possible for thin films and therefore not of direct concern.

The projectiles, when interacting with a solid sample, deposit their energy in a variety of processes, which, according to [14], can be split into 5 groups:

1. Excitation and ionisation of target electrons,
2. Projectile excitation,
3. Electron capture,
4. Recoil losses ('nuclear stopping'), and
5. Electromagnetic radiation.

Depending on the projectile species, different mechanisms dominate the losses. For electrons, e.g., just the processes 1, 4, and 5 are relevant. For light ions, however, except for the very low impact velocity regime, process 1 dominates in the velocity range considered in this work. Especially for massive projectiles in the very low velocity regime, nuclear stopping gains importance.

In general, when we refer to slow particles, this refers to the projectile velocity v_P regime below the characteristic electron velocity, which is of the order of 1 a.u. ~ 2.1877 10^6 m/s, corresponding to projectile energies of less than about 25 keV/amu. When looking at solid samples, the Fermi velocity v_F represents the characteristic electron velocity, thus $v_P < v_F$.

This chapter is divided into two larger sections, one dealing with the effect of electron emission due to impact of ions (singly-charged, multiply-charged, cluster-ions), and a shorter one about surface modifications due to the interaction with highly charged ions (HCI).

I.2 Electron Emission

I.2.1 Overview

Particle impact induced electron emission is a phenomenon, which has been known for more than a century (see e.g. [15, 16] for topical reviews). The emission of electrons can be driven by the impact of particles, e.g. electrons, ions or neutral atoms, or other kinds of energetic interactions, like with photons. The emitted electrons carry information about the sample and the projectile as well. That is why various electron spectroscopy methods are standard analytic techniques in surface- and solid-state-science and provide valuable analysis possibilities.

From a fundamental point of view, the interaction of electrons or photons with the electrons in a solid sample is rather well understood. For fast particles, and conductive samples, also the interaction of ions and solids is well described (see e.g. [14, 16]). In contrast, the interaction of slow ions with solids, especially with insulators, still gives rise to some questions. In the very low velocity regime, the exact nature of the involved processes becomes more important, whereas at higher projectile velocities they can be treated as a mean energy loss due to direct collisions with the sample's free electrons.

One of the involved phenomena is electron emission, which sometimes even occurs at projectile energies, where from classical descriptions no such emission should be possible (see e.g. [9, 10, 17, 18] and references therein). Electron emission is of fundamental interest in a variety of applications, e.g. plasma-screens, micro-channel-plates (MCP) or other converters for detection of particles, or as an important contribution to be considered in fusion plasmas interacting with the inner wall of a Tokamak [19]. Also in surface analysis, electron emission is an important effect, which some techniques are based on (see above). Here, one might especially mention the recent development of an Helium-ion-Microscope [20], which uses ion induced electron emission as a key for ultra-high resolution imaging of surfaces.

Electron emission can be quantified by looking at the total electron emission yield γ, defined as the number of electrons emitted per incident event. This can be extended to the differential yield $\frac{d\gamma}{d\Omega dE}$, containing information about the emission solid angle $d\Omega$ and energy element dE. In our investigations, we are usually measuring the total electron emission yield

$$\gamma = \int_0^\infty \int_{2\pi} \frac{d\gamma}{d\Omega dE} d\Omega dE. \quad (1)$$

While the majority of publications on electron emission in the past deals with conductive targets, nowadays the investigation of insulating materials is getting more and more into the focus of several research groups (see e.g. [8, 21-26] and references therein). There, the experimental difficulties due to surface charging are still a strong limitation and the reason, why in this field still many questions are open. Driven by the growing importance of charged particle beams interacting with insulating materials, we investigated several different aspects, including also capillary guiding (see part II of this work) and, related to that, nano-structuring of insulating samples (see section I.3) in a large range of kinetic and potential projectile energies. The fundamental mechanisms of electron emission, therefore, differ between the various investigations, as discussed in the next section.

I.2.2 What drives electron emission?

Electron emission from solids can have a number of reasons. In principle, any kind of excitation, which gives a single electron enough energy to overcome the vacuum barrier, i.e. lifts its energy above the vacuum level, can cause the emission of electrons. Such processes involve the

- bombardment of the surface with
  - *(i)* electrons,
  - *(ii)* photons, or
  - *(iii)* heavy charged particles,
- thermal emission due to heating of a sample, or
- field emission in high electric fields.

Depending on the involved processes, the emitted electrons might carry valuable information about the specimen, from which they have been emitted, and can therefore be used for target analysis.

In this work, the focus lies on electron emission induced by the impact of ions. Obviously, due to the much larger number of degrees of freedom, the involved processes are more complicated than e.g. in the case of the emission of a photo-electron or an electron induced secondary electron.

Ion induced electron emission in general can have two fundamentally different excitation mechanisms:

(i) kinetic energy transfer from the projectile into the electronic system of the solid, where the projectile velocity plays a key role [16], causing so-called *kinetic electron emission* (KE), or

(ii) direct or indirect excitation due to electronic interaction with the empty states of the ion, thus, purely driven by the potential energy stored in the ion, resulting in *potential electron emission* (PE) [15].

Usually, these two contributions to the total electron emission from a solid, kinetic and potential emission, respectively, can be separated completely, because of little interdependence. In some cases, however, correlations can be found [27].

Kinetic emission is, except in the very low energy region, the dominating process for singly charged ions. For beams of atoms in the ground state, impinging on a surface, no potential energy is involved, thus purely kinetic electron emission can be observed. It is mainly determined by the energy loss of the projectile in the solid [28]. In contrast, potential electron emission does not need any projectile movement. It is purely driven by processes, involving the ion's empty states.

Kinetic electron emission

Parts of the following description are taken from[19].

Excitation of electrons in the sample due to the kinetic energy of the impinging projectile can happen due to direct collisions of the projectiles with an electron. In the low velocity regime ($v < v_0$), the electronic stopping power (or electronic stopping force) is expected to be nearly proportional to the projectile's velocity [29].

In order to be ejected, the excited electrons have to reach the surface (electron transport) and eventually penetrate the surface into the vacuum. Since kinetic electron emission occurs due to energy transfer of the projectile to the electrons of the solid, it is in principle a sub-surface effect, where the projectile has to penetrate the bulk. In contrast, as discussed later, potential emission occurs often mainly in front of the surface. Therefore, usually the energy- and angular distributions differ substantially.

Kinetic excitation of electrons occurs inside the solid due to [16]

(i) direct collisions between projectiles and target electrons and/or target nuclei and
(ii) various secondary processes.

Here, (i) refers to the excitation of conduction (or valence) electrons into free states above the Fermi level, ionisation of the target atoms' inner shells, ionisation of the projectiles and electron loss from the projectile, respectively. Additionally, (ii) concerns cascade multiplication of diffusing electrons, excitation due to recoil atoms and backscattered projectiles, and eventually plasmon and photon emission processes [19].

Due to the complexity of the involved processes, several theoretical approaches do not directly consider the detailed mechanisms, but rather treat the electron production in a semi-empirical way (see e.g. review in [16] for a more detailed treatment).

It has been suggested to assume proportionality of the electron yield to the mean electronic energy loss per length element dE/dx of the primary particles, the stopping power $S_e = -\left(\frac{dE}{dx}\right)_e$ [28]. All possible excitation mechanisms are summarised in the quantity S_e. Of course, the proportionality in reality deviates from the ideal case, thus, the proportionality constant is in fact not a constant, but depends on the projectile's velocity and/or internal excitation, etc.

The principle electronic excitation mechanism at high impact energies of electrons, ions and atoms is thought to be the direct collisional momentum and energy transfer to conduction electrons from the Fermi edge and the ionisation of inner-shell electrons (see e.g. [16]).

In such direct collisions, the maximum energy transfer T occurs, when the projectile with velocity v_p hits an electron traveling at Fermi velocity "head on", thus

$$T = 2m_e v_p \, (v_p + v_F) \tag{2}$$

with the electron mass m_e and the Fermi velocity v_F [28]. It should be noted, that early investigations [30] discussed the problem of a too low energy transfer onto an electron at rest, to overcome the vacuum barrier. When considering the initial velocity the electrons already have at the Fermi edge, emission becomes possible [28, 31]. However, below a certain projectile threshold velocity v_{th}, the energy transfer does not exceed the sample's work-function W_Φ and the electron cannot escape into the vacuum. This threshold can easily be determined to [28]

$$v_{th} = -\frac{v_F}{2} + \left(\frac{{v_F}^2}{4} + \frac{W_\Phi}{2m_e}\right)^{\frac{1}{2}} \tag{3}$$

where again the Fermi velocity v_F and electron mass m_e occur. In fact, below this velocity, no kinetic emission should occur.

Since the electron of concern is a conduction electron, a better estimation is obtained, when considering not the free-electron's mass, but an effective mass due to the binding in the conduction band $m_e^\star$ [17], which depends on the band structure of the material (see e.g. [32, 33]).

An alternative theory for kinetic emission [34] is also predicting a velocity threshold of similar magnitude, however, it assumes only direct creation of an inner-shell vacancy by the primary ion, followed by an Auger process, which eventually excites an electron from the conduction band. It provides also a threshold velocity, as the inelastic stopping power equals the binding energy of the core electron with respect to the Fermi level, i.e. as the valence electrons cannot be excited.

The threshold velocity from eq. (3) works rather well for proton impact onto metallic surfaces, but fails by far for heavier particles, for which KE is already observed at impact velocities well below the predicted value [17]. In such a case, quasi-molecular effects have to be considered, since the simple assumption of a head-on collision becomes more and more inappropriate, the closer the velocity gets to the threshold. Due to the large mass difference between the electron on the one hand, and the light ion on the other hand, the very ineffective kinetic transfer mechanism improves in the case of heavier projectile atoms or ions as a

consequence of so-called Pauli-excitation [35], known from inelastic atom collisions in the gas phase, which then increases the maximum energy transfer, and through that, decreases the threshold velocity. A more detailed model considers quasi-molecular auto-ionisation processes in close encounters of the projectiles with positively ionised target ion cores, which has been investigated e.g. for the case of singly charged noble gas projectiles [17].

In general, electrons emitted due to kinetic processes upon ion impact, show rather low kinetic energies of typically just up to a few eV.

In this work, we also provide experimental results for below-threshold emission.

Potential electron emission

Parts of the following description are taken from [19].

The ion carries potential energy, which directly influences the solid, thus, even without touching the surface, electrons can be ejected into the vacuum. The underlying energies completely originate from the internal energy of the ion, hence, a neutral atom beam does not show PE at all (as long as the atoms are not in an excited state).

The potential energy of an ion of charge-state q is determined by

$$W_{pot,q} = \sum_{j}^{q-1} E_i^{(j)} \tag{4}$$

with the ionisation energy of charge-state j being $E_i^{(j)}$, and the final ion's charge-state q. Of course, the potential energy is a function strongly increasing with the ion's charge-state.

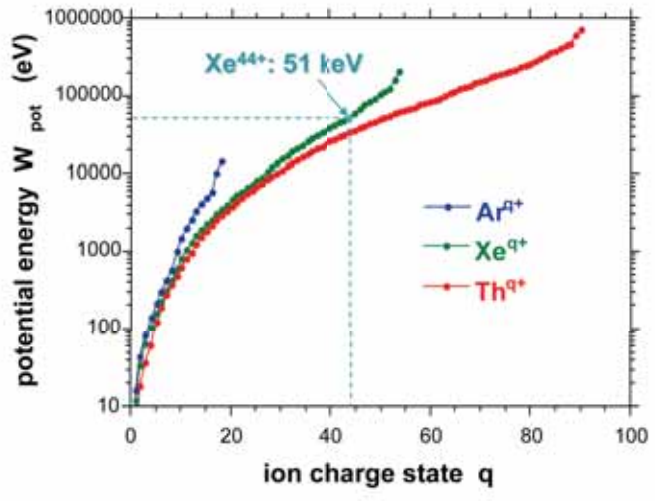

Figure I-1:Potential energy as a function of the projectile's charge-state
Potential energy according to eq. (4) for different projectiles (Ar^{q+}, Xe^{q+}, Th^{q+}). Figure taken from [36].

Especially when considering highly-charged-ions (HCI), the involved potential energies can become pretty large and for slow projectiles exceed the kinetic energy by orders of magnitude. As an example the potential energy of a Xe^{44+}

ion , 51 keV, is shown in figure I-1. Nowadays, these high charge-states can be provided for experiments by electron beam ion traps (EBIT) [37].

Potential emission due to the impact of singly, doubly, or multiply charged ions has already been investigated decades ago (e.g. [38]). It turned out, that the emission happens due to rapid electronic transitions from the surface into empty states of the incident particle.

Different processes have been identified as being involved into the phenomenon of potential electron emission (see e.g. [15]):

(i) *Resonant neutralisation* (RN) involves electron transfer from the surface conduction band into unoccupied states of the projectile ion. The transition can only happen, if the initially unoccupied final state is energetically degenerate with the electrons in the conduction band. The process itself does not directly cause an electron to be emitted, but acts as a precursor for subsequent transitions. This is the most important process concerning the formation of "hollow atoms" [39] in front of a surface (see later in this chapter).

(ii) *Resonant ionisation* (RI) being the inverse process to the RN. Upon this process, an electron is transferred from the projectile into an empty surface state. Also this process does not directly lead to the emission of an electron.

(iii) *Auger neutralisation* (AN) is a process, where one electron of the target directly fills the vacant ground state of the projectile ion. The related energy is transferred to another valence electron, lifting it above the vacuum level. The process can occur, if the ionisation energy of the filled state, $W_i^\star$, exceeds twice the work function W_Φ. The kinetic energy of the emitted electron E_e obeys $E_e \leq W_i^\star - 2W_\Phi$. $W_i^\star$ is the effective ionisation energy, which, due to a level shift according to the interaction with the image charge, depends on the distance between the surface and the projectile.

(iv) *Auger de-excitation* (AD) of the projectile occurs after RN- or AN-transitions, when the remaining excitation energy exceeds the work-function W_Φ. The excited projectile electron can now become emitted when an electron from the surface is captured into the ground state, or, on the other hand, can undergo a transition into the projectile's ground state itself, causing the emission of another surface electron.

(v) *Autoionisation* (AI) occurs for doubly or multiply excited projectiles. One or more electrons are emitted into vacuum while other electrons in excited states become de-excited. In combination with preceding RN into highly excited states, this is an important process for electron emission of MCI.

(vi) *Quasi-resonant neutralisation* (QRN) can occur only when the projectile comes very close to the surface, because a large overlap of the inner electronic orbitals is needed. It is an important process in the interaction between the surface and a MCI especially within the bulk.

(vii) *Radiative de-excitation* (RD) of a neutralized, excited projectile is much less probable than Auger-type de-excititation mechanisms, due to the much larger timescales of occurrence. Especially for high-Z projectiles, however, x-ray emission can be a significant contribution when filling the inner shells in the last steps of the MCI decay.

The above mentioned formation of hollow atoms in front of a surface when speaking about the interaction of a MCI or HCI is going to be discussed in section I.3.1.

For detailed reviews about the whole topic of ion induced electron emission, refer to e.g. [15], [16] and references therein.

I.2.3 Current Method

I.2.3.1 Experiment

This chapter has been published earlier to wide extent [7].

Ion induced electron emission yield measurements were performed at the ECR ion source at TU Wien described in detail elsewhere [40, 41]. The source is capable of producing singly and multiply charged ions (charge-state q) of various species with acceleration voltages between 0.5 kV and 10 kV and intensities between a few pA up to some µA, depending on the species.

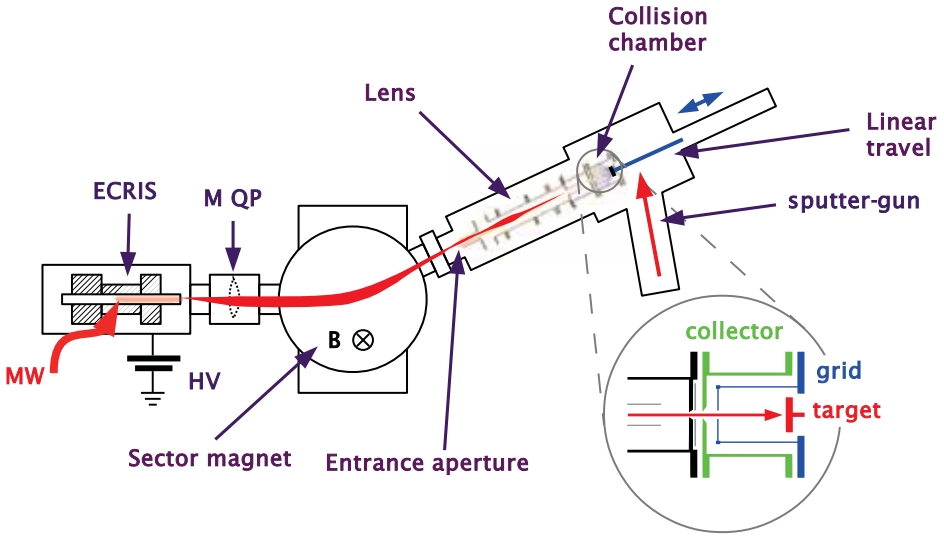

Figure I-2: Beamline Overview
The microwave (MW) heated plasma inside the TU-Wien ECRIS [40, 41] provides high charge-state ions from gaseous atoms and molecules, accelerated by a high voltage (HV) of 500 V up to 10 kV. The beam is focused via magnetic quadrupole lenses (M QP) and mass-charge-separated by a magnetic sector field at an entrance aperture. Eventually the beam can be focused and decelerated by an electrostatic deceleration lens system into the collision chamber, which is shown in more detail. It consists of the target (red), surrounded by a cylindrical symmetric grid (blue) as well as a separate collector electrode (green). The target holder can be linearly moved into a position in front of a sputter-gun along the chamber axis.

The extracted ion beam (D^+, He^{q+}, C^{q+}) is focused by two magnetic quadrupole lenses with perpendicular focussing planes, mass-separated by a magnetic sector field at an entrance aperture at the beamline of 3 mm diameter. The ion beam

can be accelerated or decelerated and focussed onto the target surface with a custom accel- / deceleration lens system, consisting of several elements. In front of the lens system, directly behind the entrance aperture, a set of electrostatic steerers is located. A second set of deflection plates is placed inside the last deceleration lens element and allows the experimenter to centre the ion beam onto the sample, especially when decelerating. When entering the main chamber, the beam passes a final aperture of 3 mm diameter, behind which an electron repeller electrode is located. This is kept at about -100 V with respect to the aperture potential and ensures, that no electrons from the beamline can enter the collision chamber and cause faulty measurements. The apparatus is mounted inside a bakeable UHV chamber, differentially pumped via a Turbo Molecular and occasionally by a Ti sublimation pump, resulting in a base pressure in the 10^{-10} mbar regime. The vacuum vessel between the ion source and the experiment's chamber always had a pressure better than 10^{-7} mbar. The main chamber is equipped with an argon sputter-gun under 10° grazing incidence to the target surface, which is used for cleaning the surface. For this purpose the target can be moved along the beam axis into a proper position with a linear translator.

The total electron emission yield was determined by a current method with a retarding grid [16, 42]. The basic principle of this method in its simplest form is to first measure the electrical current at the target when applying a retardation voltage to a surrounding grid, in order to keep all emitted electrons at the sample. The measured current then gives the contribution of impinging ions only. In the next step a positive voltage is applied to the surrounding grid, so that the electrons are extracted and leave the target, contributing to the measured target current in an additive manner. Denoting the current at the target I_T and indicating the applied voltage to the surrounding grid by the superscript "+" for positive extraction voltage and "-" for a negative retarding voltage, in order to suppress the electron contribution, the electron emission yield follows as $\tilde{\gamma}_1 = q\frac{I_T^+ - I_T^-}{I_T^-}$. The projectiles' charge-state is q.

A detailed description of the electronic equipment as well as of the data acquisition system can be found in [19]. The collision chamber has been developed further since then and is intensively presented and discussed in [43].

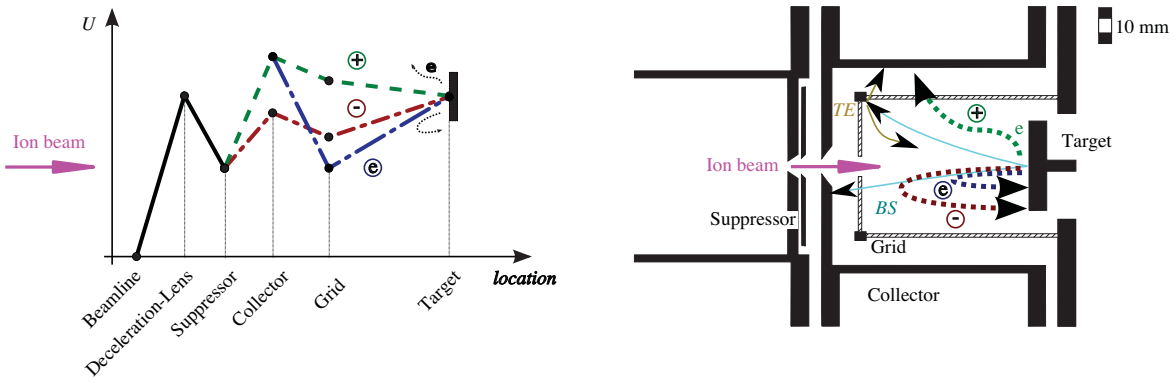

Figure I-3: Current Method for Electron Emission measurements

Schematic illustration of the voltage switching states "+", "-", and "e"(left). The lines in the chart indicate the electrostatic potential the ions find when crossing the collection chamber towards the target. The electrodes shown in the right figure are cylindrically shaped around the beam axis. The switching states' influence onto the electrons, as well as the back-scattered projectiles (BS) and tertiary electrons (TE) from the grid are indicated. The coloured, dotted lines indicate the electron trajectories (just schematically) and are depicted with the corresponding state (see text for details).

The actual geometry of the used apparatus is shown schematically in figure I-3. One can see, that in addition to the mentioned grid, a surrounding collector electrode is introduced. The grid, as well as the collector are rotation-symmetric, around the beam axis. The grid consists of a holder structure of several massive rods, which are wrapped by a thin wire. The grid's geometric transparency is around 90% when averaging over all directions. A more detailed description of the geometry can be found in [43].

This electrode is biased positively with respect to the grid and also measured with a pico-amperemeter, as the target and the grid as well. The potentials of sample, grid and collector are each digitally controlled and the electrical currents of grid and collector are measured simultaneously via separate standard electrometers, converted into digital signals and recorded by a computer.

The bias voltage forces secondary electrons produced at the collector electrode not to reach another part than the collector itself, thus not contributing to any measured current. The collector currents I_C^s with the switching-state $s \in \{+, -, e\}$, allow a second determination of the emission yield, since the extracted electrons in the "+" state, which pass the grid are measured at the collector electrode. When denoting the grid's effective transparency c, one can obtain another value for the electron emission yield by

$$\tilde{\gamma}_2 = -\frac{q}{c}\frac{I_C^+}{I_T}, \tag{5}$$

in addition to $\tilde{\gamma}_1$. The grid's transparency c is not directly determined by just the geometry, but highly influenced by the applied voltages, because the electric field enhances the transmission. Also electrons, that hit the grid, might lead to the emission of a significant number of secondary electrons [44], which contribute to the effective transparency. Therefore, it can only be determined in calibration measurements by demanding $\tilde{\gamma}_1 = \tilde{\gamma}_2$. This has been done in a large number of measurements on a gold sample, from which eventually a value of $c = 0.91 \pm 0.02$ has been derived.

Obviously, the statistical error at small yield values becomes large in the case of $\tilde{\gamma}_1$, because it is basically a subtraction of two large numbers, as compared to the yield itself. Thus, $\tilde{\gamma}_2$ is better suited to determine the actual value for the yield at lower values. This is why all the numbers shown in this work, unless stated differently, refer to the yield measured via the collector, i.e. $\tilde{\gamma}_2$, or more precisely a slightly modified expression, denoted as γ_2, as discussed later on in this section.

In order to extract the emitted electrons (switch state "+"), a voltage of +20 V is applied to the grid with respect to the sample. Complete suppression of the corresponding electron current is achieved by biasing the grid to -60 V (switch state "-"). Of course this holds only, as long as the emitted electrons are slow enough, i.e. have a kinetic energy below 6o eV. For typical kinetic electron emission within the covered energy range this should be fulfilled for the vast majority of emitted electrons.

The collector electrode is always kept 30 V more positive than the grid in order to suppress secondary electron emission. Another repelling voltage state "e" was used in combination with "-" in order to obtain some indication about error contributions, which will be discussed in the next paragraphs. This state uses a larger electric field between the collector at 50 V and the grid, which is 100 V negatively biased with respect to the target. The voltages given here were used for metallic targets. For the insulators, the extraction voltage was increased, in order to minimise possible effects from a charged surface.

The voltages presented here are always relative values, with respect to the target. As already mentioned, a high positive potential can be applied to the sample, in order to decelerate the projectiles. Therefore, all the electronic equipment is located inside a HV cage, out of which the digital signals are transported via fibre optics.

Backscattered (BS) projectiles contribute either directly to the measured currents, as long as they stay ionized during the scattering process, or indirectly via electrons they eject from the grid. For a theoretical description of the arising contributions to the measured currents and their correction, we use very simple average values, where the energy and angular distribution, respectively, are not explicitly taken into account. This simplification should be valid, as long as one keeps in mind, that some constants, as e.g. the grid's transparency c, may in fact change their value slightly as a function of impact energy and projectile species.

When denoting the reflection coefficient for ions having a final charge-state $m \leq q$ after the scattering event R_m, the electrical current of the BS ions follows to $I_{BS} = \sum_{m=1}^{q} I_{BS}^{m} = \frac{1}{q}\sum_{m=1}^{q} mR_m I_0$ producing an additional current at the grid of $I_{G,BS} = (1 - c^{\star})I_{BS}$ with the grid's geometrical transparency $c^{\star}$ (in contrast to the effective transmission for electrons $c > c^{\star}$, because of the lower mass, thus different inertia, of the electrons). The incident ion electrical current onto the target is I_0. The backscattered ions directly influence the measured currents independently of the applied fields, as long as the projectiles' kinetic energy is large compared to these. As soon as one reaches energies below several 100 eV, one can think about contributions of directly scattered projectiles, which are in fact influenced by the applied voltages. This can be seen as one of the limitations of the apparatus at low kinetic energies.

Especially when decelerating the ions, there is a risk of hitting any other electrode than the target directly. This, of course, is a severe problem, since emitted electrons influence the measurement and eventually lead to wrong results. Such direct hits onto the electrodes (Collector, Grid) can be identified due

to the fact, that one expects a significant discrepancy between the "-" state and the "e" state, respectively. At the very low projectile velocities one expects also switch-state dependent focusing and deflection of the ion beam, causing different locations of impingement, where the surface conditions might differ. The induced change of the yield can be minimised only by proper surface preparation in advance, but still it definitely plays a significant role in the lower impact velocity regime. A purely electrical error component, a blind-signal without any physical current in the apparatus, which is dependent on the switch state is eliminated by subtraction of a measurement without any ion beam on the target. This contribution is very small and only plays a role for very small incident currents I_0 < 1 nA.

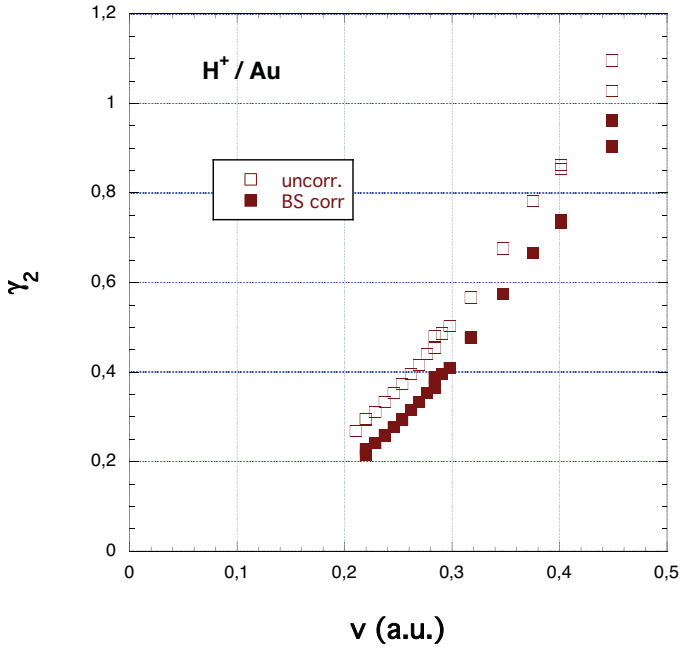

Figure I-4: Backscattering correction
The electron emission yield from a gold substrate under the bombardment with a proton beam is shown as a function of projectile velocity in atomic units. The empty squares represent the result according to eq. (5), i.e. without any correction for backscattered projectiles. The filled squares, on the other hand, show the same results, but with the backscattered ions taken into account. One can see, that the correction can reach a magnitude of up to about 10%.

Concerning direct error contributions, backscattered projectiles cause the emission of electrons from the grid. We refer to these electrons as tertiary electrons (TE) although this term might be a bit misleading. The average TE emission yield of the grid for projectiles of charge-state m is referred to as η_m. Of course this number inherently includes not only the emission yield, but also the backscattered's charge-state as well as its kinetic energy. The current of emitted electrons from the grid is $I_{TE} = (1 - c^*)\frac{1}{q}\sum_m \eta_m R_m I_0$, which is positive due to the leaving of negatively charged particles. Depending on the state s, the amount of TE reaching the collector, α_s, changes. The fraction $1 - \alpha_s$ of TE contributes directly to the target

current. It is obvious that $\alpha_+ \approx 1$, i.e. practically all electrons will reach the collector electrode, whereas both, α_- and α_e are not so well defined. Trajectory simulations with SIMION [45] were performed, in order to verify the experimental hints found, which indicate α_e being roughly 1, meaning that the majority of the electrons produced at the grid's cylinder eventually hits the collector or the grid itself, because of feeling the stronger electrical field towards the collector electrode through the wire spacing of the grid. The contribution to the target current is therefore negligible.

In order to find a rather compact formulation we introduce the fraction β_s of electrons emitted from the target, which can actually leave the sample due to the applied fields, thus $\beta_s = 0$ for $s \in \{-, e\}$ and $\beta_+ = 1$. The current of emitted electrons from the target due to ion induced electron emission is $I_{EE} = {}^{\gamma I_0}/_{q}$. Summarising these contributions, the measured currents can be written as

$$\begin{aligned} I_T^s &= I_0 - I_{BS} - (1-\alpha_s) I_{TE} + \beta_s I_{EE} \\ I_G^s &= (1-c^\star) I_{BS} + I_{TE} - \beta_s (1-c) I_{EE} \\ I_C^s &= c^\star I_{BS} - \alpha_s \mathrm{I}_{TE} - \beta_s c I_{EE} \end{aligned} \tag{6}$$

from which the impinging ion current $I_0 = I_T^s + I_G^s + I_C^s$ follows immediately by summing all three equations in (6). In principle, as can be seen, the current does theoretically not depend on the switch state $s \in \{+, -, e\}$, as long as the ions' kinetic energy is high enough for the beam to overcome the potential barrier in front of the target without hitting any other electrode.

Solutions of (6) lead to possible evaluations for the electron emission yield:

$$\begin{aligned} \gamma_1 &= \frac{I_T^+ - I_T^e}{I_0} \\ \gamma_2 &= -\frac{q}{c}\frac{I_C^+ - I_C^e}{I_0} \\ \gamma_3 &= -\frac{1-q}{c}\frac{I_G^+ - I_G^e}{I_0} \end{aligned} \tag{7}$$

which have distinct advantages and disadvantages concerning their practical use. For small total electron emission yields γ_1 suffers from a large statistical spread, since it results from a difference of (similar) large numbers. γ_3 is the only solution of (7), independent of α_s, allowing to check for validity of the assumption $\alpha_e \approx 1$, but, however, small errors lead to large discrepancies, because they are scaled up a factor $\frac{1}{1-c^\star} \approx 10$. The situation is much better in the case of γ_2, since I_C^e is a small quantity compared to $I_C^+$and c close to 1. Therefore γ_2 from (7) was used for the evaluation of the presented data after careful calibration measurements at large electron emission yields and small backscattering coefficient (electron emission from gold by keV Ar^{q+} ions) assured agreement between the three different methods in (7).

The lower energy limitation of the apparatus, around $100\ q$ eV, arises mainly from the already mentioned variation of the spot size on the sample surface, due to a lens effect depending on the applied voltages. Especially the positive voltages, applied to the collector and the grid cause significant widening of the ion beam in the lower 100 eV regime. For the appearing larger distances between the impact event and the central axis, the surface condition might be slightly different, as already mentioned earlier in this work. Additionally, the grid's transparency depends on the location of the electron emission, thus the ion's impact lateral

position on the sample, and cannot be treated as being state-independent any more when reaching low impact velocities. This is a fundamental limitation of the method.

Without explicitly mentioning, all currents in the above treatment are actually time averaged values. The averaging duration was around 1 s, after which the switch state was changed to the next one. The first 2 s after setting a voltage were not recorded, in order to avoid electrical artefacts, thus after around 9 s, when all three states s have passed, a new measurement cycle was started. Each such cycle represents one time-dependent yield value. The above treatment assumes, that the fluctuations of the incident current I_0 on this time-scale are negligible.

Usually, the measured values for the electron emission yield vary with time, due to surface modifications (sputtering) and implantation. The measured values represent just equilibrium values between implantation on the one hand and sputtering on the other. More details on the CM method used can be found in [43].

The usual metallic samples (tungsten, gold, Silver) were sputter cleaned with 2keV Ar^+ projectiles under an angle of incidence of about 10° before a measurement was performed.

In addition to the investigation of electron emission from metallic samples, the method was extended to be able to measure electron emission yields from insulators. This is especially difficult, because the remaining charges at the sample surface attract the electrons, and trap them. Therefore, usually one can only measure electron emission from insulating materials by probe beams of very low intensities, where the charge of individual projectile impacts does not influence the other emission events because of temporal and/or local displacement. One possibility for measuring under such conditions is the usage of an electron statistics detector (see e.g. [46] or chapter I.2.4.2 in this work). With such a method, single events are counted, thus, the mean time between two impacts at the 'same location', i.e. a location, where the electric field of a remaining charge is significant, is large, as compared to the time necessary to remove the charge. This is, of course, determined by the conductivity.

Since the emitted electrons also contribute to the remaining charge, especially HCI cause significant sample charging and in consequence a negatively influenced electron emission yield measurement. For particles like e.g. Xe^{40+}, the electron emission yield from a gold surface due to potential emission can easily reach values of more than 120 electrons per impact event [46]. Therefore, it might be necessary to heat the sample, in order to achieve the necessary electrical conductivity [46].

In this work, we used lower charge-states, and therefore, the electron emission yield is much lower. On the other hand, the current method needs a minimum ion current of approximately 1 nA, to give reliable results, which is orders of magnitude above the typical single ion impact regime in the case of the electron statistics measurement. The basic idea, which should intentionally be tested, was to heat the sample to several hundreds of degrees, so that the electrical conductivity reaches values high enough to allow charge removal on the necessary time-scale.

Due to the fact, that the involved currents are very small and at the same time the insulators at the elevated temperatures become more and more conductive, one runs into the problem, that an electrical target heating by heat conduction gives a significant background current measured at the target. In order to avoid this current, which with increasing target temperatures can even exceed the ion current by far, one has to avoid direct contact of the heaters with the sample.

Therefore, a sample holder was constructed, which uses an indirect radiative heating, which allows sample temperatures of up to about 380°C without significant error currents at the target.

One limitation was, that the whole holder needed to fit into the experimental chamber, which had been used with conductive targets before.

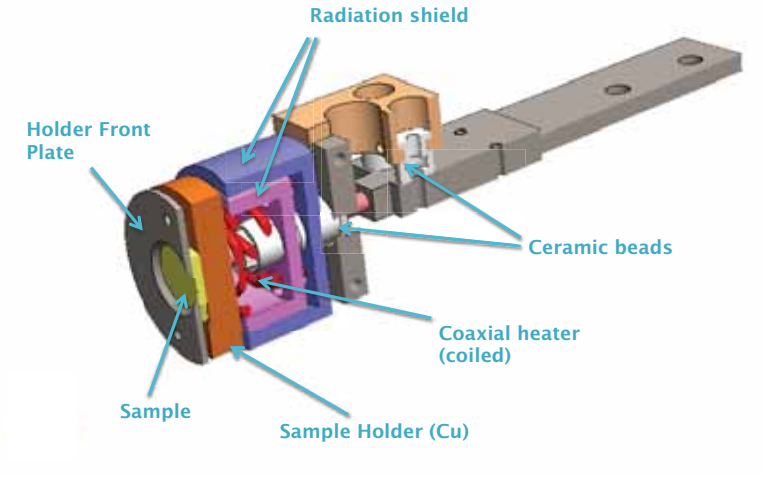

Figure I-5: Cut through the indirectly heated sample holder
From left to right: The ion beam impinges from the left onto the sample (yellow), which is sandwiched in between a holder front plate (gray) and a massive copper plate (orange). This plate is mechanically mounted via a thin rod (light red) on a cooler stainless steel holder (right, gray). The heating is achieved via radiation from a coiled coaxial heater (red). Losses are minimized by a set of two concentric radiation shields (purple, violet). Electrical isolation is achieved by usage of ceramic beads (Al_2O_3).

The basic idea is, that those insulating parts, which separate the electrically measured target from the heaters, must not become as hot as the target. The used insulators are made of Alumina (Al_2O_3), which has an electrical resistivity of more than 10^{12} Ω m at room temperature.

The sample itself (in this work a LiF(100) single crystal), is mounted on a massive copper plate, held by a stainless steel sheet with a central hole of 9 mm diameter (figure I-5). The copper plate is used to ensure a uniform temperature distribution, due to its high thermal conductivity of about 400 W/(K m) [47]. The backside of this Copper disk is covered by graphite paint, which causes the emissivity to become practically 1. The sample's temperature is monitored via a K-Type thermocouple, connected to the copper disc, which is holding the sample. Mechanically, the copper disk is mounted on a central 3 mm diameter rod, which itself is fixated on a stainless steel holder, a few centimetres away. Over this connection, the electrical ion current is measured. On this steel holder, which never reaches temperatures as high as at the sample, alumina parts are used to hold another part, where the actual heater is anchored. This is built by a stainless steel coaxial heater, which is coiled to achieve the necessary heating power within the given volume, defined by the surrounding radiation shields. The total length of the heater is approximately 10 cm, allowing a total heating power of about 25 W. The radiation shield consists in principle of two concentric stainless steel cups, with polished surfaces, both mounted via ceramic parts (Al_2O_3) on the central rod.

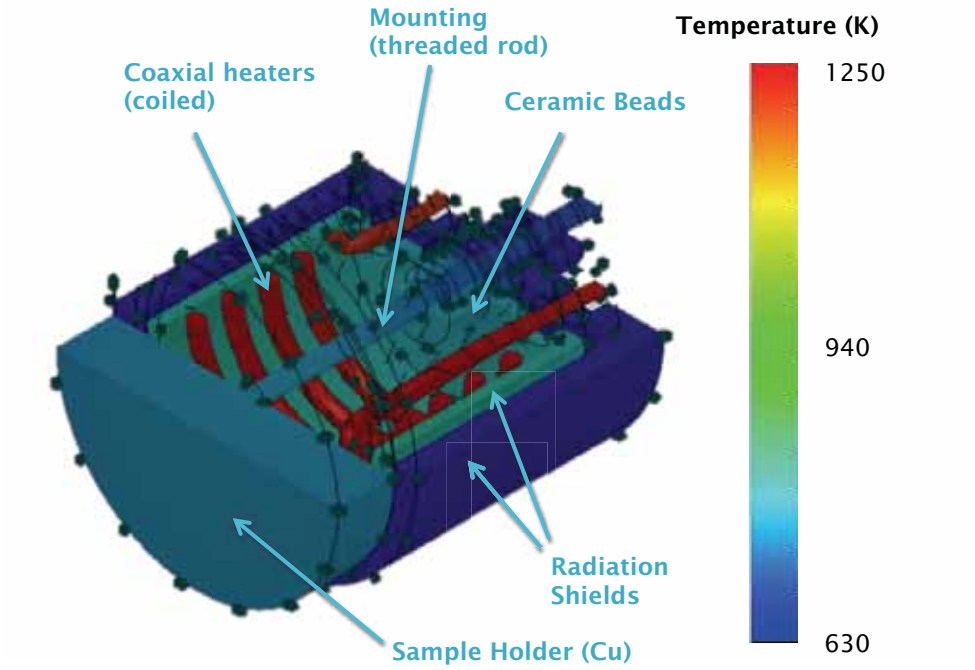

Figure I-6: Simulated temperature distribution

A cut through the essential parts of the sample heater is shown. The calculated temperature is colour-coded. It is a result of simulation with the (heat) transport code SolidWorks [48]. The image gives an idea about the working principle of the heater coil in combination with the radiation shields surrounding it.

The temperature distribution has been simulated (figure I-6), in order to estimate the maximum temperature, which can be achieved. Basis of the simulation is the maximum heating power of about 2.5 W/cm, equally distributed along the coaxial heater. The emissivity values for all surfaces were roughly estimated to 0.2 for clean metallic surfaces, up to 0.6 for the graphite layer at the backside of the copper disk. The surface temperature of the coaxial heater reaches values as high as roughly 1000°C, which is above the manufacturers recommendation.

One can see, that the outer shield reaches temperatures well below the one of the copper disk, also preventing overheating of other parts outside, especially insulting ceramic parts, which, as mentioned above, could possibly give rise to blind currents when becoming too hot. Heat conduction through the central rod leads to the heating of these outside holder parts (not shown in the simulation figure), where the crucial insulators are located.

Empirically, it turned out, that above a target temperature of about 390°C, the target leak current reaches values of several nA. Therefore, the target temperature was chosen below this value for measurements. It should be mentioned, that this currents occur without decelerating the beam by applying a high voltage to the target itself. When doing so, massive leak currents occur even at lower temperatures. Therefore, beam deceleration is not an option when measuring insulating samples at high temperatures.

The temperatures of the involved parts were at first also estimated by an analytical model, including radiative as well as conductive transport, which is described in detail elsewhere [49]. In fair agreement with the model simulations, we reach temperatures of more than 420°C at the sample holder, using about 25 W of total heating power. The electron emission yield measurements from LiF were finally conducted at temperatures of about 370°C (see chapter I.2.3.4).

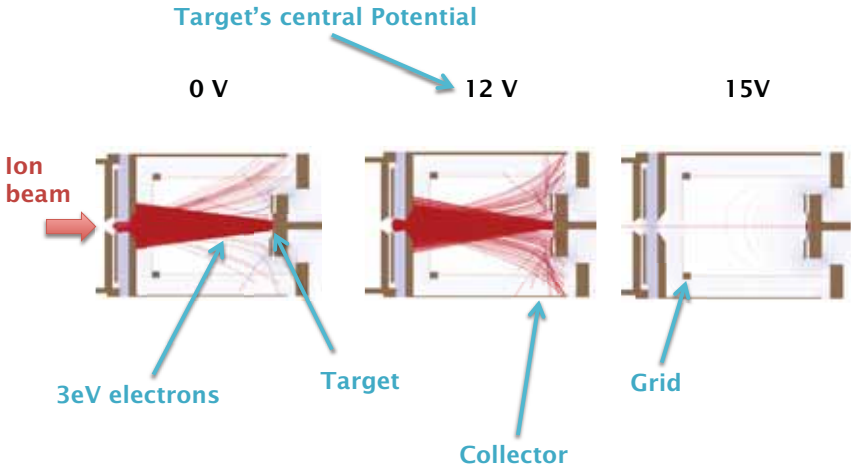

Figure I-7: Electron trajectory simulation examples
The graphic shows some examples of electron trajectory (red) simulations, performed with SIMION [45]. A cut through the collision chamber is shown (brown). The target charging causes an effective potential, from which the emitted electrons are starting. In the beneficial case of no charging (left), the emitted electrons are extracted by the applied field, according to the "+" switch state. In contrast, when reaching an effective central potential of 15 V, no electrons can be extracted at all. The ion beam enters from the left through an entrance aperture, equipped with an electron repeller. Afterwards, the beam passes the collector electrode, the grid, and eventually hits the target in the centre.

In order to get an idea of the effect, a charged sample has onto the emitted electrons, a number of simulations with SIMION [45] were performed. These investigations can be found in a more detailed description in [49]. Essentially, the target was modelled by a set of 4 equidistant concentric rings surrounding a central disk. The potential at the outer ring was fixed to ground, whereas the centre was varied between 0 V and 20 V. The rings' potentials were chosen according to a linear interpolation between the central and the outer potential. The energy of the emitted electrons was chosen between 0.5 eV and 3 eV. Faster electrons, would suffer less from the surface charging, than slower ones, therefore no higher electron energies were included in the investigation. According to the switch-stare "+", i.e. extraction of emitted electrons away from the target onto the collector electrode, the grid potential was set to 70 V with respect to the grounded sample, the collector voltage was 95 V. For this simulation we chose a uniform angular distribution for the emission.

It soon turned out, that a charging of even a few volts was enough to prevent electrons from being emitted properly, thus the measured effective yield drops.

After emission from the target centre disk, according to a uniform distribution of lateral positions in a circular region of 2 mm in diameter, the trajectories are recorded and the location of impact is determined. Only those particles, which

reach the collector electrode are counted and compared with the total number of emitted particles. From this, a quantity referred to as collection-efficiency is calculated.

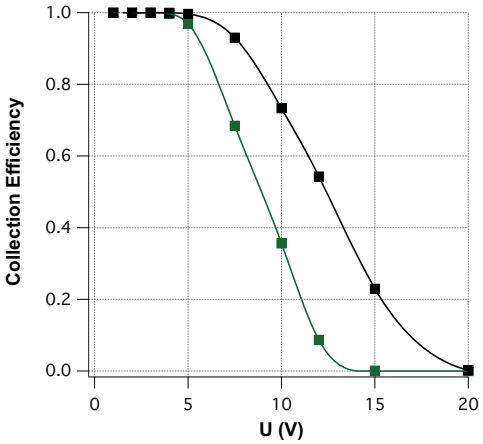

Figure I-8: Simulated electron collection efficiency
The values are a result of a SIMION [45] simulation, counting the number of electrons actually captured at the collector electrode after being emitted from the target centre region.

The simulated collection efficiency, as can be seen in figure I-8, stays rather constant for effective target potentials of up to a few volts, before it suddenly starts to drop rapidly with increasing charging. The lower the initial kinetic energy of the electrons is, the stronger is this effect, the sooner the drop sets in. Since the grid's transparency here practically equals 1 – only the mounting parts could block the particles on their way, since the wire is not explicitly included in the simulation, but just a fully transparent equipotential surface is used for simulating the grid – the collection efficiency automatically reaches a value of 1 without any surface charging.

Concerning the surface charging, as discussed earlier, the balance of incident particles and charge removal due to conduction is essential. When considering a very simple rate equation for the time evolution of the accumulated surface charge density q at the surface as a function of the incident flux j_{in} and the discharge flux j_d, characterised by the effective discharge time τ_d,

$$\dot{q} = j_{in} - j_d = j_{in} - \frac{q}{\tau_d} \tag{8}$$

and solving it for the equilibrium case $\dot{q} = 0$, we obtain direct proportionality of the equilibrium charge density at the surface and the incident current flux j_{in}. Therefore, also the surface potential is directly proportional to the incident flux. When increasing the temperature, charge transport through the bulk as well as along the surface is enhanced and hence the effective characteristic discharge time is reduced.

In order to understand the charging especially to define a proper parameter space, in which the presented method allows reliable measurements of the emission yield, a systematic study of the measured yield for various incident currents was performed.

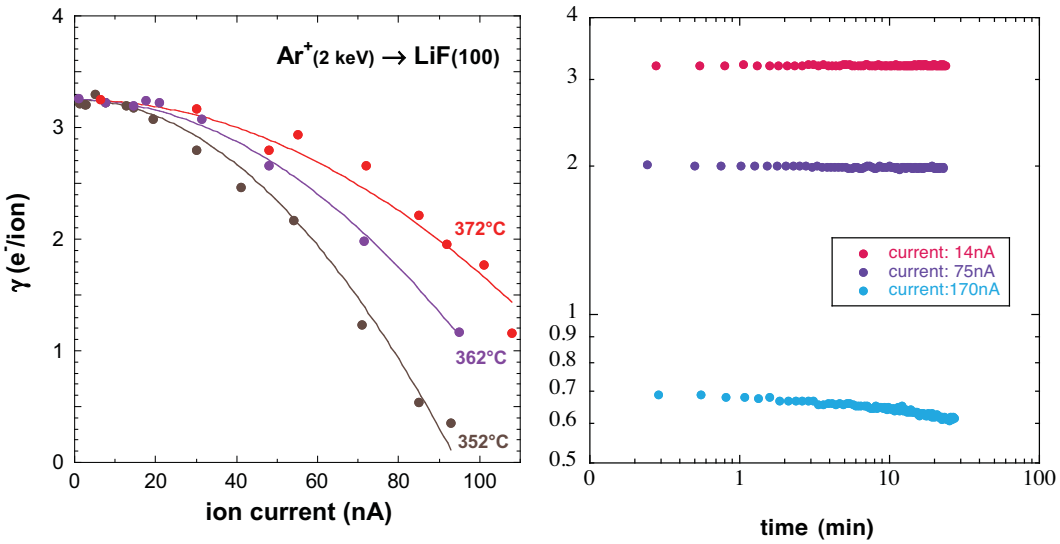

Figure I-9: Incident current dependence of the measured yield

The measured electron emission yield is plotted as a function of incident ion current (left) for three different target temperatures. The dots represent equilibrium (time-independent) values. The lines are polynomial fits to guide the eye. As shown, especially at large ion current, or low temperature, respectively, this equilibrium is reached on a time-scale of minutes or even hours (right). In this (right) panel, the temperature is fixed to T=362°C.

The target's temperature was varied, starting at values as high as possible at leak currents well below 1 nA. When measuring the electron emission yield, one finds distinct time-dependent behaviour, as soon as the ion current is increased. This can be understood in accordance with equation (8), because of the time-evolution of the charge-density at the surface, which has to eventually reach some equilibrium. The time dependence, especially at high beam intensities, or low temperatures, respectively, reveals involved time-constants of minutes or even hours (figure I-9, right). The equilibrium values reached after some time are plotted as a function of incident current (figure I-9, left) and reveal a distinct behaviour. The curves show similar behaviour as the collection efficiency (figure I-8), because, according to eq. (8), the equilibrium charge density, thus the resulting electrostatic potential, is proportional to the incident ion current. One can see, that below about 15 nA, practically no change in the measured yield occurs, even for target temperatures as low as 350°C, whereas larger intensities cause a drop of the measured electron yield.

The sample's temperature was chosen in a way that for the occurring ion beam currents the sample's surface charging was negligible due to the enhanced ionic conductance of the LiF(100) crystal. To check whether the deposited charges are efficiently removed a number of measurements has been performed for various incident ion intensities and temperatures.

Due to the fact, that the measured yield in the regime of several nA incident current at temperatures well above 350°C does not show any time dependent behaviour, nor does the value depend on the intensity, is a strong indication, that the measured values in fact are to be trusted and represent the total electron emission yield. In addition, the qualitative agreement of the ion current dependent yield with the simulated collection efficiency is another confirmation.

Experimentally, the emission has been measured at several intensities but only those values from regions where the yield showed no dependence on incident current have been taken into account in the present study. For the results on LiF, please refer to section I.2.3.4. The pressure in the chamber was always better than a few 10^{-10} mbar during the performed measurements. All presented data measured with this setup are measured under normal incidence.

I.2.3.2 Ion Induced Electron Emission from Tungsten

Parts of this work have already been published earlier [7, 9].

With the apparatus described in the last section, a number of measurements were performed. One of those dealt with the investigation of electron emission from a tungsten surface.

Tungsten has recently been introduced as a new material of choice for the first wall in Tokamaks (see e.g. [50]), because it exhibits favourably low sputtering yields and a very low tritium (= fusion fuel) retention as compared to the previously used carbon/graphite wall material and/or divertor tiles [51]. We measured total electron emission yields due to the impact of slow singly and multiply charged ions (deuterium, helium and carbon) on sputter-cleaned polycrystalline tungsten surfaces by using a current method in combination with a retarding grid (See section I.2.3.1). Results are presented in the eV to keV impact energy region as typical for fusion edge plasma conditions and discussed in terms of potential and kinetic electron emission.

The conditions in the boundary region of a magnetically confined fusion plasma in a Tokamak reactor, like ITER [52], are highly relevant for the production of impurities at the material boundary considered (wall or divertor plate) and their transport into the plasma core. These impurities as well as the He produced by the nuclear reaction in future D-T fusion reactors influence the radiative balance (radiation losses) and thus also change the nature and intensity of the resulting plasma-wall-interaction processes. As an important consequence, localized plasma cooling by impurity radiation may change the plasma density and temperature gradients in such a way as to give rise to internal transport barriers, leading to improvement of the overall plasma confinement.

Within this rather complex scenario, the potential drop across the space-charge sheath forming in front of a material boundary, the so-called *plasma sheath voltage* (PSV), is of particular interest, because it strongly determines the final impact energy of plasma ions and therefore the role of desorption and sputtering of the wall material. This PSV itself, however, is significantly influenced by the flux balance of charged particles in the sheath region, which depends strongly on the electron emission caused by the involved projectiles [53].

Typical species in the plasma edge region of a Tokamak are deuterium, from the fuel, impurities resulting from graphite components as well as helium from the nuclear ash. Due to the plasma conditions, multiply charged ions may play a role, especially because of possibly significant potential electron emission contributions.

The energy regime accessible by our method ranges from about 100 q eV, up to several keV. The sample was a polycrystalline tungsten sheet, chemically cleaned with acetone before installation inside the UHV chamber. Before each measurement, the sample was sputter cleaned with 2 keV Ar^+ ions under 10° incidence angle.

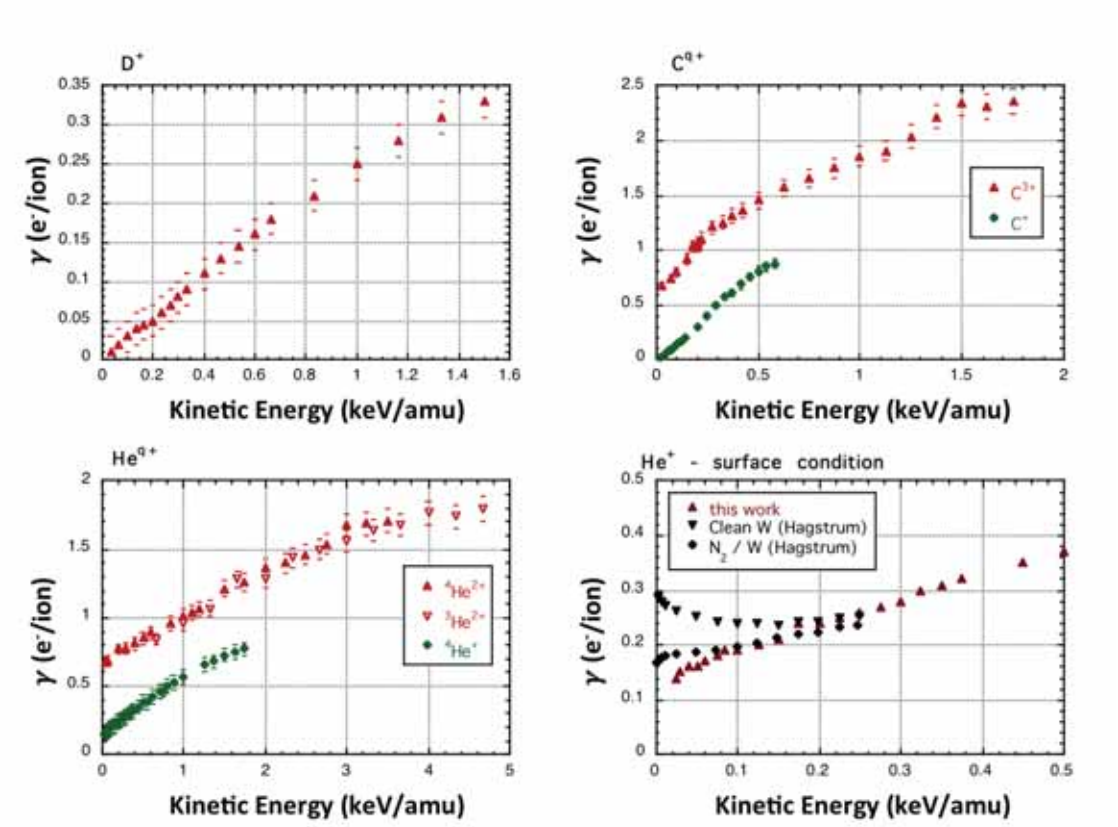

Figure I-10: Results on ion induced electron emission from a tungsten surface

Total electron emission yield from tungsten, induced by the impact of He^{q+} (lower left), C^{q+} (upper right) and D^{+} (upper left) respectively. The abscissa shows the projectiles' kinetic energy in keV/amu, the ordinate is the total electron emission yield. The presented values were evaluated from the raw current data using eq. (7) and the grid's transparency $c = 0.91$. The lower right figure shows a comparison to former measurements of Hagstrum [54] for the clean metal vs. a tungsten surface covered by a monolayer of nitrogen.

The resulting total electron emission yields for D^{+}, He^{+}, He^{2+}, C^{+}, and C^{3+} impact on the sputter-cleaned polycrystalline tungsten surface, obtained by the above described method, are presented in figure I-10 as a function of the projectiles' kinetic impact energy per atomic mass unit.

Contributions from kinetic (KE) and potential electron emission (PE) can in principle be distinguished [15]. From the experiment, the PE contribution can be estimated by extrapolation of the measured yield data towards zero impact energy. One can see, that He^{+} and all multiply charged projectile ions show clear signs of potential electron emission. In principle, for PE to occur, the potential energy of the projectile has to be at least twice the work-function of the target [54, 55].

With a value $W_\Phi \approx 4.55\,\mathrm{eV}$ for tungsten [56] PE could in principle occur for all investigated projectile ions, because the lowest potential energy involved is 11.26 eV in the case of C^{+}. However, estimates on the basis of the semi-empirical formulae of Kishinevsky [57]

$$\gamma_{PE} \approx \frac{0.2}{E_F}\left(0.8E_{pot} - 2W_\Phi\right) \qquad (9)$$

for singly charged ions and Arifov [58]

$$\gamma_{PE} \approx k\left(E_{pot} - 2W_{\Phi}\right) \tag{10}$$

for multiply charged ions respectively (with $E_F \approx 8\,\mathrm{eV}$ for the Fermi energy of tungsten [59] and E_{pot} the ions' potential energy; $k = 0.0183\,eV^{-1}$ [58]), show that significant PE yield γ_{PE} should only occur for He^+ and the multiply charged projectile ions.

	E_{pot} (eV)	γ_{PE} (calc.)	γ_{PE} (exp.)
D^+	13.6	0.03	0
C^+	11.3	0	0
C^{3+}	84	1.36	0.7
He^+	24.6	0.2	0.15
He^{2+}	79	1.28	0.7

Table I-1: Potential Electron emission characterization
The experimental values are shown in comparison to calculated ones, using eq. (9) for singly charged projectiles and (10) for higher charge-states.

In table I-1, calculated PE contributions according to eqs. (9) and (10) are compared to PE yields obtained from figure I-10, showing reasonable agreement. The systematic lower values of γ_{PE} than the calculated ones originate from the lack of surface cleanliness, as illustrated in the figure.

The surface preparation is a crucial point for electron emission studies especially at very low impact velocities, since the emission yield is very sensitive to adsorbed impurities. In order to illustrate this, figure I-10 (lower right) shows a comparison to a corresponding study about the influence of adsorbed nitrogen onto the emission yield [54]. A strong influence of even lowest contaminations was found. The curves for clean tungsten are shown in comparison to measured yields after depositing one monolayer of nitrogen on the surface. One can see, from the qualitative behaviour, that potential emission is strongly suppressed by the ad-atoms. The presented electron emission in the very low impact velocity regime does not exactly follow the values measured by Hagstrum [54]. This is probably related to the fact, that on our sample, after sputter-cleaning, still some different ad-atoms remain. Unfortunately it is not possible to clean a tungsten surface by sputtering completely, but only by flash heating the sample to temperatures above approximately 1700°C (see e.g. [60]). However, this does not apply to the other presented materials. In this work, the surface contamination of tungsten is not of great concern, since a technical environment - as present in a fusion device - does not provide atomically clean surface conditions either. The sputter cleaned tungsten surface should, on the contrary, be representative for such an environment.

Because of the fact, that the (2s $2p^2\,{}^4P$) state of C^+ is metastable, a fraction of the projectiles arrives at the sample in this excited state. In the literature, one finds a fraction of approximately 32% being present in an ion beam formed by 100 eV electron impact ionisation [61] of CO. The C^+ beam out of an ECR ion source, as presented here, can be assumed to also contain a significant amount of metastables. However, since the additional potential energy stored in the excited ion is approximately 5.3 eV [61] higher than for C^+, possible potential emission is expected to be negligible. This is in agreement with the experimental findings.

The increase of the measured electron yield with kinetic energy is related to kinetic electron emission KE. This is obvious from the fact that this increase is (practically) independent of the projectiles' chare-state as seen from a comparison between C^+ and C^{3+} as well as He^+ and He^{2+} (figure I-10). Within our experimental errors we also do not observe an isotope effect, because data for $^3He^{2+}$ and $^4He^{2+}$ coincide if plotted for the same impact velocity (or equivalently for the same kinetic energy per mass unit).

From our data in the low energy impact regime and the experience from our investigations in ref. [53] we conclude that the influence of ion-induced electron emission on the PSV in Tokamak edge plasmas with tungsten walls will be significant only for doubly- and multiply-charged ions, while singly charged ions in general do not emit a sufficient number of electrons to effectively lower the PSV.

The emission yield from W due to C^+ impact is finite even well below the classical threshold for the excitation via binary collisions at 0.1 a.u. (corresponding to $E_{kin,th}(C^+) \approx 3\ \mathrm{keV}$), as determined by eq. (3) with the above mentioned values for $W_\Phi \approx 4.55\ \mathrm{eV}$. Since there exist no promotion channels, where electron emission could occur due to the formation of quasi-molecules of projectiles and target atoms, the mechanism for the emission process is not clear. As suggested in [9], collective effects might contribute to the electron emission into the vacuum or the high energetic tail of the Compton profile might give rise to a possible collision driven emission [62].

I.2.3.3 Band structure effects in ion induced electron emission

The results shown in this chapter have already been published [10]

A commonly accepted fact is the proportionality of the energy loss, or stopping power $S = -dE/dx$ of point particles in metals in the low kinetic energy regime to their velocity v, thus $dE/dx = kv$ (see e.g. [29]). This should be valid for velocities $v < v_0$, where $v_0 = \frac{e^2}{4\pi\epsilon_0\hbar} \approx 2.18\ 10^6\ \frac{\mathrm{m}}{\mathrm{s}}$ denotes the Bohr velocity. However, due to the high resolution of energy loss spectroscopy experiments in the respective regime, deviations from this law have been observed (e.g. [63]). The proportionality is linked to the assumption of a free electron gas. When considering also *nearly free* electrons, that participate in electron-hole and bulk plasmon excitations [63], but are trapped in a way, that they do not contribute to e.g. electrical conductivity, the effective number of participating electrons to the projectile stopping can become much larger, than just from the free electrons. It was found from the energy loss of protons in Cu, that the localized d electrons do contribute to the projectile's energy loss [63] .

A recent investigation [64] provided clear evidence for the related band structure effects in the case of slow protons ($v < v_0$) through a thin gold foil. The authors found a clear change of the slope in a dE/dx plot versus projectile velocity at around 0.15 a.u., above which they claim d-electons can contribute to energy loss, whereas below this threshold velocity, only s- and p-band electrons can be excited. A further investigation of the energy loss of protons in a thin gold foil was made and a threshold value of $v_{th} \approx 0.18\ \mathrm{a.u.}$ was found [10].

Several theoretical descriptions also suggest a linear relation between the electronic stopping and the total electron emission respectively [16], therefore we performed electron emission yield measurements in the same velocity regime as in the case of stopping power discussed above. Especially, the distinct kink in the

stopping cross sections $\epsilon = S/n$, with n being the atomic density, attributed to the excitation of 5d electrons lead to the question, whether such a kink also appears in the total electron emission yield.

The results of the electron emission measurements from a poly-crystalline gold sample are presented in figure I-11. Each point represents an average value of a number of measurements. Each of these measurements covered the whole range of velocities, before re-measuring at the same projectile energy. Before each such measurement-cycle, the target was sputter cleaned.

Because of the small potential energy of the protons, potential electron emission (PE) does not contribute significantly to the total yield. Using the semi-empirical formula given by Kishinevsky, see eq. (9), with the Fermi-energy $E_F \approx 7.3$ eV [65], the projectiles' potential energy $E_{pot} = 13.6$ eV and the work function $W_\Phi \approx 5.1$ eV of the polycrystalline gold [66], one can estimate the PE yield to be roughly 0.02 e^-/ion. Concerning kinetic electron emission, we can use eq. (3) to obtain a rough estimate for the classical threshold velocity, needed to excite a conduction band electron above the vacuum level by a binary collision with the projectile. From this, we obtain a threshold velocity of about 0.11 a.u., when using the unbiased electron mass. However, as shown in the literature [17] , the usage of an effective electron mass can help to include collective effects from the solid. When doing so, and entering an effective mass $m_e^\star = 1.09\, m_e$, we find a slightly lower threshold of 0.1 a.u [17].

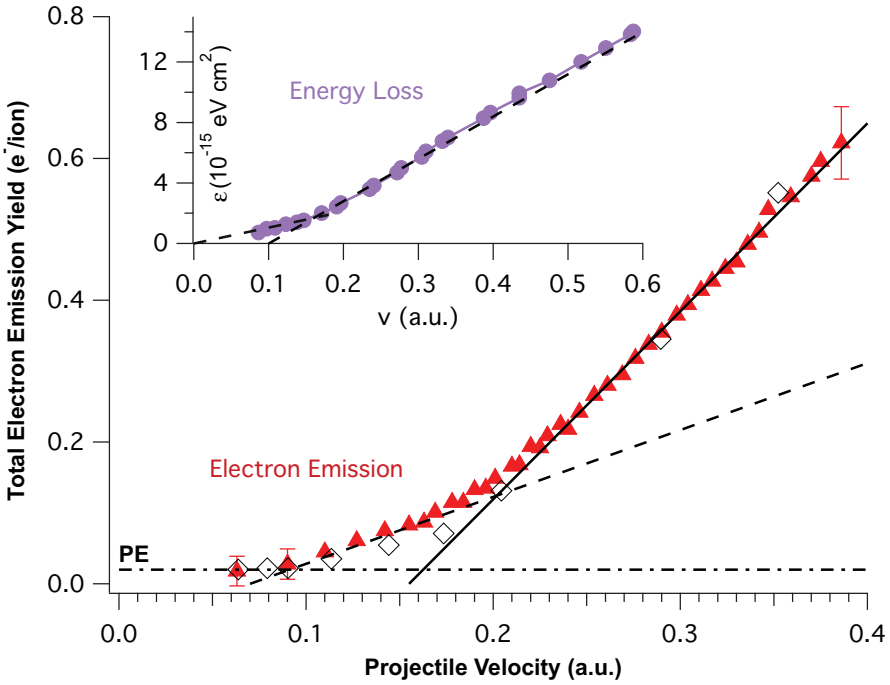

Figure I-11: Total electron emission from Au excited by impinging protons
The red triangles show electron emission yield data as a function of projectile velocity. For comparison, data from the literature [67] are included (black open diamonds). A horizontal dash-dotted line (PE) represents the estimated potential emission contribution to the total yield. The solid as well as the dashed lines indicate two regimes of rather linear velocity dependence. The insert shows the stopping cross section of protons in Au (data from [10]). For details see text. Estimated statistical errors are shown.

No significant electron emission channel due to level promotion is expected for this highly asymmetric collision system, thus, the direct collision excitation is thought to be the predominant excitation mechanism [68].

The classical threshold's location along the velocity-axis at 0.10 a.u. fits the presented measured data nicely (figure I-11) when taking the estimated potential emission of about 0.02 e^-/ion into account. In the projectiles' velocity regime between 0.10 a.u. and 0.18 a.u. the yield increases linearly with the projectile velocity, but eventually deviates from this linear behaviour above roughly 0.18 a.u. Staying in the simple picture of having (nearly) free electrons of $v < v_F$ which are excited by direct collisions with impinging projectiles, one could try to introduce the 5d electrons by (i) taking into account their higher effective work-function they have to overcome and their at the same time (ii) smaller velocity (energy), which can be accounted for by lowering the effective Fermi-energy by the same amount of roughly 2 eV [65]. Of course, this simple description ignores the localized character of the d-electrons, which makes a free-electron-approximation at least questionable, but at the same time might give a rough guess for the expected kinematic threshold for these electrons. Inserting the modified values for W_Φ and E_F into eq. (3), one obtains about 0.17 a.u. for the resulting threshold, which interestingly matches the location of the kink in the velocity dependent total yield within reasonable limits.

In figure I-11, the dashed line would therefore represent the contribution of the 6s electrons, whereas above roughly 0.18 a.u. also the 5d electrons can be ejected from the sample due to direct collisions with the projectiles. Linear fits, which also make use of previously measured data, deliver a location of the transition region where the 5d-electrons start to contribute at around 0.19 to 0.20 a.u. Eventually, a comparison between the slopes within the two different regimes, one below 0.19 a.u., the other above, leads to a factor of 2.86 in the case of electron emission, which can be compared to roughly 2.4 for the electronic stopping power, as shown in the insert.

In summary, we report the observation of a rather sharp, distinctive threshold for the specific emission of 5d-electrons from a gold surface by proton impact, below which only 6s electrons contribute to the total electron emission. The values are in good quantitative agreement with semi-empirical estimates and qualitatively fit to corresponding measurements of the electronic stopping power [10].

I.2.3.4 Electron emission from LiF

Parts of this work have been published earlier [8].

The recently discovered effect of ion-guiding through insulating capillaries (see Part 2 of this work) has revived the fundamental interest in the interaction of charged particles with surfaces in particular insulating ones [15, 69-74]. For insulator surfaces a severe difficulty in ion beam experiments is caused by the generation of electrical charges at the surface. Both the impact of positively charged ions and the consequent electron emission contribute to a positively charged surface layer. This charged layer does not only change the impact energy and beam geometry, but also the energy distribution of emitted charged particles. Since their energies are usually very low, even a charging by less than a Volt can severely influence measured total yields of charged secondary particles.

In this context the ion-induced electron emission yield is a quantity of interest. Surprisingly high electron yields from insulator surfaces are found experimentally [15, 70-73] for single ion impact events. The involved mechanisms are still a matter of investigation and debate (see e.g. [15] and references therein for a detailed review on the topic).

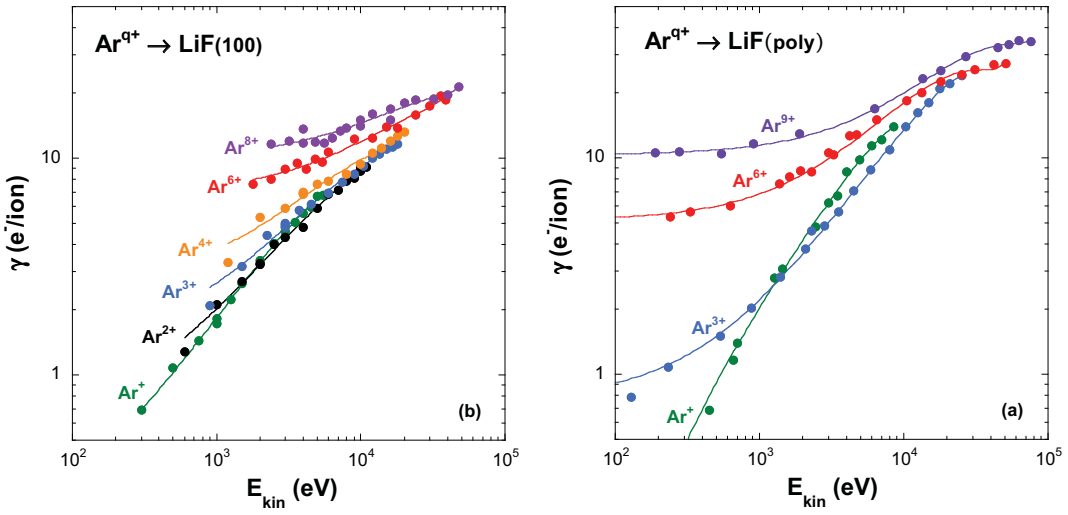

Figure I-12: Total electron emission yield from LiF due to the impact of Ar^{q+} projectiles (q=1..9)
The yield in the case of the LiF(100) single crystal (left) was measured using the current method described in this work (see I.2.3.1), and compares well to values taken from [26] (right). The lines are shown to guide the eye only.

Electron emission in single ion impact events (i.e. in cases where the subsequent ion impact event takes place after a time long enough that the charge generated by the previous impact event could be removed) can only be measured by special techniques, for example the method of electron emission statistics (ES), described e.g. in [74, 75] or in section I.2.4.2 of this work. For the more conventional method of determining total electron emission yields via measuring the current of emitted electrons and the current of incoming ions (current method CM, see section I.2.3.1), more intense ion beams (> nA) are necessary, which tend to charge-up the insulating samples. For reliable electron emission yield measurements using CM, the building-up of charge at the surface has to be overcome by one of several ways:

- Flooding the target with charge carriers of appropriate polarity (e.g. low energy electrons) in between ion pulses.
- Deposition of insulating target materials as thin (µm) or ultra thin films (nm) on metallic substrates, to reduce the electrical resistance of the surface layer.
- Heating of a sample up to temperatures where it becomes a good ionic conductor.

In particular the latter method is very well applicable in the case of alkali halide targets [46, 71]. As shown in detail in section I.2.3.1, a target heating was

introduced into the existing electron emission measurement setup using a current method and successfully tested in a number of proof-of-principle measurements.

It is well known (see section I.2.2) that electron emission due to the impact of ions onto a solid consists of two contributions, namely kinetic (KE) as well as potential emission (PE). These can in most cases be treated as being independent from each other. Whereas PE is an effect purely driven by the potential energy of the ions due to the direct or indirect recombination of electrons into the empty shells of the ion, KE is caused by the projectiles' movement through the target. For PE to occur, the potential energy, i.e. the sum of ionization energies, has to exceed twice the work function in the case of metals or twice the binding energy in the case of an insulator.

In the case of LiF as target material, this minimum potential energy is about 25 eV. Therefore, the electron emission of Ar^+ from LiF, as presented in figure I-12 is of purely kinetic nature. In this figure we compare the results obtained during this work by measurements using the current method (see chapter I.2.3.1 for details about the experiment) for Ar^{q+} (q = 1, 2, 3, 4, 6, 8) ion impact on a LiF(100) single crystal with previous data measured for Ar^{q+} (q = 1, 3, 6, 9) ion impact on a thin polycrystalline LiF film using the electron statistics method [25, 26]. The good agreement between these two sets of measured data, both in impact energy dependence and absolute magnitude of the total electron emission yield, demonstrates that our measures to prevent a macroscopic charging of the single crystal surface were sufficient. Small remaining differences could be a result of differences in the targets used (a thin polycrystalline LiF film vs. a bulk LiF(100) single crystal). The measurements presented in this work even show slightly higher electron emission yields at very low impact velocities, which is also a good indication, that charging effects do not play any significant role.

The qualitative discussion on the underlying mechanisms for KE and PE presented in [25, 26] is also valid for our results.

Since the measurement technique provides reliable data in comparison with the literature, we could use the same method for the investigation of the electron emission from LiF due to impact of xenon ions, which are especially of interest to correct previously measured yields from the emission for very high chare-states ($q > 20$) [46]. There, just the potential electron emission was of interest, in order to compare with predictions from the classical over-the-barrier model [76], thus, the kinetic contributions had to be subtracted. At that time, the KE contribution was estimated by using the Ar^+ data from [26]. We now find good qualitative agreement of the Ar^+ and the Xe^+ induced electron emission yields from LiF (figure I-12, figure I-13).

While in [46] KE-contributions to the observed total electron emission yield could only be roughly estimated, we can now use the data for low chare-states, especially from Xe^+, to separate PE and KE in the case of highly charged ions (e.g. Xe^{20+}).

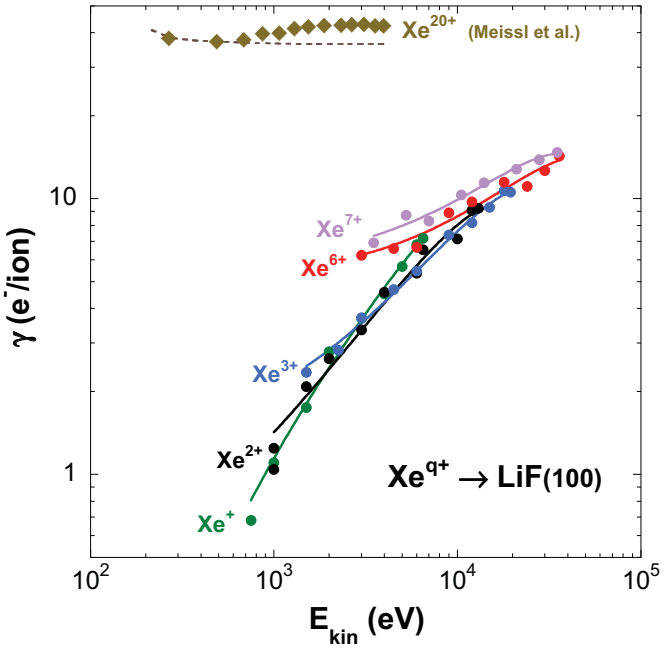

Figure I-13: Total electron emission yield from LiF due to the impact of Xeq+ projectiles (q=1..7,20)
The electron emission yield from a LiF(100) single crystal is plotted as a function of the projectiles' kinetic energy. The lines are shown to guide the eye only. Data for higher charge-states (Xe^{20+}) are included (data from [46]). A distinct crossing of the Xe^{+} curve with higher charge-states, even more pronounced than for Ar^{q+} projectiles is found.

The new data on Xe^{q+} (q = 1, 2, 3, 6, 7) ion impact on a LiF(100) single crystal are shown (figure I-13) and compared to recent results obtained for Xe^{20+} ion impact [46]. In this figure the contribution from potential electron emission for Xe^{20+} projectiles obtained by subtracting the kinetic contributions is indicated by a dotted line. One can see, that in this impact energy regime PE exceeds KE by at least one order of magnitude for such a high chare-state.

In conclusion we have demonstrated, that the problem of macroscopic surface charging due to an incident ion beam can be overcome in the case of LiF by heating the sample to a temperature above approximately 370°C and a simple current method can be used to reliably determine the electron emission yield from such a surface. With this method we have studied electron emission from a LiF(100) single crystal due to impact of singly and multiply charged Ar and Xe ions. Our results compare well with previous data and can be used to estimate the KE contribution to the total emission yield in the case of considerably higher charge-states of Xe.

An interesting observation is the distinct crossing of the electron emission yield curves for Ar^{+} and Xe^{+}, respectively, with the corresponding higher charge-state curves, i.e. that the electron emission yield increases more strongly with the projectiles' velocity than for higher charge-states and eventually becomes even larger above the crossing velocity. An interpretation of possible underlying mechanisms can be found in [27].

I.2.3.5 Comparisons

There are several interesting questions related to electron emission from surfaces, especially from insulators. One of them deals with the existence of molecular effects in electron emission. Numerous investigations have been published so far concerning this topic (see e.g. [77-79]).

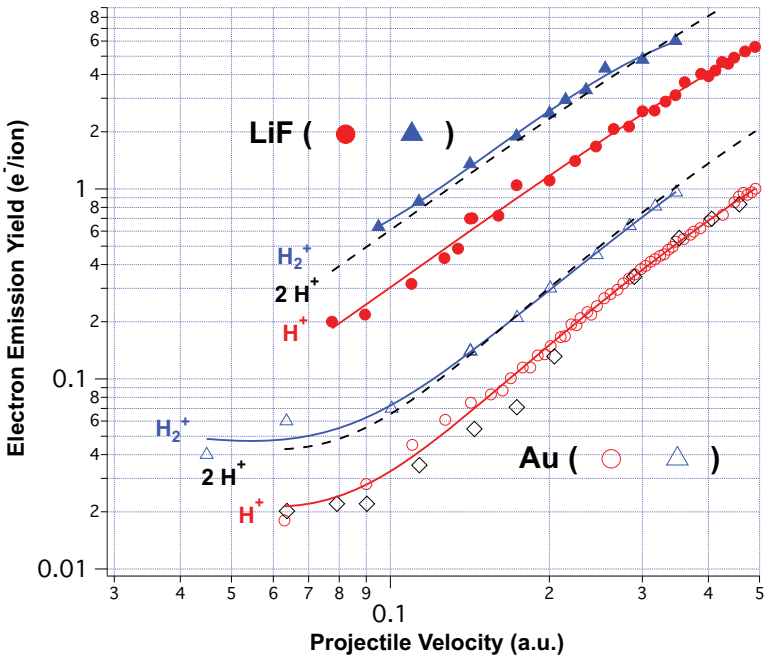

Figure I-14: Electron emission yield comparison from Au and LiF for H^+/H_2^+ projectiles
As a function of projectile velocity, the total electron emission yields plotted for protons (red) in comparison to molecular hydrogen (blue). The lines are drawn to guide the eye only. For comparison, the emission due to impact of two individual protons is included (black dashed). Reference data from the Literature [67] are shown (black open diamonds).

We measured total electron emission yields from gold and LiF with the current method presented in section I.2.3.1 for both, protons H^+ as well as molecular hydrogen ions H_2^+. The used samples as well as their treatment and the measurement procedure have been discussed in detail in the previous sections.

A first feature, which can easily be seen in figure I-14 is the large discrepancy of the electron emission yield from gold and LiF. Especially noticeable is the fact, that LiF has a wide band gap and a large ionisation energy has to be transferred in order to cause emission into vacuum (ionisation energy of the F^- 2p valence electron $E_{ion} \approx 12$ eV [80]), but still, the electron emission yield is much higher than from gold, where much less energy transfer is needed to eject an electron ($W_\Phi \approx 5.1$ eV [66]). This has been interpreted in the past as a consequence of the much larger inelastic mean free path an excited electron experiences in the insulator, as compared to the metal. Therefore, contributions from deeper inside the solid add to the total emission yield, whereas, in the case of metals, only electrons out of a thin surface region can escape into vacuum (see e.g. [46]).

Concerning possible molecular effects, one can compare the electron emission from two individual protons, which is simply twice the value, that one projectile causes, with the emission yield due to impact of the H_2^+ molecule. As can be seen in figure I-14, there is no significant difference from the gold sample. At low impact velocities, the statistics does not allow any conclusive statement. However, in the case of the LiF(100) target, a very small, but systematic shift of the molecular electron emission is observed, as compared to the individual protons. Unfortunately, no more detailed investigations have been performed so far, but it might be worth for future experiments to take a closer look at this effect.

Driven by the recent discovery [81], that the energy loss of slow protons through a thin film of LiF shows a distinct threshold velocity of 0.1 a.u., below which no electronic stopping of the projectile occurs, we take a look at the corresponding threshold behaviour concerning electron emission.

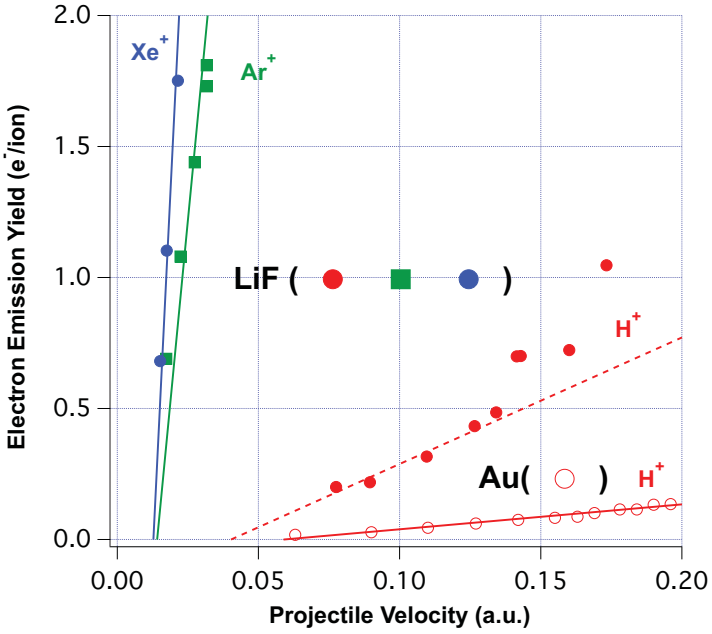

Figure I-15: Total electron emission yield from Au and LiF in the low impact velocity regime
The velocity dependence of the yield is shown for Xe^+ (blue), Ar^+ (green) and H^+ (red) projectiles. The solid lines are the result of linear fits to the shown data (the dashed line only includes a subset of the presented points). The solid lines agree well with the liner behaviour of the velocity dependence, whereas in the case of the emission from LiF by protons, the linearity is not distinctive enough to allow a proper extrapolation to the axis.

In order to determine experimental values for the threshold velocities, below which no further electron emission occurs, we use linear fits to the low velocity data (figure I-15) and extrapolate them to intersect the axis. For gold as a target material, we have to take into account a contribution from potential electron emission, as discussed in section I.2.2. This is estimated to a value of $\gamma_{PE} \approx 0.02\ \mathrm{e^-/ion}$ and has to be subtracted from the total measured yield. Potential emission from LiF needs not to be taken into account, because of the large

ionisation energy of the involved target electrons, which makes PE impossible for the projectiles shown here.

One immediately realises the high linearity within the shown regime in the case of Ar^+ and Xe^+ impacts on LiF as well as in the case of protons impinging on a gold surface. Unfortunately, the data for proton impact on LiF do not reach such low velocities as obviously necessary to obtain a reasonable threshold value, because the behaviour is rather non-linear, even in this small velocity region.

		v_{th} (a.u.) exp.
LiF	**Xe^+**	0.013
	Ar^+	0.014
	H^+	0.04*
Au	**H^+**	0.1

Table I-2: Threshold velocities
Experimental values are extracted from the data shown in figure I-15. The value for H^+/LiF (*) is not reliable due to the non-linear behaviour of the electron emission as a function of velocity. Theoretical values according to the classical threshold velocity are calculated from eq. (3).

Nevertheless, it is obvious from the data, that at 0.1 a.u. still significant electron emission occurs, which is astonishing due to the non-existing electronic stopping of the projectiles, observed in a thin film [81]. A possible explanation is the fact, that the electron emission could well be attributed to nuclear stopping, through a promotion channel, or simply the different sample conditions.

In contrast to electron emission into the vacuum, one can also study the internal excitation of electrons, which is too small to overcome the vacuum barrier.

A sandwich structure of two metallic layers, separated by a thin layer of insulating material, has been used to study this internal excitation. The thin insulator between the two metallic layers acts as a tunnel barrier, through which a current can be measured, that is related to the electronic excitation. We could measure nice dependencies of this tunnel current of e.g. the projectiles' charge-state, showing the importance of effects related to the potential energy of the impinging ions onto the internal excitation inside the bulk. Related work has been published in [4, 11].

I.2.4 Cluster induced EE

I.2.4.1 Introduction

Electron emission due to ion impact onto a solid surface is, as already discussed in the last sections, a still investigated topic. Due to progress in the production of high-brilliance cluster beams in the 1990s, nowadays the investigation of the interaction of such clusters with surfaces gets into the focus of several research groups, both experimentally and theoretically (see e.g. [77, 78, 82-87] and references therein). Besides sputtering, landing, and other phenomena, which are intensely studied, we wanted to investigate the phenomenon of electron emission

under impact of such clusters onto metallic and insulating surfaces. The clusters are especially interesting projectiles due to their high mass and, therefore, very low impact velocities down to the order of a few thousand meters per second.

As already discussed in earlier sections (see I.2.2), potential electron emission can be excluded in the presented experiment, therefore purely kinetic effects or other phenomena contribute to the observed electron emission. When considering the kinematic threshold for electron emission (e.g. section I.2.2), one soon realises, that for such slow particles, the direct collisional excitation becomes practically impossible. Therefore, other excitation mechanisms have to be considered, as it seems.

I.2.4.2 Experiment

The aim of the experiment was to measure the emission statistics from a gold (111) as well as from a LiF (100) single crystal under impact of light (>2) to heavy (~1000) singly charged Copper clusters Cu_n^+. The angle of incidence was 45°.

The experiments have been performed at the magnetron cluster source in Caen, France [85]. This source is capable of providing metallic clusters from the monomer up to several thousands of atoms. For the detection of the emitted electrons, we used a setup, which has been successfully used in the past to measure electron emission statistics at highly-charged-ion impact [46, 88, 89].

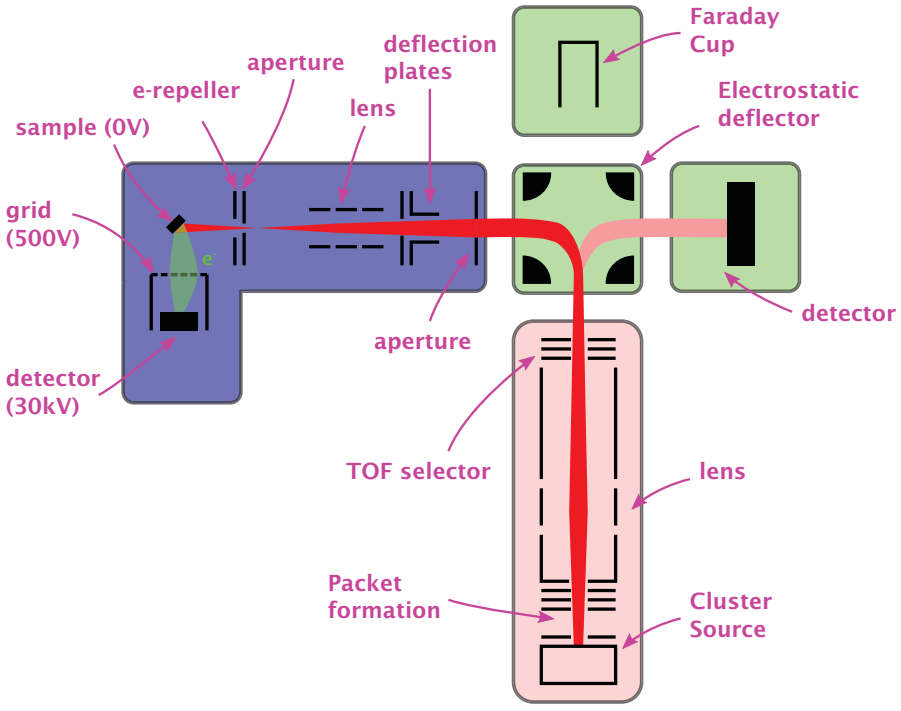

Figure I-16: Experiment Overview
The setup consists of several blocks: the source (red), the primary beam diagnostics and manipulation (green), as well as the electron emission measurement beamline (blue).

The experiment consists of the cluster source, with a time-of-flight (TOF) line, to separate the mass contributions (see figure I-6). Behind this track, an electrostatic deflector allows to guide the ion beam into the beamline or, alternatively, onto a detector for TOF measurements. Thus, mass determination of the clusters. The cluster acceleration voltage was varied between 1.5 keV and 4 keV.

The experiment's beamline (figure I-16, blue) uses two UHV chambers, one differential pumping stage and the collision chamber, both pumped via turbo molecular pumps. The base pressure in the collision chamber was as good as 10^{-10} mbar during the experiments.

The magnetron sputter source produces a large range of masses, which are, in a first step, extracted in some packets of some µs length. These packets are accelerated in a two-step dynamic electric field process causing a significant energy spread of the projectiles later on. A set of separation electrodes is used to select a TOF slice at the end of the field free drift track, before the beam enters an electrostatic 90° deflector. This can be used to pass the beam into a specific detection system, where the ions are decelerated to some 10 keV before hitting an electrode, where secondary electrons are emitted and eventually detected by a PIPS detector, similar as the equipment at the measurement beamline. This SE detection is used to determine the cluster size via time-of-flight measurement before sending it to the experiment's beamline by changing the deflection direction.

After entering the first differentially pumped chamber through a 5 mm aperture, the beam passes a set of deflection plates and an electrostatic einzel-lens, which is used to focus the beam onto the target. In between the lens and the target, a 2 mm aperture is used to cut the beam directly in front of the target. Right behind the aperture, a negatively biased (-60 V) suppressor electrode is used to avoid electrons from the aperture to reach the electron detector.

The electron detection system is in principle identical to the one, used in an earlier measurement at the Heidelberg EBIT [90]. For detection of the electrons, it uses a passivated implanted planar silicon (PIPS) detector (Canberra GKPD100-12-300AM), which is an energy dispersive detector, providing an energy resolution of about 7 keV. By applying a high voltage of about 30 kV to the detector, electrons are accelerated to an impact energy of 30 keV, thus the deposited energy within the integration time of the system is directly related to the number of electrons by $E_{tot} = n * E_1$, where $E_1 \approx 30\ \mathrm{keV}$ is the deposited energy per electron. In fact, one also has to take into account backscattered electrons, which deposit only parts of their kinetic energy within the detector, as discussed in more detail a bit later in this section.

The electrons, after being emitted from the sample (or the projectile), are accelerated towards a grid, which is biased about 500 V. For the low kinetic energy projectiles (1.5 keV) only, the grid voltage was reduced to 150 V to avoid significant deflection of the projectile beam. In a number of measurements it was assured, that the collection efficiency does not significantly change within this voltage range.

The beam impinges on the sample under an incidence angle of 45°. We used a circular gold (111) single crystal sample with an active diameter of about 6 mm. The gold was held by a stainless steel ring, facing the beam. The whole sample holder was mounted on a vertical rod, which could be moved by a mechanical manipulator in all the spatial dimensions and was rotatable by 360°.

The second sample, a LiF(100) single crystal was mounted on the same holder, about 40 mm below, and could be moved into the beam by the vertical linear travel. This sample covered the whole holder width (11 mm). In order to avoid possible charging of the sample surface, the LiF crystal was heated to about 100°C. The temperature was monitored by a K-Type thermocouple mounted close to the sample.

Sample positioning was done by moving the holder in both lateral directions and monitoring the measured electron count-rate at the same time. Because the electron emission statistics for all projectile species had a significant 0-electron contribution (in contrast to the impact of highly charged ions), a change of the mean emission yield results in a changing count-rate, which represents the emission rate of at least one electron onto an impact. Due to this fact, a weak material-, and geometry-dependent contrast can be seen, allowing to identify the sample position by looking at a flat plateau in the electron yield lateral scan.

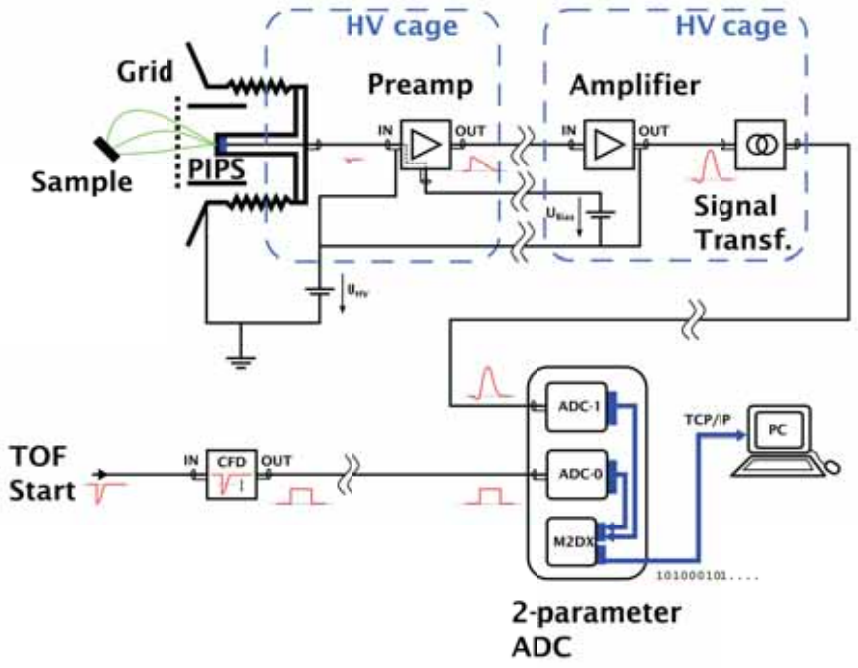

Figure I-17: Measurement Electronics and Data Acquisition
The detector inside a UHV chamber provides pulses, which are processed by a two-stage-amplification. The whole detector equipment is at high voltage, thus, the signal is eventually transferred to ground potential via a signal transformer. The pulse height is fed into the second channel of the 2-parameter ADC, the first one is supplied by the start pulse of the ion source extraction. Shown pulse-shapes are illustrative only. For details see text.

A schematic illustration of the electric circuits is shown in figure I-17. The PIPS detector is connected to a preamplifier (Ortec 142), which produces proper pulses in the mV regime and feeds the applied bias voltage of 50 V to the detector. The preamplifier was directly connected to the flange, holding the detector inside the vacuum. The whole flange as well as the preamplifier are located inside a HV cage, because they are operated at the detector potential.

This first cage is connected to a second HV cage in a rack, containing a mini NIM rack. The signal is transferred from the HV cage to ground potential via a signal transformer and afterwards fed into one channel of a 2 parameter ADC system M2DX by the JKU Linz [91]. The start signal from the ion source's extraction system is wired to the other channel of the ADC. The ADCs (Canberra 8715) are operated in coincidence mode, with the master being the start pulse, thus, impact timing information with respect to the start pulse is available.

The M2DX software stores all events, including the timing information into binary files, which are processed later on for evaluation purposes. By using this 2-parameter system, the mass information is acquired in combination with the data about electron emission at the same time.

After passing the grid, the electrons are, as already mentioned, accelerated towards the detector potential. This was varied between 25 keV and 30 kV. Due to the low electron emission yields, as compared to the case of MCI or HCI impact, field emission had to be avoided. Because of the fact, that at the highest possible detector voltages after some time of operation sudden bursts of electron emission occurred and therefore caused rather unpredictable and quite considerable background, the detector voltage was usually lowered during the day.

Nevertheless, before and/or after each measurement, a dark spectrum was recorded, which eventually was used in the evaluation procedure to subtract the estimated background. These dark spectra were recorded in the same way as the actual electron emission measurements and used in the evaluation procedure later on.

In order to obtain the correct electron emission number distribution W_n, with $\sum_{n=1}^{\infty} W_n = 1$, the physical spectra have to be interpreted first accordingly. As already mentioned earlier, the measured spectra $f(E)$ represent the energy deposition in $[E, E + dE]$ inside the detector. The detected electrons on impact have a kinetic energy of E_0. Following the considerations in [92], the measured spectra can be understood as a superposition of functions $f_n(E)$, representing the contribution due to the emission of i electrons, thus

$$f(E) = \sum_{n=0}^{\infty} c_n f_n(E). \tag{11}$$

Each of these i-electron contributions reflects the fact, that not the total energy of all involved electrons is deposited in the detector, but instead some of the electrons are backscattered, causing less energy to be measured. When assuming a simple alternative decision process for the backscattering, with a probability p_{BS}, a binomial statistics $P_n(m)$ describes the probability of m–fold backscattering for n electrons to occur. Such a reflected electron deposits about 60% of its kinetic energy inside the detector, thus an energy lowered by δE. The deposited energy of n emitted electrons appears as a Gaussian in the spectrum, centred on nE_0, with a width ΔE, determined by the energy resolution of the detector and the electronics. For those electrons, which have undergone m-fold backscattering, the energy spectrum appears as Gaussian as well, with an increased width of

$$\Delta E_m = \sqrt{(\Delta E)^2 + m(\Delta E_{BS})^2} \tag{12}$$

and centred around an energy, which is m-times lowered by δE, thus

$$E_m = nE_0 - m\delta E. \tag{13}$$

The complete n-electron contribution to the whole energy spectrum takes then the form [75]

$$f_n(E) = \sum_{m=0}^{n} P_n(m) g(E; E_m, \Delta E_m) \tag{14}$$

where $g(E, \mu, \nu)$ are normalized Gaussians around μ with width ν. The actual n-electron contributions c_n can eventually be determined by fitting a measured spectrum with eq. (11). The fitting procedure usually constrained the peak spacing to a fixed value, which was determined by the calibration procedure mentioned earlier. The width of the primary Gaussian ΔE was fixed. Usually, the peak position for the 1-electron peak was also fixed, according to the calibration measurements.

For fitting a spectrum, the backscattering probability was chosen between 0.18 and 0.25, depending on the detector voltage E_0. The energy resolution of detector and electronics was determined from the fit-functions to be about 10 keV. For the energy broadening for backscattered electrons ΔE_{BS}, a value of 12.6 keV was used.

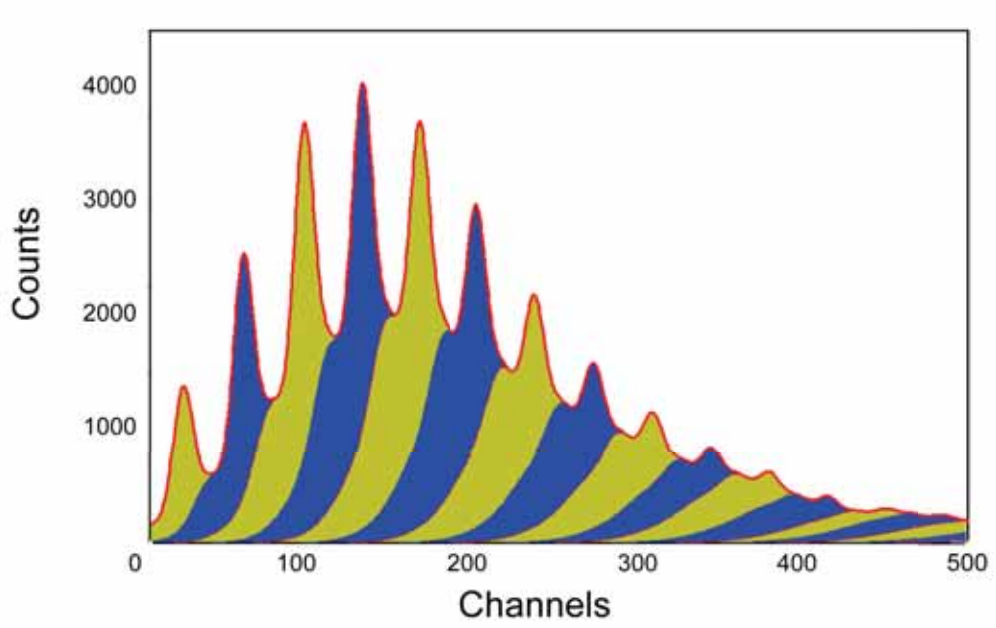

Figure I-18: Illustration of the multiple energy contributions to the measured energy spectra
An example energy distribution for the impact of O^{6+} on gold. Figure taken from [46]. The colour-coded areas show the contributions of the individual n-electron distributions according to eq. (14).

An illustration of the contributions due to the detection of n electrons can be seen in figure I-18. The colour code indicates the various distributions stemming from the corresponding electron number. One can see, that especially for higher electron numbers, the backscattering contributions can become even larger, than the primary peak.

Prior to the measurements, three spectra were taken at three different detector voltages E_0, at 25 kV, at 27 kV and at 30 kV. By analysing the peak shift as a function of detector voltage, the ADC channel numbers were calibrated.

It has to be pointed out, that due to the repetition rate of the cluster emission from the source of 1 kHz, the maximum impingement rate was limited in order to avoid multiple hits by ions of similar masses. Within one frame, i.e. between two subsequent start-pulses from the ion source extractor, usually only the first event was actually counted, in order to avoid pile-up from the preamplifier, which has a rather large decay-time of the resulting electronic pulse upon one event of about 1000 µs.

The electron spectrum is measured at the same time as the time-of-flight, which in principle would allow measuring a large range of masses at the same time. However, because of ion optical problems, and also the fact, that it was not clear, how the number of ions per time interval in one frame was actually distributed, usually narrower mass distributions were measured. Eventually, in the evaluation process, the masses were cut into reasonable slices before processing the resulting electron statistics spectra.

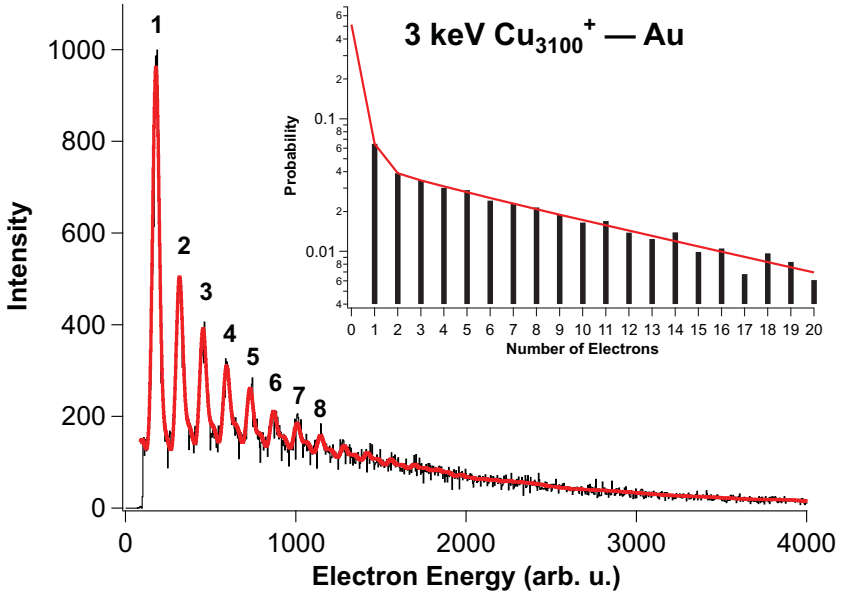

Figure I-19: Example statistics spectrum

An example energy spectrum as measured with the detector. The red line is a fit according to eq. (11). The insert shows the resulting number distribution with a 0-electron component from a fit (red line). See text for details.

After measuring a raw energy spectrum and cutting a proper mass-slice out of the acquired data, the underlying number distribution W_n was evaluated by fitting eq. (18) to the spectrum (figure I-19). As already mentioned, a corresponding dark-spectrum, which was recorded right before and/or after one measurement was rescaled in accordance to the measurement duration and subtracted from the measured energy spectrum.

A complete number distribution, of course, needs also a proper 0-electron component W_0, i.e. the probability, that no electron is emitted upon ion impact. The method described here is not capable of delivering this probability, because the ion impact is not independently determined. Therefore, in order to be able to get a reasonable number for the total emission yield, one has to fit a distribution to the measured number spectra.

The total electron emission yield, i.e. the mean number of emitted electrons is defined by

$$\gamma = \sum_{n=0}^{\infty} nW_n. \tag{15}$$

The number distribution, of course, fulfils the normalisation condition

$$\sum_{n=0}^{\infty} W_n = 1. \tag{16}$$

As suggested in [80], the electron emission statistics can be fitted by a two parameter Pólya-distribution

$$W_n(\gamma, b) = \frac{\gamma^n}{n!}(1 + b\gamma)^{-\left(n+\frac{1}{b}\right)} \prod_{i=1}^{n}[1 + (i-1)b], \tag{17}$$

with a second parameter b, besides the mean number of electrons γ, which determines the deviation from a Poisson (for $b = 0$ the Pólya distribution becomes equal to a Poisson distribution). The meaning of this parameter has been interpreted as the strength of cascades in electronic excitation processes [93].

Unfortunately, in most cases it was not possible to fit the acquired spectra with a law like eq. (17). However, only for the low electron contributions the deviations were significant. Therefore we decided to use a law, which allows in addition a Poisson contribution, thus our fit law is defined by

$$W_n\left(\gamma; c_1, \lambda_1, c_2, \lambda_2, b\right) = \mathrm{c}_1 \frac{\lambda_1^{\,n} \mathrm{e}^{-\lambda_1}}{n!} + \mathrm{c}_2 \frac{\lambda_2^{\,n}}{n!}(1 + b\lambda_2)^{-\left(n+\frac{1}{b}\right)} \prod_{i=1}^{n}[1 + (i-1)b], \tag{18}$$

with the unknown fit parameters c_1, λ_1 for the Poisson and $c_2, \lambda_2,$ and b for the Pólya distribution. Most of the acquired data could be fitted with this law. Nevertheless, no physical interpretation can be given yet; it just seems, as if another low-electron-emitting process is superimposed a standard electron emission process, which follows the Pólya distribution from eq. (17).

Possibly, the background subtraction does not contribute to all effects, which influence the measurement negatively. A process, which is driven by the incident beam, e.g. some secondary electrons from a different source than from the sample could well be the reason for the low-electron Poisson contribution. Therefore, we also investigated the measured Pólya-contribution alone in comparison. These investigations are still going on and are therefore not included completely in this work, where just a qualitative impression on the effects can be given.

I.2.4.3 Results and Discussion

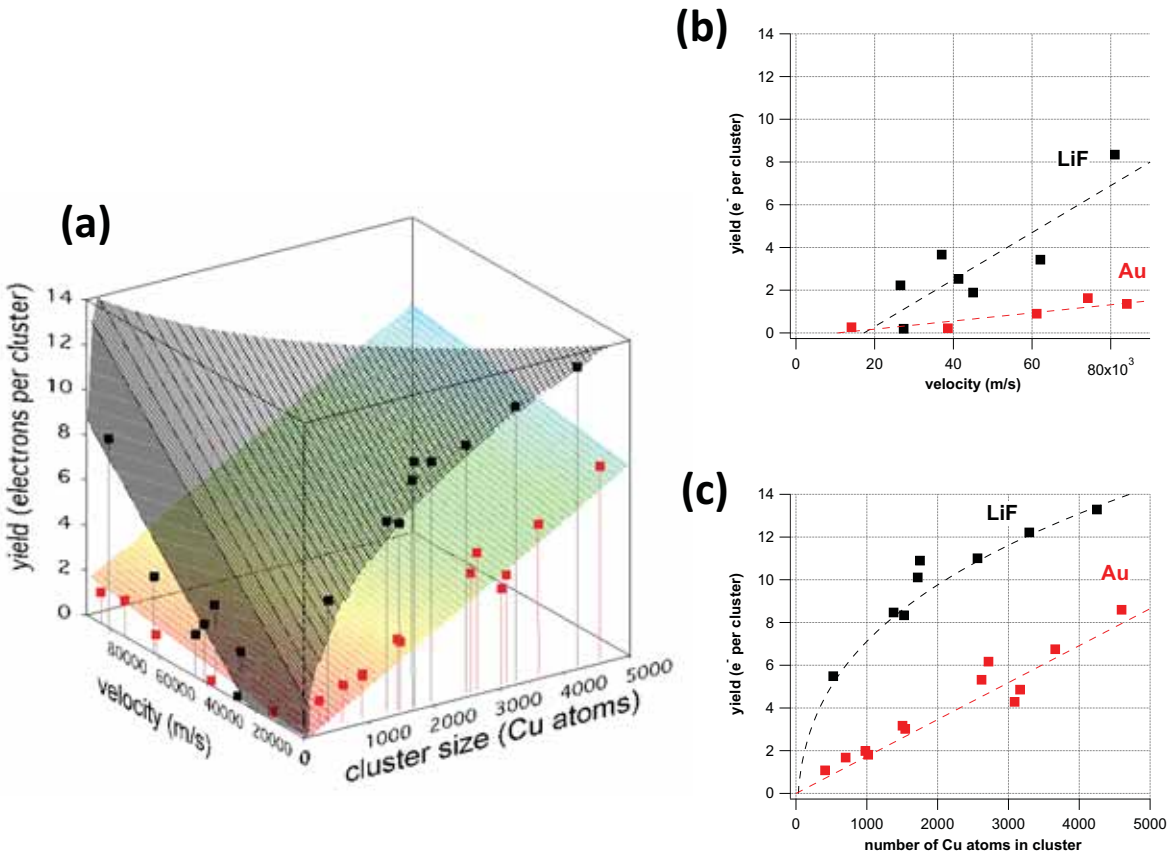

Figure I-20: Preliminary total emission yield data as a function of cluster size and impact velocity
The results for gold (red) and LiF (black) differ remarkably. In (a) the electron emission yield per cluster impact is shown as a function of cluster size and projectile velocity. Just small cluster data (Cu_n^+; $n < 300$) as a function of velocity is shown in (b), whereas (c) includes only data at low impact velocities ($v < 5000\,m/s$) as a function of cluster size. The coloured surfaces and lines, respectively, are included to guide the eye only.

Out of the measured electron statistic spectra, we determined the mean number of emitted electrons γ for emission from gold as well as from LiF by fitting eq. (18) to the number distribution.

The data evaluation is only of preliminary nature, there are further investigations going on. But first impressions can be found, when plotting the evaluated yield values as a function of cluster size and velocity (figure I-20). One remarkable fact is the much larger emission yield from LiF as compared to the one from the gold sample. On the other hand, they both exhibit an increasing yield with cluster size as well as with the projectile velocity, as can be seen in the figure.

For LiF, however, the increase of the total yield with cluster size is much weaker than in the individual limit, i.e. if all cluster atoms would contribute equally. Or, form another point of view, the yield is not proportional to the cluster size. On the contrary, at lower masses, a steep increase of the yield appears, which rapidly flattens towards larger clusters.

Eventually, we investigated the surface of the irradiated samples with contact mode AFM under ambient conditions, in order to find out, whether remaining droplets or similar obstacles can be found due to the irradiation. Unfortunately, up to now, the images did not allow to draw any conclusions. XPS or AES investigations could be useful to determine the amount of copper on the surface before further steps are taken.

I.2.4.4 Summary

Electron emission from surfaces caused by ion bombardment has been intensively studied in the last decades (see e.g. [15, 16] and references therein) but still there remain some open questions concerning the fundamental processes. Especially the occurrence of electron emission below certain threshold impact velocities is still drawing attention (see e.g. [9, 10, 62] and references therein).

We measured electron emission statistics from metal (Au) and insulating surfaces (LiF) under the bombardment with singly charged copper clusters Cu_n^+ (n~1-8000) in the kinetic energy regime between 1.5 keV and 4 keV provided by the magnetron sputter cluster source available in the ARIBE facility at GANIL, located in Caen [94]. The projectile velocities reach values well below the classical threshold for kinetic electron emission.

We used an existing setup for the electron number statistics measurements described elsewhere [46, 88]. The emitted electrons are collected from the sample by an electric field and afterwards accelerated to 30 keV. These electrons hit a surface barrier detector, which gives a signal proportional to the deposited energy, thus the number of electrons detected within the integration time.

The measurement showed, that even for impact velocities as low as approx. 1500 m/s, electron emission occurs and shows large differences between the investigated insulating and metal sample, respectively.

Although a detailed interpretation still has to be developed, one could think of two possible involved mechanisms, one being driven by direct collisional effects, the other being a consequence of local surface heating (see e.g. [9, 18, 95]).

Further results of cluster induced electron emission from gold and LiF will be reported in the PhD thesis of Katharina Dobeš.

I.3 SURFACE NANO-STRUCTURING

Parts of the work described here have already been published [12, 13].

I.3.1 Introduction

The use of slow (eV–keV) highly charged ions (HCI) as a novel tool for gentle surface nano-structuring [96-98] has raised considerable interest of researchers in recent years and a variety of materials have been considered for investigation [99, 100].

In a highly charged ion Z^{q+}, considerable potential energy is stored during its production when q electrons are removed from an originally neutral particle, e.g.

14 keV for Ar^{18+}, 121 keV for He-like Xe^{52+} and 250 keV for Ne-like Th^{80+} (see section I.2.2) [101].

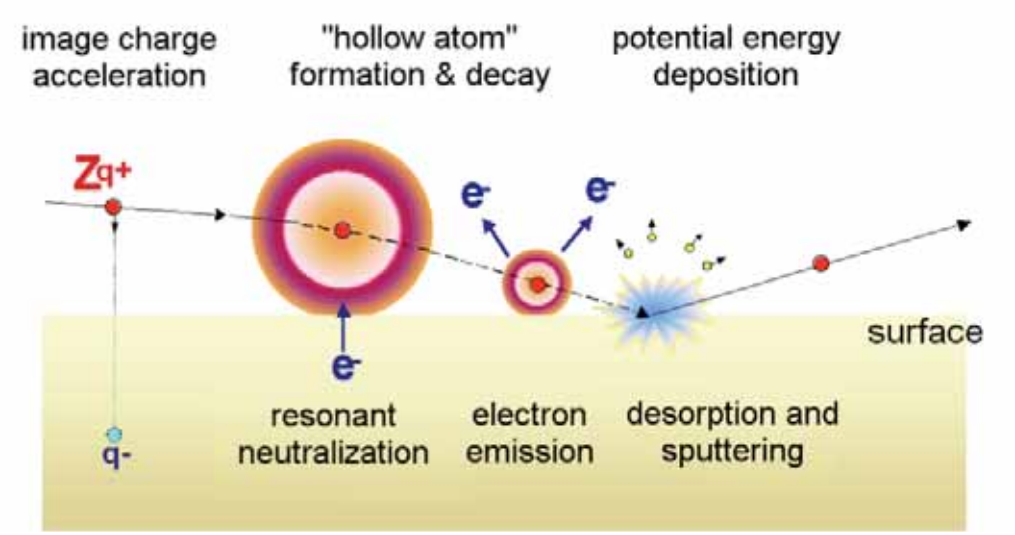

Figure I-21: Scenario of the interaction between an approaching HCI at a metal surface
For details see text. Figure taken from [36].

Nowadays, there exists a commonly accepted scenario, describing the interaction of such a highly charged ion with a surface [15, 36, 96, 102, 103], eventually leading to the neutralisation of the projectile, and thereby releasing its potential energy.

According to this scenario (see figure I-21), a very highly charged ion when approaching the surface is accelerated towards the sample by its own image charge. This acceleration defines a minimum kinetic energy that the HCI can reach at its final approach. The neutralisation of the projectile then starts with the formation of a transient, multiply-excited particle with some empty inner shells, a so-called "hollow atom"(HA) [39]. In the case of metallic targets, the above surface part of this interaction can be well described by the "classical over-barrier model" (COB) [102] and leads to the emission of a large number of low energy electrons. As soon as the HA comes very close to the surface, it gets screened by the metal electron gas, causing further emission of electrons. Eventually, the highly excited HA enters the solid and the inner shell vacancies recombine by emission of fast Auger-electrons and/or photons.

For metals these processes could to wide extent be supported by experimental and theoretical investigations during the last two decades [15, 96, 102, 103]. Similar processes for semiconductor and insulator targets, however, are not as well understood. Fundamental investigations related to this topic can be found in e.g. [46]

An interesting fact is, that in contrast to commonly used ion lithographic techniques, a very slow ion does not cause collision cascade damage to the bulk. Therefore, a slow HCI, which still can deposit a large amount of energy at a sample surface could be an interesting tool for surface structuring with high resolution avoiding any damage to deeper layers [97]. This might allow, to use HCIs as unique tool for etching, ultra-thin-film growth and nano-structuring.

In order to get an idea of the involved length- and energy-scales, one can take a look at the classical-over-the-barrier (COB) model [102]. It predicts first quasi-resonant electronic transitions from the surface to the HCI to arise not before reaching a critical distance R_c

$$R_c \approx \frac{\sqrt{2q}}{W_\Phi} \tag{19}$$

These transitions fill highly exited projectile states with hydrogenic principal quantum numbers n_c

$$n_c \approx \frac{q^{\frac{3}{4}}}{W_\Phi^{1/2}} \tag{20}$$

where q denotes the projectile chare-state and W_Φ is the sample's work function. Both equations use atomic units. To give an example: for fully stripped Ar^{18+} ions on Al(111) ($W_\Phi = 0.16$ a.u.) the COB model predicts $R_c = 2$ nm and $n_c = 22$ [46].

The term "hollow atom" [39] illustrates nicely the extreme population inversion, which lasts up to several fs during the approach to the surface. Due to the high excitation of the projectile on its way towards the surface and beyond, soft X- as well as electrons due to auto-ionisation (AI) and Auger-type channels are emitted. In front of the surface, the emission of electrons dominates, whereas inside the bulk, significant emission of X-rays de-excites HA, which carry K-shell vacancies.

Formation and decay of hollow atoms can be studied through their ejected electrons and characteristic soft X-rays, as well as their trajectories, energy loss and final chare-state distribution of surface-scattered projectiles [96, 104-106].

Until finally ending within the bulk, along the whole projectile's trajectory from the time reaching R_c from eq. (19), a significant amount of the projectile's potential energy is transferred into a possibly very high number of emitted electrons (e.g. 150 for slow Xe^{40+} impact on a LiF surface [46]) and photons. The energy, transferred to particles or x-rays that cannot escape into vacuum, either because they are emitted inside the bulk and eventually inelastically scattered or emitted above the surface, but in a direction towards the bulk, is finally turned into an electronic excitation of the target within a small region around the impact site. This massive electronic excitation is confined in a very small volume at the surface and therefore leads to a very high energy density, which eventually can produce surface modifications [99].

In the case of CaF_2, e.g, it could be shown [107-109], that a HCI projectile of sufficiently high chare-state, slowly approaching the sample at low kinetic energies (150 q eV) can produce a single topographic feature on the surface upon the interaction with high efficiency, i.e. every ion produces exactly one defect. These defects are of a topographic nature, non-erasable nano-sized protrusions (hillock). This holds true above a certain threshold of potential energy (around 12 keV), above which height and diameter of the hillocks increase with increasing potential energy. By simulations on the basis of an extended classical over-the-barrier model the observed threshold could be successfully linked to a solid-liquid phase transition (nano-melting) [99, 107, 110].

It should be noted, that the production of these hillocks on the surface is purely related to the projectiles' potential energy. The kinetic energy, on the contrary, even has a slightly negative effect onto the hillock creation, due to the fact, that the potential energy is released along the track into the solid, and therefore, the energy density at the surface is lowered, as compared to a very slow particle.

On KBr(001) surfaces bombarded with slow highly charged Xe ions, on the other hand, pit structures with lateral sizes of 10 nm to 25 nm and monoatomic depth are created above certain thresholds for both potential and kinetic energy [111]. The mean pit volume shows a linear dependence on the potential energy of the ions. Potential sputtering [36] by a defect mediated desorption mechanism was invoked to explain these results.

I.3.2 Investigations on HOPG

Parts of the work described here have already been published [12, 13].

I.3.2.1 Historical review

Highly oriented pyrolytic graphite (HOPG) was one of the first materials, where the effect of (highly charged) ion bombardment could be investigated by scanning tunneling microscopy (STM). It is interesting, due to the simple preparation and reproduction of atomically flat standard surfaces by cleavage with adhesive tapes.

However, the nature of the produced defects by ion irradiation is still a matter of debate. It is particularly not clear, whether or not the produced defects are topographic protrusions, or just some kind of electronic defect.

Early studies of the defects produced by the impact of ions on HOPG were performed with singly charged Ar^+ ions at rather high implantation energies of 50 keV [112, 113]. The authors reported the occurrence of hillocks in the STM images with heights in the tenth of nanometer range and diameters in the nanometer range after the bombardment. The number of hillocks and the number of impinged ions was found to be equal and the observed structures were associated with a modification of the crystalline structure at the surface. The observed raising of the surface was attributed to interplanar stresses which are generated along the ion path. At that time, however, no corresponding AFM data were collected in order to obtain evidence of real topographic modification.

Further investigations [114] showed hillock formation to occur after irradiation with singly charged N, S, Ar and Xe ions in a kinetic energy range of 15 to 40 keV. At a fixed kinetic energy of 20 keV they found an increase of the hillock diameters when increasing the ion mass and linked this behaviour to the increasing nuclear stopping losses for heavier projectiles, while in this regime the electronic energy loss is nearly constant. Varying the kinetic energy of the Ar^+ projectiles between 10 keV and 30 keV, on the other hand, showed no significant influence on the hillock diameter. However, because the energy loss for these projectiles is dominated by nuclear stopping and almost constant, no final conclusion on the effect of the kinetic energy of the projectiles could be deduced from these experiments.

Later on, multiply charged Ar^{q+} ions (q=1,4,8) at rather low kinetic impact energies (<1 keV) were used as projectiles and subsequent STM investigations revealed, that the potential energy of the projectiles has a much larger impact onto the hillock size, than the projectiles' kinetic energy [115]. A strong increase of the defect size, in particular the defects' diameter, was observed as a function of chare-state at fixed kinetic energies.

Since STM images the electron density near the Fermi level, it is merely impossible to make definite conclusions on the topographic aspects of the features without corresponding AFM measurements. However, no protrusions were found in the contact mode AFM [115] and the combination of STM and AFM data led the authors to the assumption that the surface modification is due to the enhancement of partial charge density of state at the surface as a result of carbon atom sputtering.

Nevertheless, when considering the poor sensitivity of an ambient contact mode AFM to atom-sized structures as well as the low vertical resolution, the defects are practically not exceeding the expected noise level at these low charge-states.

Irradiation of samples with Ar^{q+} (q = 1, 8 and 9) ions at impact energies of 150 eV under normal incidence at the TU Wien [69, 116] and subsequent STM investigations without breaking the ultra-high-vacuum (UHV) conditions in between revealed an increase in lateral size and, to less extent, the features' height with increasing potential energy of the projectiles. Analysis of the tunneling current images via Fourier transformation and filtering showed a $(\sqrt{3}x\sqrt{3})\,R\,30°$ surface reconstruction in the vicinity of most of the defects [69]. Contact mode AFM imaging in UHV did not yield any evidence of topographic changes due to the ion bombardment.

There are two types of defects caused by low energy ion bombardment in HOPG [117]: Vacancy (VD) and interstitial defects (ID), e.g., caused by trapping of the projectile (or some recoiling carbon atom) beneath the first graphene layer, both resulting in an enhancement of the local charge density of states and hence seen as protrusions in the STM image. As the observed surface reconstruction is characteristic for ID creation, the researchers concluded that the hillocks appear due to IDs or VDs created along with IDs. The strong increase of defect diameter for higher chare-states was interpreted as a pre-equilibrium effect of the stopping of slow HCIs in HOPG [116]. The conversion of the MCI to hollow atoms is linked to a reduced screening upon final excitation within the solid, which could result in a strongly increased energy loss of the projectiles. This effect, in turn, would lead to the creation of IDs located closer to the surface and more VDs due to a higher momentum transfer to the first carbon plane.

Subsequent treatment of an impact site of Ar^{8+} with electron ejection from a STM tip or laser irradiation leads to a localised transition, a sp2 to sp3 hybridisation [118]. The same is reported for annealed samples in a hydrogen atmosphere at 650°C [119].

Further experiments [120] again yielded a clear increase in diameter with rising charge-state. A variation of the kinetic energy at a fixed chare-state of q = 23 over more than two orders of magnitude (1 keV to 300 keV) showed no significant influence of the kinetic energy on the size of the nanometer-sized features.

After, as mentioned, a number of results giving the impression of producing no topographic modifications to the surface, but rather electronic defects, such

topographic features were eventually found [121] after irradiation with Xe^{46+} at kinetic energies of 138 keV and careful studies using STM in combination with an AFM using the same tip under UHV conditions.

It should be noted that both the chare-state and kinetic energy used in this study were considerably higher than in previous experiments, which attempted to image structures with AFM. The strong repulsive forces in contact mode AFM, used in the previous studies, might damage the features created by the HCI. Moreover, several groups reported that no true atomic resolution (i.e., imaging of individual atoms) was achieved in contact mode, although they were able to image the periodic structure of the surface. Eventually, even after irradiation with Ar^+ ions (0.5–1 keV) hillocks could be found with an AFM operated in the intermittent contact mode [122]. The heights of the structures found in the AFM images (0.08–0.15 nm) were, however, much smaller than in corresponding STM images (0.2–0.8 nm).

I.3.2.2 Experimental Technique

Irradiations of the HOPG samples were carried out at the ARIBE [94] facility of GANIL (Grand Accélérateur National des Ions Lourds) in Caen, France. Xe^{q+} (q = 13, 15, 20, 23, 26, 27 and 30) and Ar^{q+} (q = 9, 12, 14 and 16) ions were extracted from a 14.5 GHz ECRIS and accelerated onto the samples under normal incidence to final impact energies of 150 keV to 360 keV. For every desired chare-state two freshly cleaved HOPG samples were fixed on a target holder and mounted in the target chamber at pressures of 10^{-7} mbar. Time averaged beam fluxes of 10^9–10^{10} ions/s and irradiation times of 20 s up to 10 min resulted in total ion fluences of up to several 10^{11} ions/cm^2 at the target surfaces. For each chare-state, two samples were irradiated with rather different fluences (typ. a factor of five). By counting the number of defects per unit area and comparing with the respective fluence, the defects could be clearly ascribed to (single) ion bombardment. Samples were investigated immediately after irradiation with a Nanoscope III (Digital Instruments) AFM in constant force contact mode. After returning to TU Wien the samples were further analysed with a MFP-3D AFM (Asylum Research). Both instruments were operated under ambient conditions with triangular SiN cantilevers (Veeco) with a nominal force constant of 0.1 N/m and a typical tip radius of curvature of 10 nm. STM images of selected samples were taken at constant current mode with a typical tunnelling current of approximately 0.3 nA and a positive sample bias voltage of 0.7 V in a AFM/STM combination (Omicron) under UHV conditions (pressure typically below 10^{-9} mbar) with commercial Pt/Ir tips (Veeco).

I.3.2.3 Results

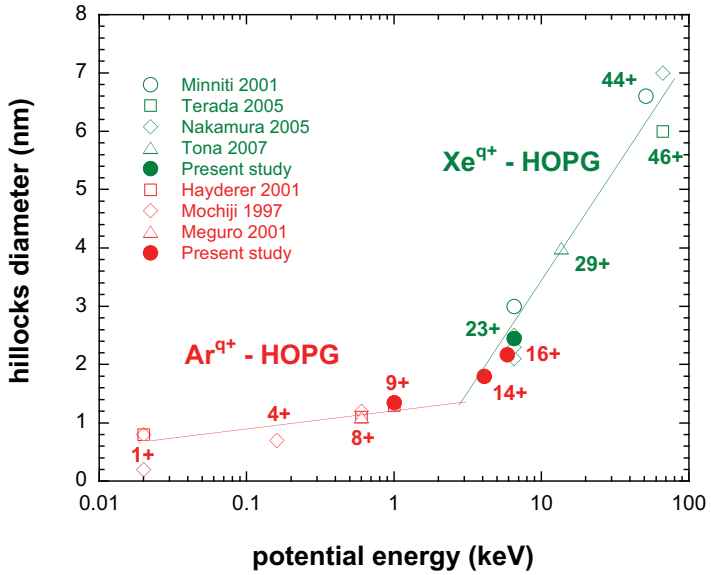

Figure I-22: Feature diameter observed in STM on irradiated HOPG
The observed diameter for the features produced by irradiation with HCI as a function of the projectiles' potential energy. Image taken from [13]. Data from [115, 116, 118, 120, 121, 123, 124].

After irradiation with Xe^{23+} ($E_{kin} = 150\,\mathrm{keV}$) ions, typical hillocks were found on HOPG by STM studies. The number of defects per unit area as measured by STM was found to be in good agreement with the applied ion fluence. For three chare-states (Ar^{9+}, Ar^{14+} and Xe^{23+}) a statistical evaluation of the diameters of the found hillocks was performed. Our results are compared with all available data from previous STM studies [115, 116, 118, 120, 121, 123, 124] in figure I-22. Although the kinetic energies of the ions used in these studies were considerably different (0.15–300 keV), all results are presented in a single plot as a function of potential energy only, taking into account that the influence of kinetic energy on the hillock diameter was found to be practically negligible [120]. Quite astonishingly all results seem to follow a single curve and our new results perfectly fit to it. Interestingly, a stronger increase of the hillock size with increasing potential energy is observed above 2 keV to 3 keV of potential energy. This might indicate a second mechanism for nano-structure formation in HOPG, which only comes into play above a certain minimum potential energy. As in the case of CaF_2 [107] a possible candidate could again be a solid–liquid phase transition (nano-melting). Preliminary calculations on the basis of the inelastic thermal spike model modified for layered materials like HOPG [125] and performed by Marcel Toulemonde strongly support that a transition to a liquid phase is possible with a potential energy between 2 and 3 keV.

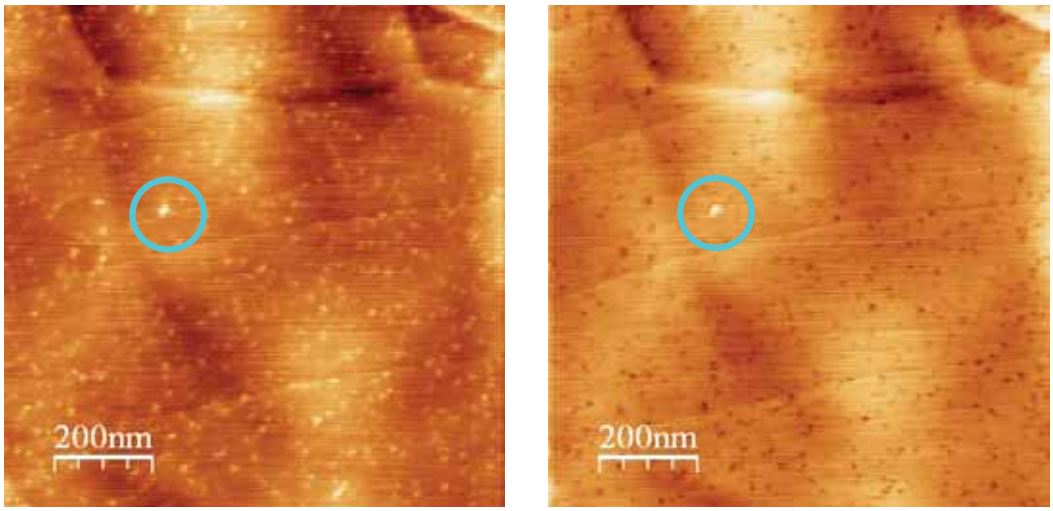

Figure I-23: HCI irradiation induced defects on HOPG.
The images are measured in contact mode AFM and show the trace (left) and re-trace (right) height images under 0° scan angle (tip movement parallel to the cantilever). When comparing trace and re-trace, one can see that except one topographic feature (indicated by the green circle), the contrast for the observed features reverses (see text).

HCI-induced nano-structures were also visible in ambient contact mode AFM for all investigated chare-states. The scanning process, however, revealed great differences compared to the stable, topographic hillocks as seen e.g., on CaF_2 [107-109]. Contrast formation in the respective scanning directions was found to be heavily dependent on changes of the scan angle: Features in the AFM topography images appear as protrusions in the forward scan and as pits in the back scan (figure I-23) when scanning alongside the cantilever axis (0° scan angle). Lateral force images which were recorded scanning perpendicular to the cantilever axis (90° scan angle) reveal the same structures with a reversed image contrast in the forward scan and the backward scan, respectively, a behaviour which is expected for the presence of friction forces. Similar results have been obtained in a study on high-energy (MeV) irradiation of HOPG with Au^+ ions [126] and in studies on mica irradiated with both slow HCI [127] and swift heavy ions [128]. It is long known that lateral forces, which are mostly caused by friction, can give rise to topographic artefacts. This effect is especially pronounced if light beam deflection is used to sense the motion of the cantilever (as in these studies) and is a consequence of measuring the bending angle of the cantilever rather than the deflection itself [129]. In the constant force mode, the loading force then not only arises from perpendicular forces but also has a contribution from the lateral forces. Hence, variations of the lateral force may cause the feedback loop to respond and the resulting apparent changes in height add to the true topography and depend heavily on the scan angle. These apparent height changes are not necessarily small as compared to the height of typical topographic features and can even be the dominant (pseudo)topographic contribution on very flat surfaces.

The mean defect diameters as measured by contact AFM remain nearly constant for the investigated chare-states and the obtained values are considerably larger (10 nm) than in our STM studies (typically below 5 nm in the

investigated potential energy regime). Hence, we conclude that the AFM tip dimension determines the observed feature size.

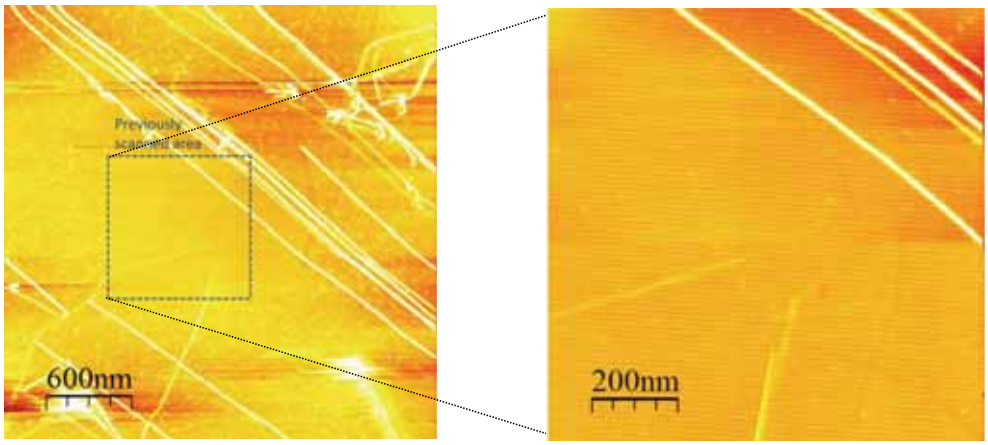

Figure I-24: Feature weakening due to the interaction with the AFM tip on HCI irradiated HOPG
The shown lateral force images were measured via contact mode AFM under a scan-angle of 90° and constant loading force, showing features from the preceding irradiation with about 1000 μm^{-2} Xe^{30+} ions of 360 keV kinetic energy. The left image shows a zoom out of the initial scan area (right), where one can clearly see the removal of the visible features in the previously scanned area. For details see text.

Similarly to the case of mica reported in [127] we have found that the structures in the lateral force images are susceptible to modification by the AFM tip as continuous scanning first leads to a weakening of the features and ultimately to their complete erasure as illustrated in figure I-24. This might be related to the fact, that the observed features are just attributed to e.g. water droplets, pinned to the defect sites. Further investigations are needed to gain better insight on the nature of the HCI induced defects on HOPG.

Similar studies have also been performed on muscovite mica [12], but are not included in this work.

I.3.2.4 Conclusions and outlook

We have studied the effects of slow HCI bombardment on HOPG surfaces by STM and AFM. Our STM results are in good agreement with the literature and support the idea that the potential energy rather than the kinetic energy of the incident ions is the dominant driving force in nano-structure creation. From our AFM studies it has to be concluded, that the resulting nano-features although visible in AFM do not represent real topographic modifications of the HOPG surface but rather regions of enhanced friction, which give rise to pseudo topographic features (protrusions turn into pits upon reversal of the scanning direction) in AFM topography images. This effect, however, could be unambiguously identified as a result of the ion bombardment by comparing the number of defects per unit area on samples bombarded with ions of the same chare-state but with different fluences. More systematic studies are planned and necessary to quantify the involved friction forces and to determine whether these

forces only superimpose a true topographic surface modification or if such a modification does not take place in the investigated potential energy regime.

I.3.3 Investigations on PMMA

In this work, just a rough idea of the investigations is shown; a detailed description about the experiment can be found in [130]. As discussed in part II of this work, one of the driving forces behind investigations of the capillary guiding effect are related to possible applications in HCI nano-lithography.

Similarly to the previously described work concerning the irradiation of HOPG, another material was investigated: Polymethyl-methacrylate (PMMA), better known as acrylic glass. It is a transparent, thermoplastic polymer, which is widely used in a variety of applications. Besides many others, especially the usage as a photoresist in the semiconductor industry for electron beam or photo-lithography of Si wavers should be mentioned. In such a process, a thin film of PMMA is deposited onto a surface. A mask is used to select areas being irradiated with an appropriate fluence. The irradiation causes chain scissions, which lower the resistivity against chemical etching. After irradiation, a liquid etchant is used to remove the damaged parts, thus, leaving a shadow image of the mask on the substrate.

First investigations of defects produced by the impact of slow HCI on PMMA have been done in the nineties [131], showing depressions to occur after etching in a liquid solvent (isopropanol). Without using such an etchant, no defects could be resolved at that time.

Only recently, swift heavy ions were used as projectiles and a systematic study of the occurring surface modification was performed [132]. Similarly to the earlier investigations with slow HCI [131], depressions in the PMMA film were found. Their diameter exhibited a distinct dependence on the projectiles' initial charge-state. For charge-states above about 45, even a protruding rim surrounding the depression was found, leading to a crater-like shape.

We irradiated films of PMMA, with a thickness of 40-60 nm, on a Si substrate with slow, highly charged xenon ions over a broad range of charge-states and investigated the sample surfaces after irradiation by contact mode, as well as intermittent contact mode AFM. We used samples of the same composition as used in [132] for the first investigations. Later on, also samples manufactured by IMS [133] have been used.

The irradiations were performed at the ARIBE facility [94] for charge-states $q < 31$, at the Rossendorf EBIT [134] for $20 < q < 40$, as well as at the Heidelberg EBIT [90] for the highest charge-states $q < 51$. The samples were investigated under ambient conditions in contact mode AFM (MFP-3D AFM, Asylum Research).

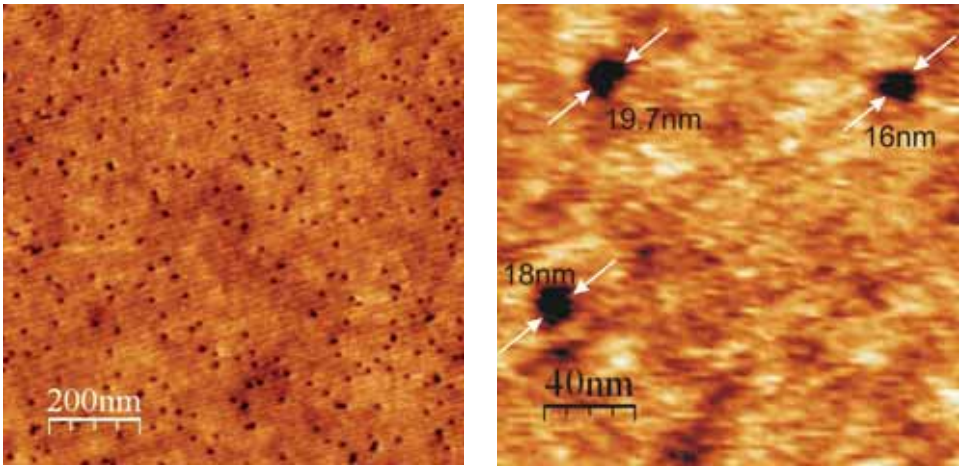

Figure I-25: Single ion impact defects on PMMA
The images show the topography from contact mode AFM measurements under ambient conditions. The PMMA samples have been irradiated prior by slow Xe^{47+} (left) and Xe^{48+} (right) particles. The typical defect sizes are shown (right).

In contrast to the earlier experiments [131], we found holes in the irradiated samples (figure I-25), even without applying any chemical etchant in our AFM studies. As an example shows (figure I-25, right), the defects are nearly circular holes.

Systematic investigations are still a work in progress, but first results nicely show a dependence of the defects' size on the projectiles' potential energy and also revealed a relation to the ions' velocity, which determines how deep the holes reach.

Driven by these findings, we tried to investigate charge-state dependencies in high fluence irradiation through a mask and subsequent etching [135]. Although it could be seen, that the irradiation-induced damage does depend on the projectiles' charge-state, there are more detailed investigations needed, in order to provide a more systematic picture.

These, in conjunction with further results of HCI-irradiated PMMA are going to be reported in the upcoming PhD thesis of Robert Ritter.

Part II: Capillary Guiding

II.1 What is Capillary Guiding?

In the year 2002, the capillary guiding effect through insulating nano-capillaries was first mentioned in the literature by Stolterfoht, *et al.* [136]. The experimental finding at that time was, that a charged particle beam in the keV kinetic energy regime interacted with a sample of etched tracks through a PET foil in a way, that the projectiles were somehow transmitted under angles of incidence much larger than the possible geometric transmission angle. The sample consisted of an electrically insulating PET foil, in which randomly distributed tracks of swift heavy ions (1 GeV xenon) were created by irradiation in an accelerator. The tracks were chemically etched to capillaries of about 100 nm diameter. The length, i.e. the foil thickness, was about 10 µm, thus, the aspect ratio of the single capillaries was about 100. In order to avoid charging at the front, the foil was coated under 45° with a thin layer of gold at the front as well as at the back side, before doing the experiments [136].

Interestingly, after some irradiation time, projectile ions were transmitted through the tilted capillaries under angles of several degrees, much larger than the geometric opening. Astonishingly, the transmitted ions even kept their charge-state upon transmission [136], which is especially surprising due to the fact, that usually, highly charged ions that come closer than a critical distance $R_c \approx \sqrt{8q+2}/(2W)$ [102], where q denotes the charge-state and W the work-function of the surface, undergo a neutralisation sequence, eventually leading to the projectiles' total neutralisation. Therefore, the transmitted particles have been reflected in a distance $d > R_c$ in front of the surface due to an electric field, caused by a charge density, deposited by the preceding ions that hit the wall.

One should mention, that earlier experiments by a Japanese group [137, 138] have used similar capillaries to investigate exactly the interaction of highly charged ions (HCI) with a surface and to produce hollow atoms [39] behind the sample. They avoided any effects from charge deposition by introducing an electron shower, which caused neutralisation of possible remaining charges at the wall.

In the case discussed first, no electron shower was used, thus projectiles hitting the inner surface of the capillaries caused the deposition of a number of charges from the neutralisation process in front of the surface [102], eventually causing the charging.

This was the starting point for detailed investigations of the underlying physics for various materials, projectiles, and geometries, also including electrons as projectiles and metallic as well as insulting capillaries (see e.g. [139] for a short review).

II.1.1 The basics

A first interpretation of the guiding effect has been given in the original work, where the experimental findings have been published [136]. According to the authors, self-organised charging effects cause the projectiles to be guided through the capillaries without getting into close contact with the walls. Their

experiment used a goniometer holding the PET foil containing the tracks (100 nm diameter, 10 µm foil thickness, 4% area coverage). Behind the sample, an electrostatic analyser was used to investigate the distribution of charge-states after the transmission.

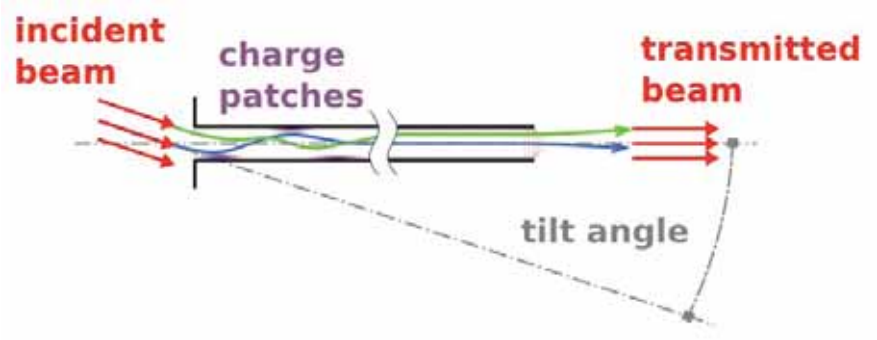

Figure II-1: Illustration of the guiding effect
The projectile beam impinges on the entrance region of a capillary. The entering projectile ions hit the wall close to the entrance and cause the formation of a charge patch, which deflects the succeeding projectile ions.

The simple picture of what is going on inside such a capillary is the creation of a first charge-patch from the ion impacts close to the entrance (figure II-1), due to the fact, that ions in close contact to the wall are neutralized by electrons captured from a small vicinity at the surface [102]. Following projectiles are deflected by the evolving electric field from the growing patch and hit the surface at another location or are eventually transmitted through the whole capillary. Of course, there might be a number of charge-patches along the sample involved, each of them contributing to the total guiding field.

These charge-patches reach some quasi-equilibrium, where the impinging projectiles refill the charges lost by conduction. During the formation process of the patches, the transmission is time-dependent, whereas it reaches a stable regime as soon as the charge-distribution at the inner wall becomes a dynamic equilibrium between conduction losses and impinging projectiles. The whole process can be thought as being self-organized in a way that the patches tend to form in such a way, that ions are eventually transmitted. The effective charge each ion deposits is in a first approximation equal to the projectile's charge qe, with its charge-state q [140]. It was found experimentally, that during charging, the time-evolution of the transmission could be described quite well by a simple $1 - e^{-\frac{t}{\tau_1}}$ law ($\tau_1 \approx 2.5$ minutes), whereas during discharging the transmission descended via a $e^{-\frac{t}{\tau_2}}$ law with a much larger time constant of $\tau_2 \approx 40$ minutes [136].

In order to understand this behaviour, a simple model of charge balance can be applied [136, 140, 141], where the transmission is thought to be proportional to the total charge on the capillary's inner surface, thus $J_{trans} \propto q_s(t) = \int \rho(\vec{r}, t) d^3r$. The proposed models differ, so only a rough idea of the mechanism shall be given here, whereas the reader can find more detailed insight into the models in the literature [136, 140-143]. The electrostatic potential inside the capillary reaches values of just a few volts, which should be enough to guide the keV projectiles under incidence angles of a few degrees [144].

When denoting the beam current J_{in} and the discharge current absorbed by the surface J_d, the balance reads

$$\dot{q}_s(t) = J_{in} - J_{trans} - J_d = J_{in} - J_{tr} - \frac{1}{\tau_{eff}} q_s(t) \tag{21}$$

where τ_{eff} denotes an effective charging time.

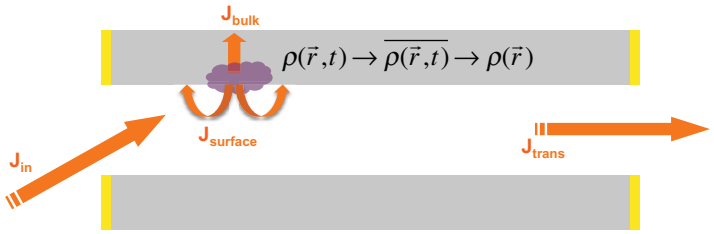

Figure II-2: Simple model for capillary guiding
A cut through the capillary (gray) with a conductive cover at the front and the backside. The incident ion beam current J_{in} from the left hits the capillary wall, causing charging. Conduction allows an electrical current J_{bulk} into the bulk and $J_{surface}$ along the surface. The transmitted ions contribute as J_{trans} to the balance.

The solution corresponds well to the behaviour of the transmission's time evolution during the charging period [140]

$$q_s(t) = q_s(t \to \infty)\left(1 - e^{-\frac{t}{teff}}\right). \tag{22}$$

The charging time is related to the bulk and surface transport times via

$$\tau_{eff} = \left(\frac{1}{\tau_s} + \frac{1}{\tau_b}\right)^{-1}, \tag{23}$$

because the adsorption into the wall can be split into two components, one due to surface diffusion $J_{surface}$, and J_{bulk} by bulk conductivity of the material (figure II-2).

When switching off the beam at $t = t_0$, the time evolution of the transmission also has to take the bulk charge $q_b(t)$ into account, since according to [140], the total charge determines the transmission, thus

$$q(t) = q_b(t) + q_s(t) = Q_0\left[ce^{-\frac{t}{\tau_b}} + (1-c)e^{-\frac{t}{\tau_{eff}}}\right] \tag{24}$$

where $c = c(q_s, \tau_s, \tau_b) < 1$. In the discussed case, where $\tau_s \ll \tau_b$, the transmission, therefore, drops fast (τ_{eff}) in the beginning and eventually becomes a slowly decaying function (τ_b). In fact, the measured time dependent transmissions during the discharge time can be well described by the above law in eq. (24), whereas it turns out, that often the charging does not exactly follow eq. (22), but shows an additional onset delay instead, before almost no transmission is observed. This onset time cannot be understood by means of the simple rate equations [140] but stems from the necessary initial charge deposition, before which the guiding effect cannot set in. It has to be noted, that in contrast to the description shown here, in the case of the glass capillary, which is presented in the experimental part

later in this work, the surface transport is not large as compared to the bulk conductivity.

A simulation of the whole process on the nano-meter scale [140], based on classical-trajectory monte-carlo and a mean-field classical transport theory approach, showed similar behaviour as the experimental findings [136, 144]. Unfortunately, this simulation is only applicable to nano-capillaries, since a simple scaling up to macroscopic length scales exceeds computational possibilities.

The linear nature of the proposed model, assuming proportionality of the discharge-current J_d and the applied charge Q is under discussion, because some experimental findings seem to disagree (see e.g. [145]).

II.1.2 Nano-capillaries and what we could learn from them

In this short section, a brief historical review shall be given, in order to show the developments and the state of the art when starting the experiments described in this work were started.

Before the discovery of the guiding effect, investigations with conductive capillaries were preformed, showing their potential usage as "freely" decaying hollow atom source [137, 146-148]. Following the first investigations of the phenomenon discussed in the last section [136, 140, 144, 145, 149], a number of further experiments were conducted to study the guiding effect in more detail. Theoretical simulations continued and provided an insight into the charge distributions and their time-evolution inside the capillary [140, 141, 150]. Usually all these experiments made use of multiply or highly charged ions.

Soon after the first description of the guiding effect through insulating nano-capillaries, a first characterisation evolved by using the so-called "guiding power" [151], i.e. basically a measure for the width of a Gaussian fit through the measured transmission as a function of tilt angle ϕ. According to the authors, the transmission functions $T(\phi)$ can be described by a Gaussian of the form

$$T(\phi) = T(0).\, e^{-\frac{\sin^2 \phi}{\sin^2 \phi_c}} \tag{25}$$

where ϕ_c denotes the capillary's guiding power. We use this terminus as equivalent to the width of the transmission function when presenting the results later in this work.

Of course, one expects material properties to highly influence the whole effect, especially the role of electrical conductivity obviously is crucial. By using completely different attempts in fabrication, regular arrays of very well aligned capillaries could be produced in SiO_2 [152], which were later used to investigate their guiding properties as well [153] besides other developments , like nanoscale apertures in silicon nitride membranes [154] or in Al_2O_3 [155, 156]. PET foils, however, have better guiding properties, at least larger guiding angles, indicating also the high influence, the material has onto the strength of the effect.

Systematic studies revealed the scaling of the width of the transmitted profile as well as of the guiding power when varying the charge-state or the energy of the projectiles [157-159]. It turned out that both change in the same way, i.e. the ratio between them is a constant. Furthermore, the major parameter for the scaling is the projectile energy per charge E_{kin}/q, which determines $1/\sin^2 \phi_c$ in a slightly non-linear way.

A massively debated question is, whether the whole conduction process at the insulator surface is linearly depending on the effective charge densities and potential differences, respectively, or not. Interestingly, the transmission $T(\phi)$ through the capillaries varies just slightly when changing the incident current by orders of magnitude [151]. Therefore, the authors claim a strong dependence of the transport on the deposited charge density. The experimental findings do, on the other hand, not fit to a linear model, where the discharge-current J_d is proportional to the deposited charge. Eventually, the authors link the non-linear transport to the Poole-Frenkel effect [160].

Since the inside of a capillary is not easily accessible by an experimentalist, only simulations could make the charge-patches inside visible. By careful analysis of the spot movements after transmission through a tilted capillary array, it was later possible to make the creation of charge-patches indirectly visible and investigate the creation process in more detail [161-165]. By this, one could also investigate the effect of remaining charge-patches onto following charge-cycles. It is obvious, that one crucial point in all investigations is the total discharge of the capillaries before a measurement. A closer look showed [161], that remaining charge-patches cause completely different charging dynamics and result therefore in poorer comparability.

An important observation showed [166], that in specific cases, photon emission can lead to significant signals on the MCP detector, thus one has to carefully consider them as a background.

II.1.3 From nano- to micro-capillaries

Besides possible applications in micro-ion-lithography, also fundamental interest makes the use of single capillaries interesting, because possible density effects [167, 168] cannot occur. These effects are not yet fully explained.

Within the regime of nano-capillaries, investigations concerning the influence of the capillaries'diameter onto their guiding ability [169] showed, that the guiding power does not change significantly when increasing the capillary diameter from 100 nm to 400 nm. Also the total charge inside one single capillary necessary for establishing static transmission seems independent of the diameter. Of course, one interesting question arising is, whether this holds up to macroscopic length-scales of the sample.

One interesting innovation after a row of experiments with PET foils [170-174] was the utilisation of a single large tapered glass capillary to focus an ion beam [175]. There, the authors found the guiding effect to work also on a macroscopic length-scale; their 5 cm long capillary narrowed from an inlet diameter of about 0.8 mm to an outlet diameter of approximately 24 µm. They found a focusing effect, i.e. a beam density enhancement in comparison to the freely travelling beam, which could also be explained qualitatively by the guiding effect. For fast (MeV) projectiles, a focusing effect in a tapered glass capillary has been found [176], too, but this is attributed to scattering rather than the guiding effect discussed here.

Guiding and focusing of ion beams of higher charge-states (230 keV Xe^{23+}) has also been observed with such tapered capillaries [177] with currents between a few and 50 pA of ion current. In contrast to that, there, so-called blocking has been found [178], i.e. loss of transmission, which is attributed to a reflection inside the capillary due to a charge-density exceeding a certain critical value.

So, automatically, the question rises, whether or not the guiding effect, i.e. stable transmission under tilt angles of several degrees was also valid for macroscopic tubes. In this work, we have therefore investigated macroscopic straight capillaries (see II.2). A straight sample has a higher symmetry and is therefore beneficial for a theoretical understanding. The transmission function $T(\phi)$ can, in the case of the tapered capillaries, be quite remarkable, since it was found, that under certain circumstances the transmission in the straight direction, i.e. $\phi = 0$, is negligible, thus $T(\phi)$ cannot be described by a simple Gaussian, but a more sophisticated function with a distinct drop towards $\phi = 0$ [179].

As already mentioned, available simulations are only applicable for nano-capillaries yet.

II.1.4 Other related observations

In the literature, one also finds recent investigations of obviously related phenomena but using different geometries than the cylindrical symmetric capillaries. An astonishing effect is the so-called double ion guiding of ions between a set of two parallel glass plates [142, 143, 180], where, according to the author, a high non-linear behaviour of the insulating glass gives rise to the formation of a conductive channel on each of the two glass plates, surrounded to the left as well as to the right with a finite charge density. This eventually causes a guiding electric field, similar to the case of a glass capillary. The effect is now, that as a consequence of turning the glass plates around an axis perpendicular to them, the ion beam is also deflected, as if it was trapped. The underlying phenomenon is explained by a transition from an insulator into a conductor, as a consequence of a too high charge density.

In contrast to the ion guiding through insulating capillaries, also electrons are subject to a deflection when using similar interaction geometries. In a first attempt [181], very similar behaviour was observed, but it is still not completely clear, whether this can be attributed to guiding or maybe scattering rather than that. There, primary electrons of about 200-350 eV kinetic energy were transmitted through a regular array of Al_2O_3 capillaries under tilt angles of several degrees. The transmission at tilt angles larger than the geometric opening can be a result of charging, as in the case of slow ions, or of scattering at the surface.

In another investigation it was found [182, 183], that the electrons undergo massive energy losses during such interactions with tilted nano-capillaries, which can be understood by multiple inelastic scattering events at the surface. According to simulations, the electron transmission can be understood by quantum reflection at the surface (step in the potential) as well as inelastic scattering [184]. When taking a look at the interaction of electrons with such capillaries, one even has to consider secondary electrons, which were also found to be present behind the sample [185]. It is still not clear, to which extent guiding as in the case of ions plays a role for electrons, as there also seem to be some time dependent phenomena [186], which cannot be attributed to simple surface modification effects.

Recently, other geometries than circular capillaries became available. The creation of rhombic channels in mica-foils [187] lead to the possibility of investigating the charge patch geometry in such a case. There, the transmitted

beam profile showed interesting features, that are not fully understood yet. The image on a PSD behind the sample was not a direct image of the geometry, but showed a different pattern. However, the image had the same symmetry. The formation of these non rotation-symmetric images might give a closer insight into the charge-distribution along the capillary axis.

Fundamental investigations of the transport mechanisms in insulting materials, as discussed here, are studied by an experiment, using a single insulator surface, which is irradiated and probed at the same time by one single primary beam [24]. There, one can measure the beam deflection for various materials, beam intensities and species. Investigations of insulators' charging and discharging behaviour are still a matter of investigation.

Beside positive ions and electrons, more exotic projectiles, as 18 keV O^- ions were used as well to investigate the interaction with Al_2O_3 capillaries [188, 189]. There, even under smaller angles, charge exchange leads to significant amounts of atomic O^0 in the transmitted signal. Guiding plays practically no role in this regime.

II.2 About the Experiment

The aim of the described experiment was in a first attempt to show, whether or not the guiding mechanisms are still working in a macroscopic world, where the related dimensions are mm and cm rather than nm and µm. Of course, experimental findings for large tapered capillaries had already existed before [175], but those seemed to show quite distinct behaviour different from the case of nano-capillaries. Therefore, in a first step, we took a quick look onto the guiding properties of a macroscopic straight glass tube.

In order to investigate the capillary guiding effect one of course needs a projectile beam of proper intensity, energy and charge-state and on the other hand a mechanical manipulation system, capable of aligning and tilting the capillary with respect to the beam axis. In addition, a suitable particle detector is needed inside this UHV chamber.

The used capillaries are roughly one centimetre long and have an inner diameter of the order of 100 µm, thus an aspect ratio of about 100. They were made of borosilicate glass and are prepared by pulling a hot glass tube. The final capillary was cut by a diamond saw.

Details about the experiment are discussed in the following sections.

II.2.1 Providing the projectiles

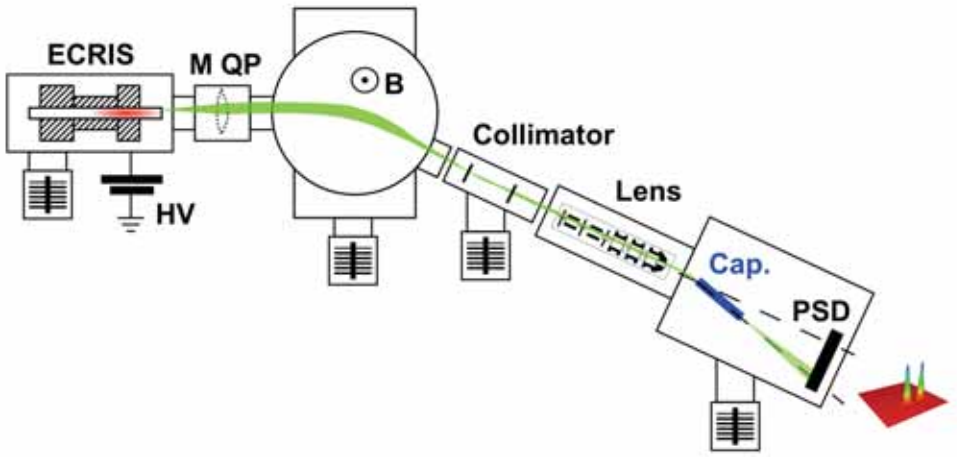

Figure II-3: Beamline overview
Starting from left to right, the ions are created in an ECRIS and extracted electrostatically. Afterwards, the ions are focused in a magnetic quadropule field (M QP) and mass-charge-separated (B) at the beamline entrance. A second aperture (Collimator) collimates the beam, which can be focused in an einzel-lens (Lens) onto the sample (Cap.). Behind the sample holder, which can tilt the capillary against the beam axis, as PSD is used to monitor the transmitted ions. [1, 6]

A schematic view of the whole experiment is given in figure II-3. The ions are provided by an 14.5 GHz all-permanent-magnet-ECRIS, which is described in detail elsewhere [41]. This source basically produces a magnetically minimum B confined plasma, which is heated by 14.5 GHz microwaves, corresponding to the electron cyclotron resonance inside the magnetic field. The radial field is hexapole-shaped and established by permanent magnets. Due to the heating of the electronic subsystem inside the plasma the atoms can be ionised up to charge-states as high as about 13. These ions are extracted by means of an electrostatic field at an extraction electrode. Afterwards the particle beam is manipulated by a set of magnetic quadrupole lenses before entering a magnetic sector field used for mass-charge-separation.
All the presented measurements were performed using argon ions of 4.5 keV kinetic energy. If not stated differently the used ion species was Ar^{9+}. In some cases also Ar^{7+} was used.
The ions enter the beamline through an aperture. For the first investigations the beam was then transferred via a set of electrostatic deflectors and lenses to the experiment's chamber, whereas in a later step, after having shown the principle existence of the guiding effect in our size-regime, we introduced a collimator, in order to be able to specify the phase-space-volume occupied by the particle beam. It consists of a set of two apertures of the same diameter, separated by a distance of 230 mm. Both, the entrance as well as the exit aperture of this collimation track are mounted on a sliding carriage, housing a whole set of different apertures. Therefore on can choose different combinations of apertures for the collimation.

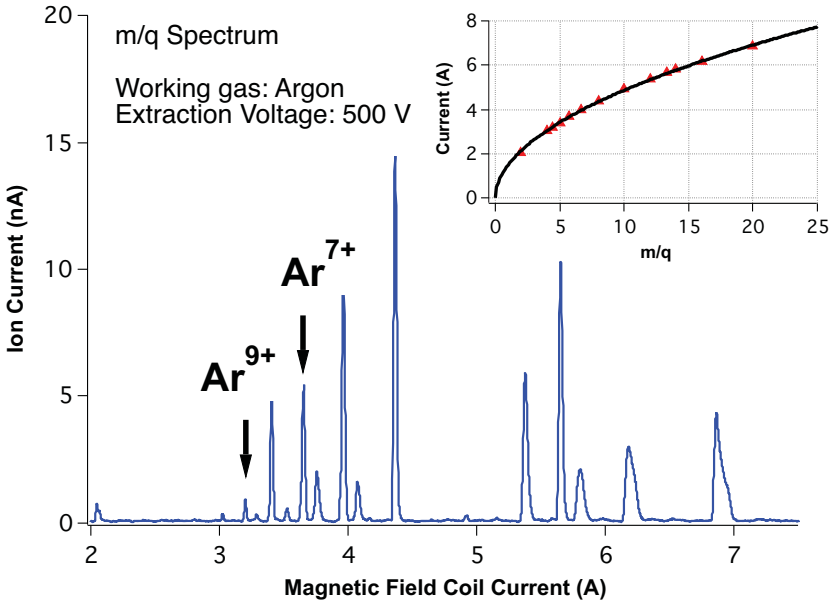

Figure II-4: Example mass-charge-spectrum
Taken at the second aperture when varying the current through the sector magnet, thus the magnetic field strength. The peak identification is shown in the upper right corner obeying a square-root-law.

It turned out that the stability of the beam from the source is a major issue for all capillary experiments presented due to the high requirements regarding 'beam quality', i.e. diameter and opening angle. Optimizing empirically the phase-space-density for the chosen 4.5 keV Ar^{9+} beam lead to the usage of a set of two 1 mm apertures, which are, as already mentioned, separated by 230 mm. Therefore the maximum opening angle of the beam can be estimated to be approximately ±0.5°. Usually the resulting projectile beam was not focused further before entering the capillary chamber. The estimated maximum diameter of the beam when hitting the capillary entrance was therefore about 3 mm. In some cases, a set of lenses behind the collimator was used to focus the projectile beam onto the capillary entrance.

In order to identify the ion species, the current at the collimator's second aperture provides suitable resolved spectra (figure II-4). Typical ion currents were of the order of 1 pA. The transmitted beam flux after collimation usually was of the order of 5 10^4 ions/s mm^2.

The collimated beam travels a distance of about 0.5 m until it reaches the experiment's chamber. In this drift region, an electrostatic einzel-lens could be used for focusing the beam onto the capillary entrance, but was usually not operated, in order to preserve the specified opening angle. Several sets of deflection-plates, however, were used to guide the beam centred into the interaction chamber.

II.2.2 The interaction chamber

After entering the chamber through the last (grounded) lens element, a set of deflection plates directly in front of the capillary entrance could be used to

influence the incident beam direction. For most of the presented measurements, however, these plates where grounded, thus the beam was not influenced.

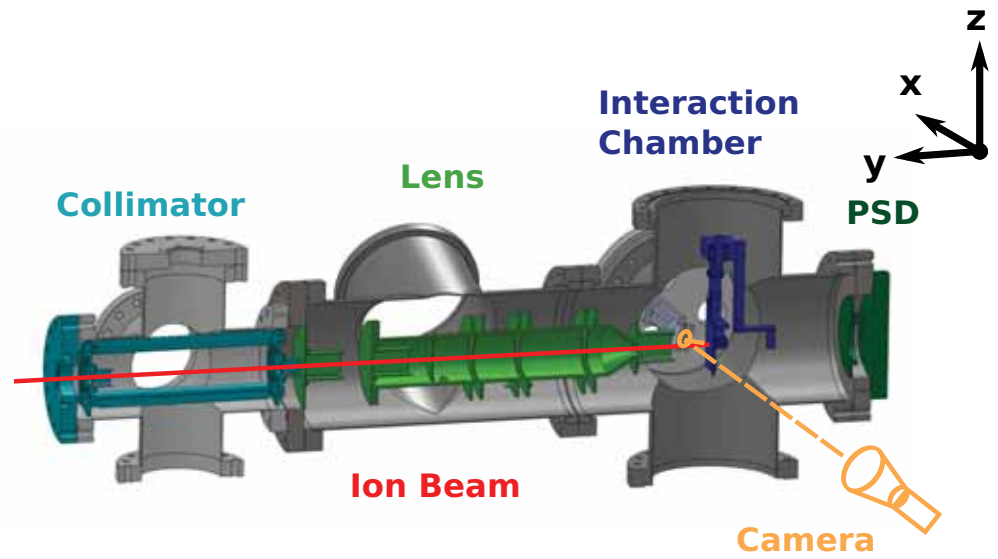

Figure II-5: Cut through the beamline
The beam (red) enters through the lens system (green) and hits the sample holder (blue). A mirror (yellow) is installed in front of the capillary, in order to have a direct line of sight into a video camera. High magnifying optics are used to monitor the entrance position.

The beam eventually hits the sample holder, which is mounted on a mechanical manipulator, allowing movement in all three directions as well as tilting around the vertical axis. The motion is stepper motor driven with a theoretical resolution of 0.012 mm and 0.02°, respectively. However, due to a rather long mounting rod, the actual reproducible position resolution was worse. Therefore, a camera was used to directly look at the aperture position via a highly magnifying optical lens system. In order to have a rather straight look onto the aperture, a mirror was installed as close to the beam axis as possible, facing the sample holder. Mounted at the backside flange, a position sensitive detector (PSD) is installed to record impinging particles. It uses a set of micro-channel-plates (MCP) in chevron configuration in front of a wedge-and-strip-anode (RoentDek [190]).

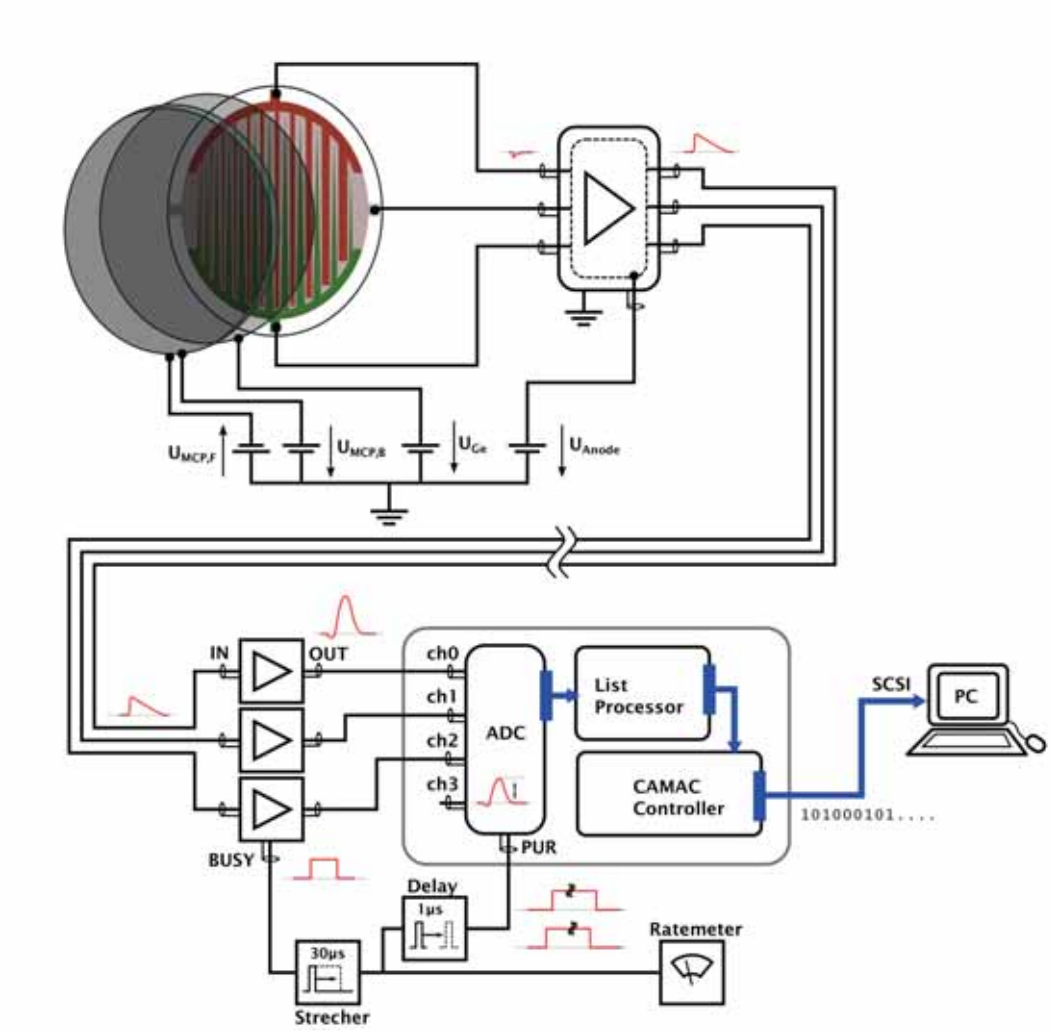

Figure II-6: Schematic view of the position sensitive detector wiring and the data acquisition system.
The illustration combines electronic wiring as well a schematic picture of the pulse shapes. The channel-plate (upper left corner) has its front and backside individually wired. The wedge-and-strip- anode, providing three output signals is separated from the MCP by a Ge layer, which is also attached to a power supply. For details see text.

The detector has been used in the past [171] and is described there in detail. However, since a number of modifications has been applied, these aspects shall be discussed here. Since this RoentDek MCP detector [190] is equipped with a special germanium-layer in between the anode itself and the MCP backside, both are decoupled electrically, which allows putting the electrical potential of the preamplifiers to ground. This is beneficial concerning electrical noise from the surrounding and therefore preferred.

The wedge-and-strip-anode provides three charge-signals (figure II-6) which are directly wired via short cables to the corresponding Roentdek 3-channel-preamplifier. These signals are then sent to the amplifiers (Ortec 570). The amplified and shaped pulses (shaping time 0.5 µs) are directly sent to a multi-parameter analogue-to-digital-converter (ADC) in pulse mode. This four-parameter ADC is located in a CAMAC crate (Sparrow MINICRATE Model 1000) also housing a list processor (Hytec LP1342) and a suitable CAMAC controller

(Sparrow Model 73A). The crate is connected to a PC via a SCSI bus line. The acquisition is controlled by the software tool KMax 7.1 by Sparrow Inc [191].

II.2.2.1 The position sensitive detector

As already mentioned, a MCP in chevron configuration was used as detector. It was equipped with a wedge-and-strip-anode.

The MCP needs an operating voltage between front and backside of 1.5 kV to 2.2 kV. Three individual power supplies (Ortec 660) were used to be able to operate the detector with either the front on or close to ground potential or at high negative voltage. First experiments were carried out with the latter mode only, i.e. having the MCP front at a voltage of -1.7 kV to -2 kV. This operating mode allows lower voltages at the backside of the detector, i.e. closer to the preamplifier and is therefore thought to be safer for the electronics. As a consequence, however, the ion beam is highly deflected by the strong electric field in front of the detector. Hence, the imaging quality is poor and the measured positions of beam incidence on the detector have to be strongly corrected. In order to be able to do so, a number of SIMION [45] simulations have been performed to check the magnitude of the deflection. It turned out, that under the chosen conditions (-1.8 kV at the MCP front), the measured distances had to be corrected by almost a factor of 2.

After the first proof-of-principle measurements the MCP was operated with its front at about -150 V, which is low enough to not influence the ion beam trajectories but on the other hand high enough to avoid counting electrons, which were present due to interaction of the projectiles with various parts of the beamline.

In all operating modes, the preamplifier, and therefore the anode itself, was put to ground potential. This is possible due to the existence of a germanium-layer in between the anode and the channel-plate, which could be put to high positive voltage. This layer was always operated about 50 V more positive than the MCP's backside. The signal at the wedge-and-strip-anode is hence only produced by the image charges of the original electron cloud, which is accelerated towards the Ge-layer.

The basic principle of the position encoding at the anode is the unambiguous relation of a the fraction between two special shaped electrodes (figure II-6, upper left corner) and the lateral location on the detector surface. A third electrode, the meander, is used to normalise the signals to the total deposited charge. Out of the detector one therefore gets three signals, corresponding to three charge-fractions of one event. Out of the three pulse-heights, the lateral position of the electron cloud can be extracted by a simple law:

$$\begin{aligned} x &= \frac{Q_W}{Q_W+Q_S+Q_M} \\ y &= \frac{Q_S}{Q_W+Q_S+Q_M} \end{aligned} \qquad (26)$$

where Q_i are the deposited charge at the wedge- (Q_W), the strip- (Q_S), and the meander-electrode Q_M. The actual values for the Q_i are derived from the measured values Q'_i by scaling them with a factor taking the different amplifications into account, i.e. $Q_i = c_i Q'_i$. In order to be able to determine the

calibration factors c_i, the whole detector surface was illuminated with an ion beam by scanning the beam using the deflection plates directly in front of the sample holder. The sample holder could be moved far enough out of the beam axis, so that the whole PSD can be reached. The factors were pre-determined by optimising the measured shape to be circular with an active diameter of 47 mm. In addition, a vertically fixed 200 µm wire about 1 cm in front of the MCP provided a straight line-shaped shadow, which allows a more precise determination of c_i. In order to improve the imaging, one can apply cross-talk corrections between the channels as well, but it turned out to be sufficient to use only an independent, linear calibration consisting of the calibration factors ci, as presented. Finally, the determined coordinates are rotation-transformed and mirrored in order to take the detector's orientation into account.

II.2.2.2 Data acquisition and recording

Basically, the events are recognised, the pulse heights are digitised and stored in a buffer memory inside the list processor. This buffer stores 5000 events before triggering an interrupt on the PC, which eventually reads the buffer into its memory and writes the information into an event-file.

An event is triggered by the busy-signal provided by the meander channel's amplifier, whenever the signal exceeds the lower-level. The amplifier provides a TTL pulse at its *busy*-output, which is fed into the ADC's *master-gate*-input to trigger a conversion. After such a conversion, the ADC triggers an interrupt at the list processor, which then requests the values at the ADC via the CAMAC bus and transfers the digitised values into a buffer memory. This whole transfer until the ADC is armed again consumes up to about 25 µs. In order to prevent subsequent events from invalidating the data, an artificial dead-time was introduced. Therefore, the busy pulse is stretched to a length of 30 µs and shifted by 1.5 µs. This stretched and shifted pulse is fed into the ADCs *pile-up-reject*-input (PUR). Any occurring event during this time is ignored. The pulses are counted in a rate-meter, which provides a visual reading of the impingement rate.

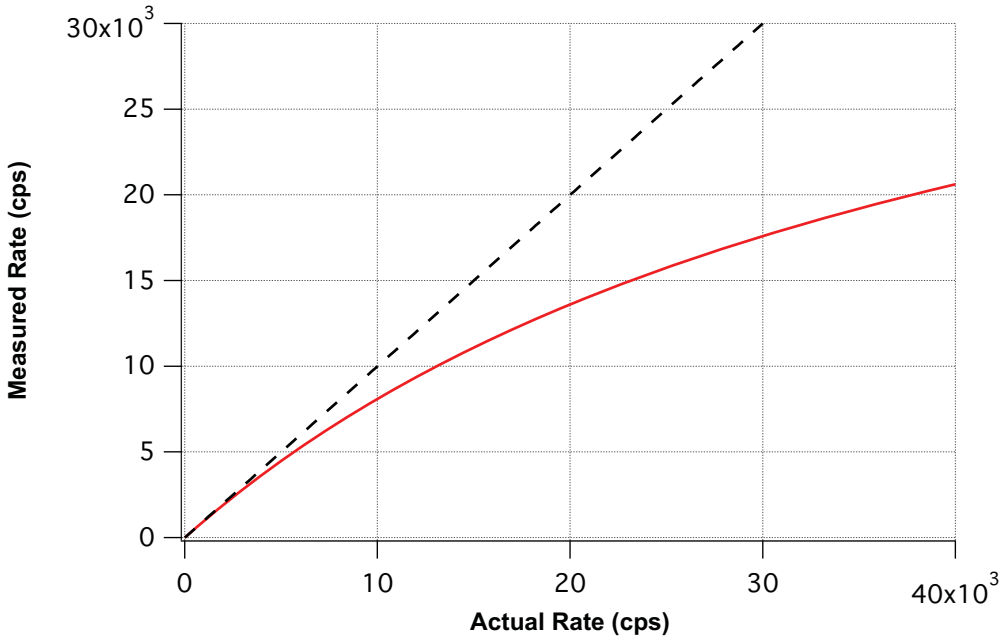

Figure II-7: Rate calibration curve
According to the proposed correction in eqs. (29) and (30), the line shows the actually measured rate as a function of the real impingement rate. The dashed line is the ideal case. For details see text.

Since the artificially introduced dead-time is a constant, one can calculate the actual impingement rate based on the measured rate under the assumption of the underlying particle statistics. As long as the creation processes for the ions are independent, one can assume a Poisson statistics, and therefore exponentially distributed waiting times between two subsequent events.

$$\mathrm{P(t)} = \frac{1}{\tau}\exp\left(-\frac{\mathrm{t}}{\tau}\right) \tag{27}$$

where $P(t)$ is the probability for an event to occur between t and $t + dt$. The characteristic time, i.e. the mean waiting time between two subsequent events to occur is τ.

An important property of the exponential waiting time distribution (27) is that the duration until the next event will occur is exponentially distributed at any time, i.e. the history does not have any influence. Therefore, a dead time τ_D, i.e. the period, during which possibly occurring events are dumped, simply extends the characteristic time of the distribution, thus $\tau' = \tau + \tau_D$. Therefore, under the given circumstances, the occurrence-rate of events R is related to the measured rate R_m by:

$$R = \frac{1}{1-\tau R_m} \tag{28}$$

As a consequence, the maximum count-rate which can be measured in a reasonable manner, where the occurring errors are not of the same order or even larger, than the actual signal, is limited to roughly 10^4 cps. As a result of the details of event recording, eq. (28) has to be slightly modified, as is going to be discussed the next paragraphs.

In order to be able to link a timestamp to each event, we introduced a two-stage timing mechanism, one on a short timescale (below about 1 s – 10 s), and one on a long-term timescale. The latter uses the computer clock to synchronise all events stored in the buffer between two subsequent transfers from the CAMAC rack to the PC. This does not provide a satisfying resolution especially at low rates, because of having a whole buffer set (5000 events) at the same time. Therefore, another timing mechanism is introduced, which accounts for the time information within one buffer set.

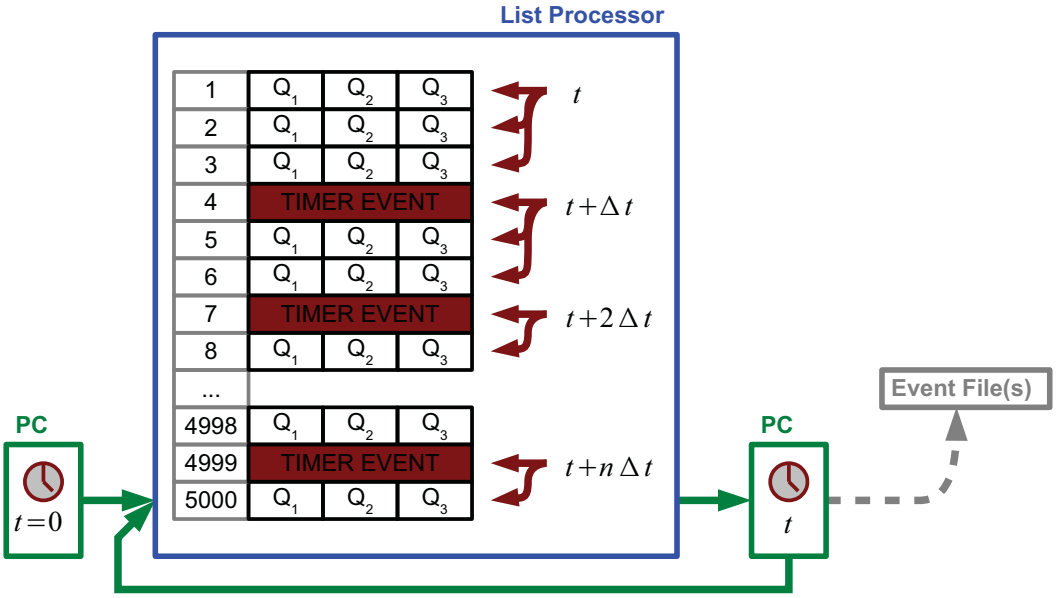

Figure II-8: Timing diagram
The illustration shows the two-step process of time-stamp creation. The PC marks every data-frame (5000 events) with an approximate beginning time. Within such a frame, trigger-events are included in fixed intervals into the event buffer, in order to reconstruct the short-term time-stamps. For details see text.

A timer at a fixed frequency (166.67 Hz) is used to trigger artificial events, which are written to the buffer (figure II-11). Therefore, every 6 ms, such a trigger-event appears in the list of events. These events are emulated by fixed numbers (58112), which cannot occur due to a real conversion event, because the number exceeds the number of conversion channels of the ADC (8k).

Whenever a whole buffer set is transferred to the PC it is immediately written to an event-file. This is an ASCII-file containing one line per event. After each event-block from one transfer, a small block is written, which contains the system time as it was before starting the acquisition of the preceding event-block. The event-file is automatically split into multiples, each of about 5 Mbytes in size.

For evaluation, these event-files can be read into an evaluation programme using the IGOR Pro data acquisition and analysis software [192]. When reading these files, the occurrence time for each event is reconstructed in the following way:

1. The PC's system time, when the acquisition at the CAMAC crate is started is recorded and assigned to the first events in the buffer next transferred to the computer.

2. By going through the buffer event by event, each time a trigger-event is recognised, the time for the next events is increased by 6 ms.

Afterwards, the rate as a function of time is reconstructed by binning the events on the time axis and eventually count rescale the bins corresponding to the bin width.

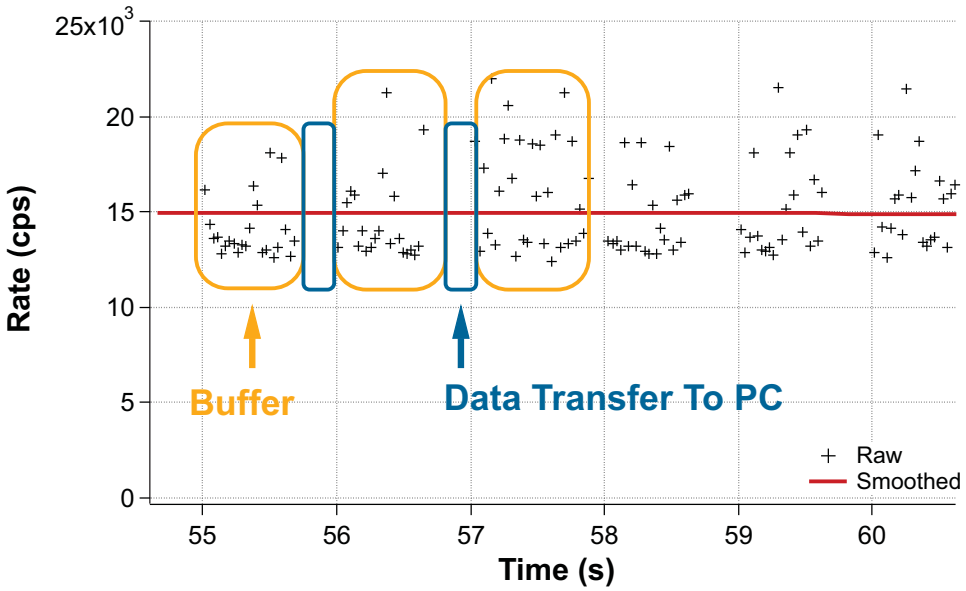

Figure II-9: Example rate plot
As indicated (yellow) there are regions, where events have been recorded, followed by the time of data transfer to the PC (blue), causing gaps in the rate. Usually, the raw data afterwards is smoothed (red line).

This way of data acquisition gives rise to the appearance of gaps of varying length (dependent on how busy the PC is) in the evaluated rates (figure II-9). Usually, these raw data are smoothed before further processing them, or, if time-independent, the mean value is determined.

Concerning the rate-correction discussed earlier in this chapter, it has to be noted, that the list processor ignores the trigger used for the timestamp-events when it is busy at that time, i.e. when a real event is being processed. In such a case, the timestamp is lost. Practically, this leads to a modification of eq. (28), since there appear less timing-events in the list than expected.

$$R_m = \frac{R}{1+\tau R}\frac{1}{1-\tau_{tr}\frac{R}{1+\tau R}} = \frac{R}{1+\tau' R} \tag{29}$$

with

$$\tau' = \tau + \tau_{tr}. \tag{30}$$

In the other direction, i.e. in the case of an event occurring while the timestamp is being processed, the correction is tiny because of the short execution time of the programme-code and is hence omitted.

The events contained in an event file (or a set of such files) provide, after the timing reconstruction, the complete information about all events occurring and can be binned with respect to the lateral position, the pulse-height, and the time

of appearance. Unfortunately it turned out, that the amplification and thus the resulting pulse height of an event is highly in homogeneously distributed across the MCP.

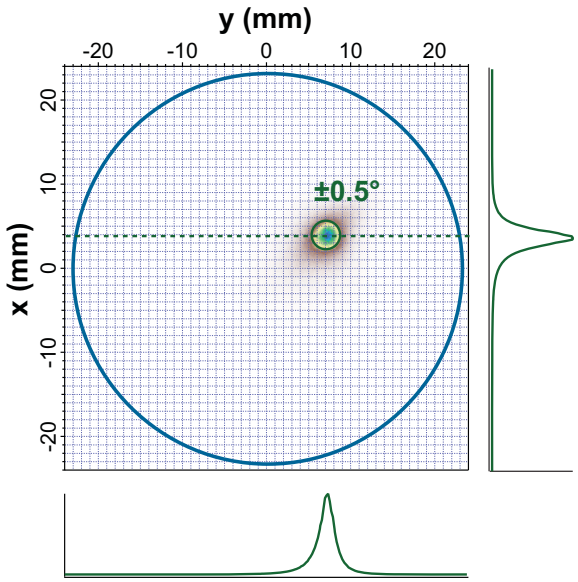

Figure II-10: Example position histogram
The beam spot is transmitted through a 100 µm reference aperture. The projections to the axes are shown. The dashed line indicates the capillary tilt plane. The estimated collimation region is shown. For details see text.

From the lateral distribution one can determine its momenta, i.e. the position and width (figure II-10 shows an example). As is being discussed in the next section, a reference aperture can be brought into the beam instead of the capillary, allowing determination of the beam intensity and beam alignment procedures as well.

II.2.2.3 The sample holder

Inside the interaction UHV chamber with a base pressure of better than about $5\ 10^{-9}$ mbar, a 3-axis manipulator is used to position the sample holder. The movement is stepper motor driven and allows a relative position accuracy of less than 20 µm. The holder is mounted on a rotatable rod, also stepper motor actuated, with an angular resolution of 0.02°. As already mentioned, the positioning is video monitored in order to guarantee the reproducibility of the absolute capillary entrance position and reference aperture respectively.

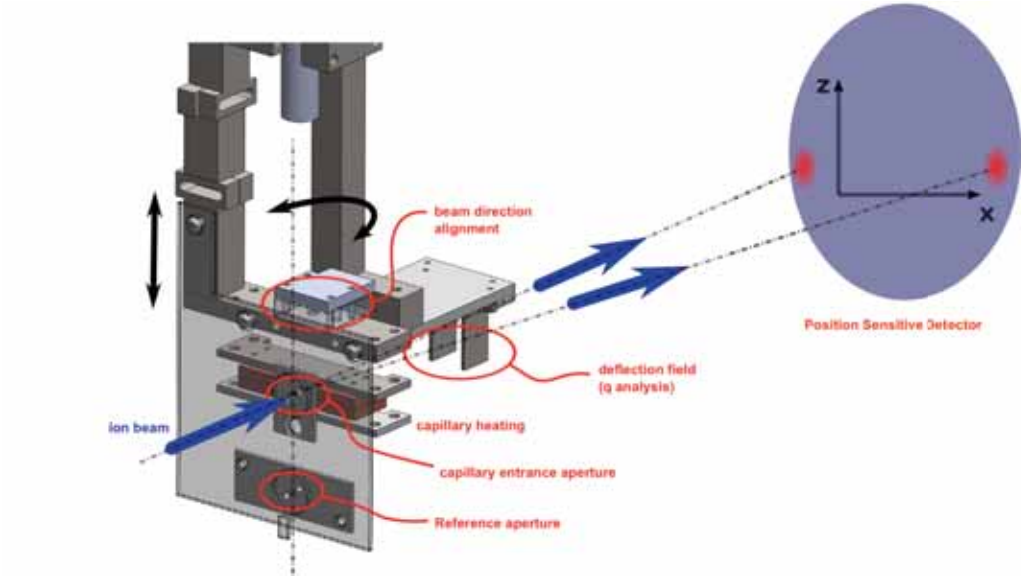

Figure II-11: Sample holder

The ion beam impinges from the left (blue). It hits the capillary entrance aperture or the reference aperture, depending on the z-position of the manipulator. Behind the capillary heating unit, containing the sample, the beam is passing a set of vertical deflectors (for q analysis). Approx. 18 cm behind the capillary, a PSD is mounted. For details see text.

The sample holder, as shown in figure II-11, is mounted on the manipulator rod and contains as major components the capillary itself, as well as a reference aperture of 100 µm diameter. A copper oven surrounds the capillary. The reference aperture is located directly under the capillary entrance and can be brought into the beam's axis by moving the sample holder 25 mm upwards. The entrance aperture position is matched with the manipulator rod's rotation axis, so that tilting the beam does not influence the aperture's lateral position.

After being transmitted through the capillary, the ions pass a pair of deflection plates, which can be used to apply a horizontal electric field. This field can be used for a charge-state-spectroscopic investigation of the transmitted beam, since the deflection angle of these projectiles is determined approximately (homogeneous field) by

$$\Delta \approx \frac{qU}{E_{kin}} \frac{l}{d} \tag{31}$$

where E_{kin} denotes the projectiles' initial kinetic energy, q their charge-state when flying through the field. The deflector geometry is characterised by the plates' distance d as well as their length l. Due to the deflection from eq. (31), the position splitting on the PSD can be used to determine the charge-state q.

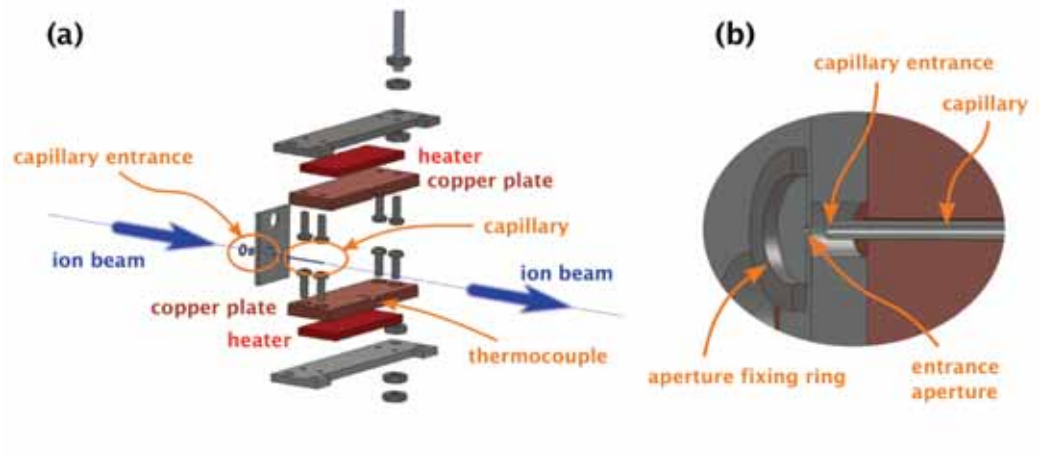

Figure II-12: Details of the sample holder
Exploded view of the heating unit (a) and a detailed cut through the entrance region (b). For details see text.

The oven consists of two copper plates surrounded by two heating units consisting of coaxial heaters, sandwiched between two stainless steel plates holding everything together. The capillary is placed inside a channel in one of the copper plates. Its counterpart has a plane surface. Just at the exit region, there is a conical cut into both plates, in order to avoid that transmitted ions showing a larger beam divergence come into close contact with the copper. The capillary samples used in this work usually have an outer diameter of 0.3 mm to 0.6 mm. In order to establish physical contact between the upper and the lower copper part, a sheet aluminum foil is filled into the gap, allowing heat transport between the two. The capillary itself is covered by graphite on its outside surface to guarantee symmetry and uniform charge transport. This graphite is also used to fix the capillary in its position and to ensure good electrical as well as thermal contact between the glass and the surrounding metal parts.

The ion beam hitting the capillary entrance would of course hit the front plane and charge the outside of the tube, which then causes deflection of the beam before actually entering the capillary. This has to be avoided. Therefore, a conductive entrance aperture is necessary, which shadows the glass front from being hit. One possibility might be to also cover the capillary's front with graphite, but this introduces the danger of having conductive material entering the glass sample, which might influence its behavior strongly. Applying a proper film of conductive material thus requires the closure of the samples entrance hole and the successive removal of this breech. We decided to use a different method for the described task, namely the placement of a metal aperture directly in front of the capillary. Of course, such an aperture needs to be perfectly aligned with the sample, which seems to be a difficult task. We chose to use a thin wire of approximately the same diameter as the capillary's inside, in the presented case this was a 120 µm silver wire, run through the capillary, to eventually pin a hole into an aluminium foil (~15 µm thick) fixed in front of the sample (figure II-12 b). Before doing so, the foil's front is covered by graphite, which improves on the one hand the mechanical properties in a way, that there does not occur buckling due to the pressure, and on the other avoids charging problems of the oxide layer on the foil. Due to the constructional details of the sample holder, the capillary protrudes the copper parts on the beam facing side by about 1 mm. The distance between the capillary front and the aluminium foil is approximately 0.4 mm. This means, that

at e.g. a tilt angle of 5°, a region of approximately 4 mm^2 is hit by the beam directly, in contrast to the case discussed first, where a conductive layer is directly applied to the surface. Nevertheless, the hit region is small in comparison to the total entrance cross section of the order of 0.01 mm^2.

At the backside of the copper plates, a K-Type thermocouple is used to monitor the temperature. The heating power of up to a few watts is regulated by a PID controller. Because of the fact, that this stabilised heating system was only capable of providing enough heating power for temperatures as high as about 50°C, constant power from an external low-voltage supply was used for heating to higher temperatures.

In order to be able to reach lower temperatures, we used heat conduction into a cold sink. Therefore, a 6 mm^2 cross section copper ribbon, attached to the sample holder, acted as conductor to a high current feed-through, and outside the UHV chamber further into a bath of liquid nitrogen. Temperatures at the chamber feed-through as low as -140°C were possible to be reached, allowing a minimum temperature of about -35°C at the sample holder. A clamp surrounded the capillary heater parts and pressed the copper ribbon from the topside and the bottom as well. Temperature stabilization was again achieved by the PID controlled heaters, heating against the attached cooling.

II.2.2.4 Alignment and measurement procedures

In the last sections, all the details about the experiment have been presented. However, before showing the obtained results, it is important to discuss the underlying measurement procedures.

Of course, before doing any guiding measurement, a projectile beam has to be available in the chamber. At first, the beam is brought through the collimator apertures and further through all succeeding elements. In order to monitor the beam on the PSD, the sample holder could be moved practically completely out of the beam's pathway. After bringing the whole ion beam onto the detector, the aperture's centre position in the chamber was determined optically with an accuracy of about 1 mm. Eventually, the beam was sent through this aperture by adjusting the deflection plates directly in front of the einzel-lens (figure II-15).

Several kinds of measurements were performed. The static ones, where no time dependence is monitored, on the one hand, and dynamic ones on the other, where the time-dependence plays a role. From the experimentalist's point of view when doing the measurement, the only difference is the proper time-synchronisation in the latter case, i.e. performing a synchronous action, like e.g. turning the beam on or off, when starting the writing into an event-file. Of course, before thinking about measuring the interaction behaviour with ions, the capillary was brought to its dedicated temperature and stabilised there for a few minutes.

When looking at the guiding power, the interesting parameter is the transmission through the capillary as a function of tilt angle. Usually these measurements started by first finding the beam through the reference aperture in its central position. Afterwards, moving the sample holder by a distance of 25 mm in the z-direction the capillary ends in the same position, the aperture has had before. The next step was maximising the transmitted intensity by tilting the capillary, in order to align the straight direction as good as possible with the projectiles. The actual measurement starts after finding stable conditions in the

straight direction. In steps of usually less than 1°, the capillary is tilted into one direction. At each step, the condition for proceeding is reaching quasi-static transmission. In this way the curve is measured stepwise until no spot can be recognised at the PSD and the transmission is practically 0. Then the measurement proceeds with the capillary in the straight direction, which is again reached by stepwise tilting. The opposite side is then measured in the same way as the one before until the transmission vanishes. Usually, after finishing such a measurement, the primary beam intensity and stability is again checked by moving the sample holder back into the reference aperture position.

Because the capillary's straight direction is always taken as with respect to the ion beam (not to the chamber axis), the centre position has to be determined for each individual measurement independently. Therefore, a Gaussian fit is applied to the datapoints, which usually agrees well with the raw data, and eventually the datapoints are shifted, in order to provide a tilt angle axis centred at the direction of maximum transmission.

It should be mentioned here, that the beam stability, especially for measurements taking several hours, is the crucial point and was quite often not satisfying. In the presented results, only those cases are selected, where the projectile beam inside the interaction chamber was stable enough for the whole measurement duration.

There are several possible reasons for the occurring instabilities, each having different characteristic behaviour, especially concerning the timescale, which can be as short as seconds or below or even up to several hours. Due to the beam collimation, small variations in the beam extraction geometry can have severe consequences concerning intensity fluctuations in the chamber, even if the total beam intensity does not vary.

The observed short term instabilities, i.e. on a time-scale of seconds or below, are off-resonance effects from the microwave plasma heating. They occur from time to time, because of the fact, that on a longer time-scale of minutes or hours the resonance conditions in the plasma chamber of the ECRIS seem to change, leading to the necessity of readjusting the heating frequency by a very small amount. Unfortunately, when doing a single measurement over several hours, it is usually not possible to adjust any source parameter during that time without influencing the beam, and thus the measurement itself. Therefore, especially these long-term measurements were challenging, because one had to find settings, which did not end up in any instabilities even after a few hours.

Whenever a time dependence is shown in this work, $t = 0$ is synchronised with some event, e.g. turning the beam on or off. After an event file is being recorded it is evaluated by a self-built tool using the IGOR Pro 6 data acquisition and analysis kit [192]. The program practically loads the event files and stores all events in the memory.

II.3 Guiding Effect First Results

First measurements have been performed not with the sample-holder shown in the last section, but a much simpler one, holding just the capillary without any heater or entrance aperture. In contrast to the later used heated holder, as presented, the sample's front was covered with graphite. Also the reference aperture was different, namely roughly 0.5 mm diameter. The whole apparatus was less sophisticated in comparison to the following temperature- and time-

dependent measurements. The beam quality at that time was also worse, because the collimation track had not been introduced. All presented results are observed at room temperature. The capillary's material was Pyrex for the very first test measurements, whereas later on, another borosilicate glass, Duran [193] had been used. The fabrication took place at the ATOMKI in Debrecen.

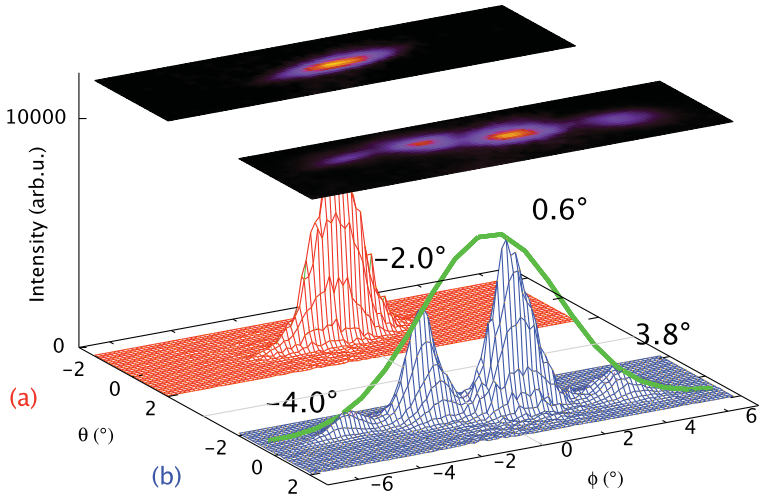

Figure II-13: First guiding observations
Two distributions on the PSD are shown: the direct beam through the reference aperture (a) and the transmitted distributions through the capillary (b) for various tilt angles (written as parameter in black). The green curve is a Gaussian fit of the transmission as a function of tilt angle, corresponding to a guiding power of ~2.9°.

Nevertheless, the results of these first proof-of-principle measurements (figure II-13) impressively showed the validity of the guiding effect for the used sample: a straight glass tube with an inner diameter of 0.16 mm at a length of 11.4 mm, thus an aspect ration of about 71. In the figure, one can see the lateral distributions on the detector (PSD) for the direct beam through the reference aperture (red) and the superposition of distributions for four different tilt angles: -4°, -2°, 0.6°, and 3.8°. The distributions are cumulative and scaled to show equal measurement durations. As projectiles, 4.5 keV Ar^{9+} ions were used. One can see, that the distributions are not circular, but elliptically shaped, which is the result of imaging aberrations caused by the PSD electronics and fixed just later.

It is important to point out, that in the case of these first measurements, several facts ensure, that the observed particles were ions, with a narrow charge-state distribution. First of all, at that time the detector was operated in a way, that a negative high voltage was applied to the front, thus the ion trajectories after passing the capillary were not straight lines, but bent curves. A SIMION [45] simulation revealed that the deflection is rather linear, i.e. there remains a linear relation between the angle at the capillary position and the lateral impact location on the PSD, with a factor of roughly 2 between the intersection with a straight line and the actual impact location. Therefore, ions could easily be distinguished from other particles like neutral atoms or photons, which of course would travel in a straight line.

The positions on the detector were first linked to passage angles at the location of the capillary via the SIMION [45] simulation, and later on fitted by the measured data to avoid systematic deviations.

From a Gaussian fit of the transmission as a function of tilt angle, the guiding power could be evaluated to be approximately 2.9° (figure II-13, green curve).

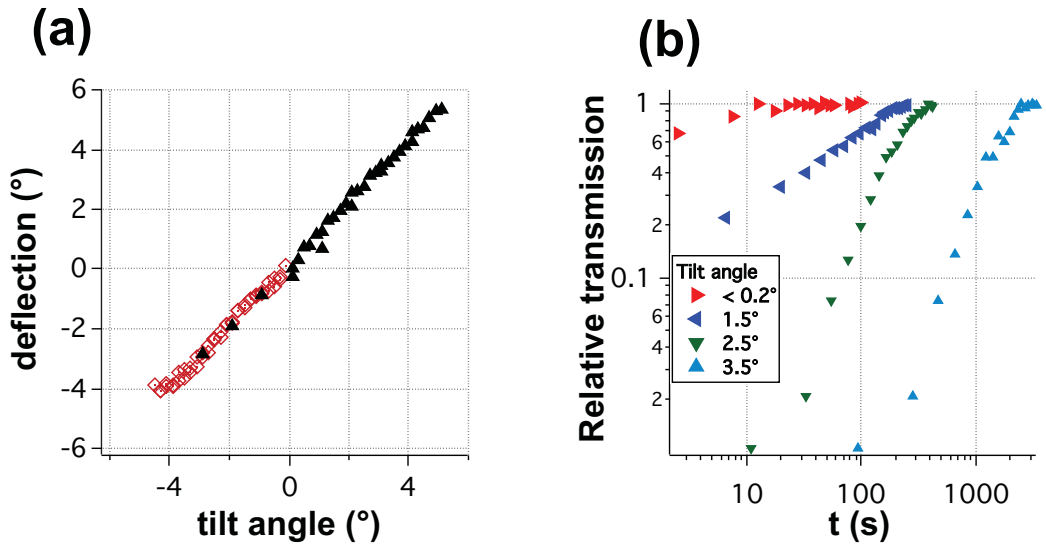

Figure II-14: Guiding through a macroscopic glass capillary
The left figure (a) shows the relation between the calculated deflection angle (from the lateral position on the PSD) and the capillary tilt angle. The red and black markers refer to different tilting history (see text). Time dependent transmission curves (b) are shown for four different tilt angles.

A linear relation between the observation angle and the capillary's tilt angle is found (figure II-14 a), as expected. If the transmitted particles had not been ions, the slope would have been different, because the deflection angle had been determined from the position on the PSD under the consideration of having Ar^{9+} particles deflected by the MCP front potential. The position information was retrieved by using the centre of gravity of the measured distributions.

At the time when these measurements were performed, it was not clear, whether the history of charging and discharging has an effect on the guiding. Therefore, we measured tilting the capillary into one direction first and later in the other. Eventually, we measured the deflection as a function of tilt angle again into the first direction, in order to see, if there appears any difference. This is also shown in the figure (figure II-14), where the first tilting direction is plotted in red, whereas the other direction and the subsequent tilting back into the first direction in black.

Another point clearly showing the transmission of ions is the time dependence. There, one can see, that the position, when changing the tilt angle, changes with time, starting off the exact agreement with the tilt angle and finally ending up in this direction. The position changing with time is not shown here, but alternatively one can take a look at the transmitted intensity (figure II-14 b), which also varies with time after the tilting event. The curves shown in the figure are measured subsequently, starting with the smallest tilt angle (practically straight direction). Afterwards, the capillary was tilted by 1.5° into one direction and the transmission was recorded. Afterwards, the capillary was tilted by another 1° into the same direction and eventually again by 1°, hence, ending up at a total tilt angle of about 3.5°. One can easily see, that the time constants involved become larger

for larger tilt angles. Parts of the charging curves can be described by an exponential law, from which one can learn a characteristic time. Qualitatively one immediately realises from the figure, that these characteristic times are growing for larger tilt angles. On the other hand, a kind of onset-time is involved, which has to be awaited until the transmission reaches a minimum value. This onset-time also strongly depends on the tilt angle.

II.4 Tuning the Guiding Effect

After understanding, that guiding also works for the single, straight glass capillary, the next step was to make one of the physical parameters involved in the guiding process accessible to variations. From the first theoretical simulations [140, 168] we know that in this first attempt, guiding could be described rather well when taking a look at just the ratio $\frac{\Delta t}{\tau_d}$, of the mean time between two impact events Δt and the mean effective discharge time τ_d.

Therefore we focused onto these two parameters, one accessible by varying the projectile beam intensity, the other by changing the material's conductivity. This was achieved, as already described in an earlier section, by adjusting the capillary's temperature at first in the range from room temperature up to about 90°C, later on, cooling abilities were also introduced to reach temperatures as low as about -35°C.

As shown in section II.5, the electrical conductivity changes in our regime roughly by an order of magnitude for each 25°C of temperature change. Thus we can cover a conductivity range of almost five orders of magnitude in total.

The measurements were performed using Ar^{9+} ions of 4.5 keV kinetic energy. The used sample was made from a borosilicate glass, its electrical conductivity measured explicitly (see section II.5), with an aspect ratio of about 71 (length 11.4 mm, inner diameter 0.16 mm).

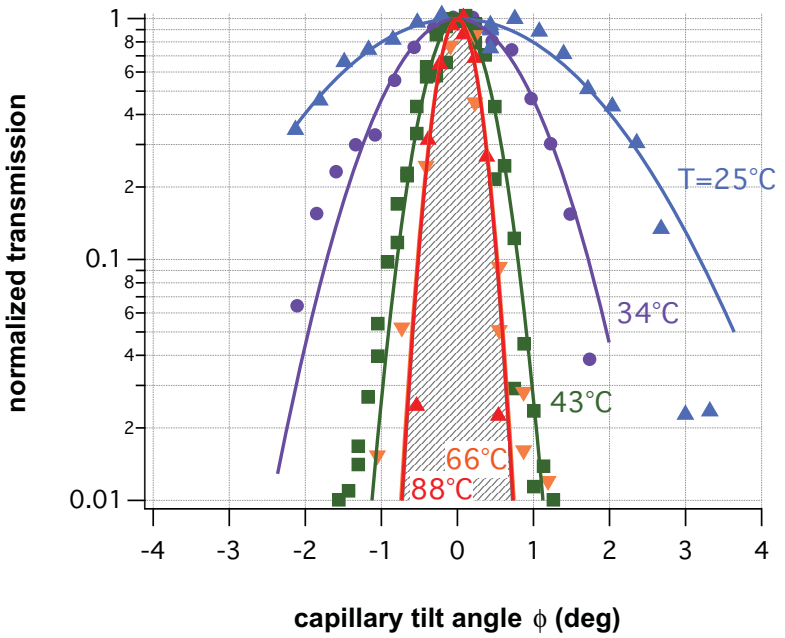

Figure II-15: Variation of the guiding power for different sample temperatures

The symbols are measured transmitted intensities, normalized to the straight direction. The capillary temperature is written as parameter. The lines are the result of a Gaussian fit through the shown points. In the centre, the geometric transmission region is shown as hatched area. The beam intensity as monitored through the reference aperture was around 5 kcps for all of the shown curves.

When looking at the stabilised regime, i.e. the equilibrium, where stable transmission is observed, we record a transmission curve by tilting the capillary and measuring the transmitted intensity. The result of such measurements for various temperatures is shown in figure II-15. All lines are Gaussian fits through the data. In all presented cases, the beam intensity as determined through the reference aperture was between about 4 and 6.5 kcps. An important fact is, as discussed in section II.2.2.4, that the centre positions are determined just after fitting the data points, thus, all data points are shifted for each individual curve.

One can clearly see, that the room temperature curve has the largest width, i.e. guiding power, whereas it drops down to a minimum at temperatures of above about 66°C. Since the width of the high temperature curves fits well with the expected geometrical opening of the capillary, corresponding to the aspect ratio of 71, and due to the fact, that the width does not change above a certain temperature value, i.e. a certain electrical conductivity, it can be seen as the geometric transmission through the capillary, which is also going to be used in the following figures. In between the room temperature curve and the ones at above 66°C, we find a variation of the guiding power parameter.

As the conductivity changes according to the temperature, from a theoretical point of view the characteristic discharge time τ_c varies. Since in the simulations [140], the main parameter is the ratio $\frac{\Delta t}{\tau_{eff}}$, with the mean time between two impact events Δt and the mean discharge time τ_{eff}, it is evident, that the beam intensity is a highly related parameter. Therefore we measured transmission curves for several different beam intensities at room temperature within the experimental limitations (see chapter II.2.2 for details).

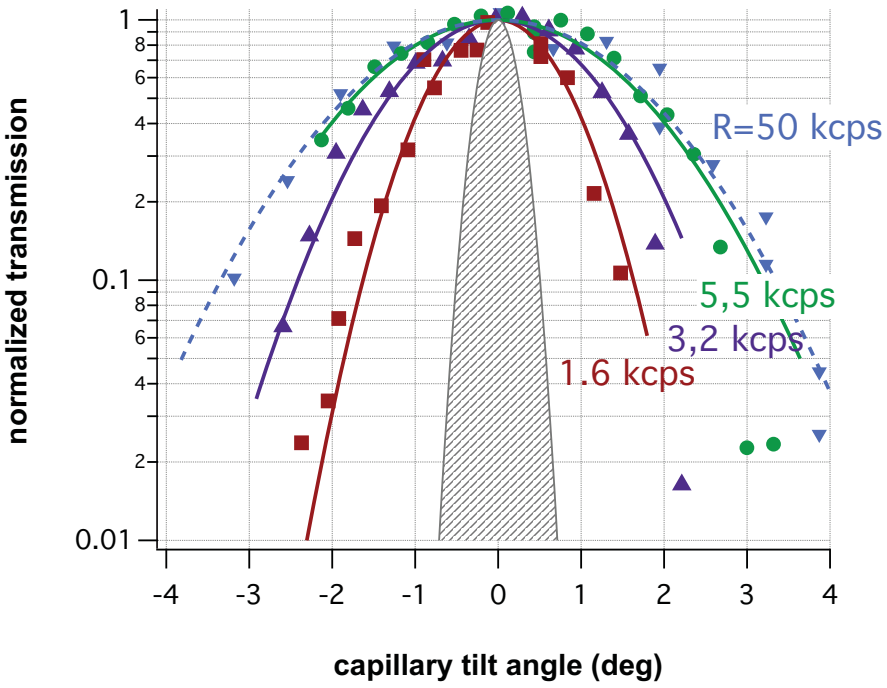

Figure II-16: Variation of the guiding power for different beam intensities
The symbols are measured transmitted intensities, normalized to the straight direction As a parameter, the transmitted intensity, as measured on the PSD in 0° direction is written. The lines are the result of a Gaussian fit through the shown points. In the centre, the geometric transmission region is shown as hatched area.

The resulting curves clearly show (figure II-16) a systematic narrowing the lower the transmitted intensity becomes. What can also be realised from this figure, is the fact, that the broadening for higher intensities, on the other side, does not continue indefinitely, but seems to weaken. At least, there is almost no difference of the guiding power between the curve measured at about 5500 cps and the one at almost a factor 10 higher intensity, at approximately 50 kcps. The respective curve is dashed to indicate, that at such high rates, the measurement accuracy is not guaranteed any more, as the dead-time induced errors become huge (see chapter II.2.2.2). The general trend of having narrower curves can qualitatively be understood from the lower equilibrium charge density, due to the lower incident rate onto the capillary's inner wall (e.g. [140]). If now, as discussed above, the ratio $\frac{\Delta t}{\tau_{eff}}$ is the determining quantity, one should be able to compensate an increase of conductivity by a corresponding change of intensity.

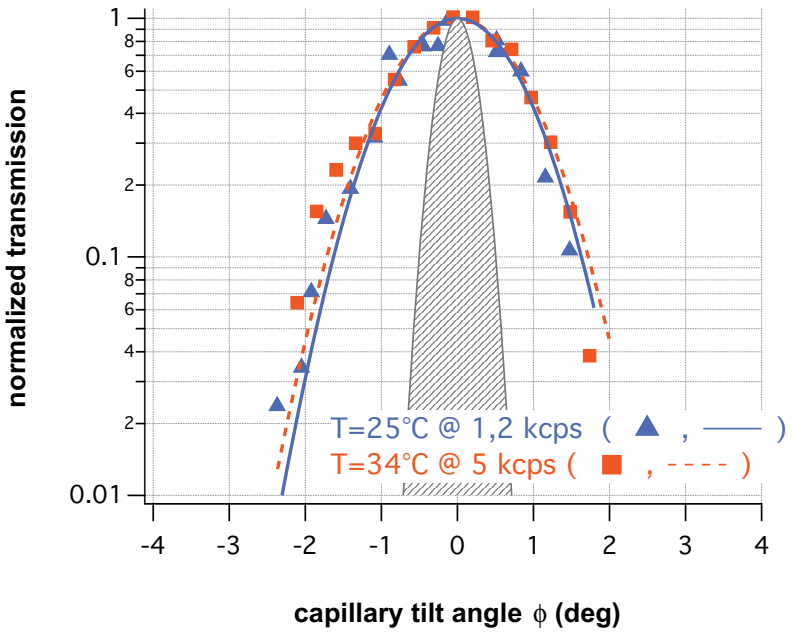

Figure II-17: Guiding power equivalence at two different temperatures
The above figure shows, as the last ones, transmission curves as a function of capillary tilt angle.

For a 10° increase in temperature of the capillary's glass, the conductivity changes by approximately a factor of 4, which can, indeed, be compensated by a 4 times increased intensity (figure II-17). As shown, the fitted curves agree very well. This fact indicates, that in the respective regime, the capillary reacts linearly to changes in the incident beam intensity, thus, the importance of the fundamental quantity $\frac{\Delta t}{\tau_{eff}}$ for the guiding is supported. It is well possible, that for larger beam intensities or lower conductivity, respectively, the linearity is not valid any more, as the resulting higher charge density at the inner wall might then induce some density-dependent effects, as reported in the literature [151].

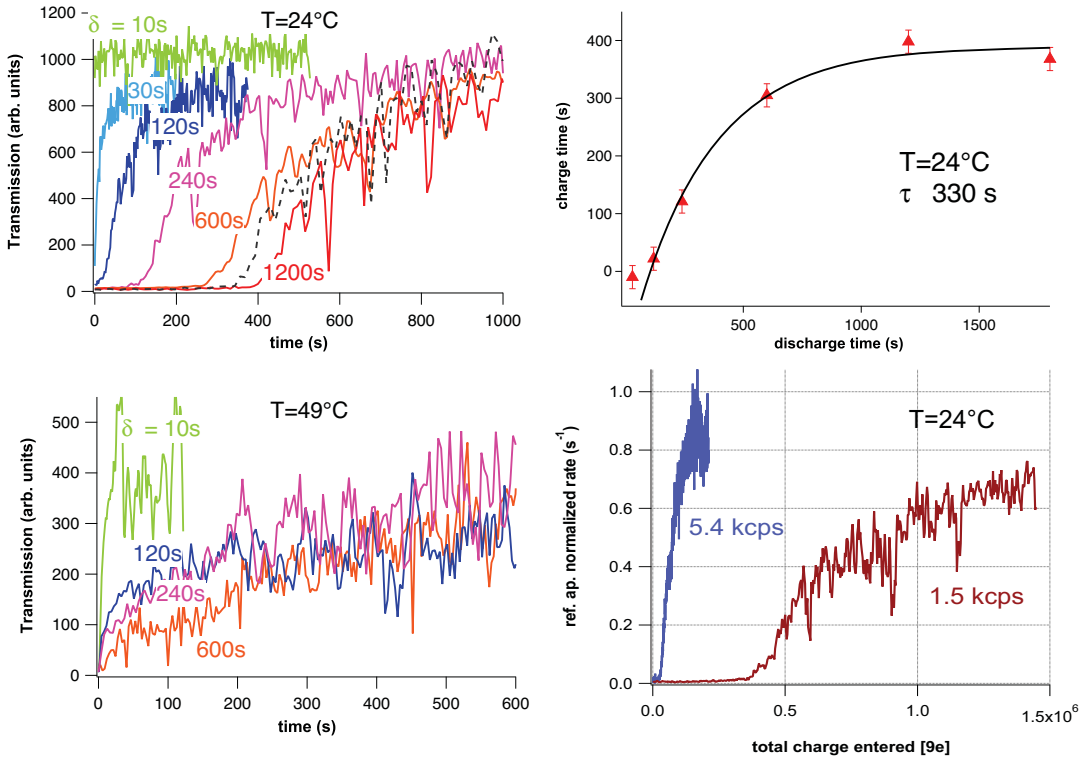

Figure II-18: Charging dynamics comparison

Transmitted intensity through the capillary as a function of time for a temperature of about 24°C (upper left) and 49°C (lower left). The parameter δ specifies the preceding discharge time. The y-axis is proportional to the transmitted beam intensity. The onset-times at room temperature are shown as a function of preceding discharge time (upper right). The symbols are the extracted values; the solid line is a fit according to eq. (32). Incident current dependence of such charge-curves is shown (lower right) at room temperature. See text for details.

When looking at the charging dynamics of the capillaries in the case of room temperature (figure II-18, upper left), one clearly realises quite distinct behaviour, where for a certain duration the transmission is very low, and eventually sets in rapidly, grows steadily according to a 1-exp law and finally saturates. This onset behaviour has also been found for nano-capillaries (see e.g. [161]). It is attributed to the formation of charge patches inside the capillary and usually accompanied by a transition from transmitted neutralised projectiles to ones with the initial charge-state.

All presented curves (figure II-18, left) were measured under a tilt angle of approximately 1.3° (The straight direction was determined just by the transmission maximum). The capillary was first charged until stable transmission was observed under the given circumstances. Afterwards, the incident beam was turned off for a duration δ between a few seconds and 10 minutes. Right after the lapse of this time, the beam was sent to the capillary again, re-charging it. The transmitted beam intensity as a function of time (with $t = 0$ being the time of turning on the beam again) reveals, that there is a strong relation between the onset time until the rate exceeds a certain limit and the preceding discharge time, directly showing the fact, that the charges are removed by conduction and have to be replaced until transmission is possible again. When plotting the onset time against

the preceding discharge time (figure II-18, upper right), one can, therefore, gather information about the effective discharge time at this temperature. Hence, the data-points were fitted by the following law:

$$\tau_1 = a - b \exp\left(-\frac{t}{\tau_{eff}}\right) \tag{32}$$

with the parameters a, b, and τ_{eff}. The fit, as shown in the figure, provides $\tau_{eff} \approx 330$ s. When elevating the temperature to higher values, one ends up with a different picture. Due to the fact, that the conductivity is expected to be higher by approximately a factor of 10, the expected effective discharge time would be of the order of 30 s. In fact, when repeating the previously described experiment with the heated capillary, but under similar conditions, one does not find the same behaviour as before. The onset time is practically 0, independent from the preceding discharge. This can possibly be plausible, when considering that the respective times might be so small, that scattering due to the stochastic nature of the guiding process exceeds them. At the increased temperature, all differences seem to be compressed by the higher conductivity, but there still remain systematic differences, also of the characteristic times in the transmission increase, after transmission sets in.

One further investigation is shown (figure II-18, lower right), where the role of beam intensity has been investigated at room temperature. There, the discharge time δ was 10 minutes for both presented curves, but the beam intensity was different by a factor of 3.6 for both, the initial charging as well as for the probing after the discharge time. The capillary tilt angle in this case was approximately 1.6°. Instead of the time evolution, as in the other figures, the total incident charge (entering the capillary) is shown at the axis, i.e. the same factor 3.6 is already used for the time-axis-scaling. In fact, the onset charges differ by about a factor of 12 (equivalent to a factor of 44 in time). According to the Literature [151], the equilibrium charge at the entrance region of the capillary does not vary with the incident beam intensity (at least in the case of nano-capillaries). Since, in such a case, the discharge dynamics of the two presented cases should behave equally, the charge distribution inside the capillary should as well be similar. Under these considerations, the huge discrepancy between the two respective onset-charges indicates, that the charge transport between two impact events has to have a major influence, although the estimated characteristic discharge time for the whole capillary is of the order of hundreds of seconds, whereas the time between two successive impact events is rather of the order of several 100 µs or milliseconds.

Returning to the quasi-static equilibrium cases discussed before, the whole systematics of the measured curves can of course be summarised by looking at the width of the fitted Gaussians as a function of transmitted rate and temperature.

Unfortunately one has to admit, that due to the inherent dynamic nature of the effect, reproducibility of dynamic features is sometimes poor. Especially the influence of primary beam instabilities onto the transmitted rate is questionable. It seems somehow, that for large tilt angles and/or low temperatures, instabilities occur possibly as a consequence of smaller variations in the incident beam flux. By choosing 4.5 keV Ar^{7+} ions, we tried to increase stability of the beam, in order to be able to also measure transmission curves as in the above figures (figure II-15, II-16) for lower temperatures.

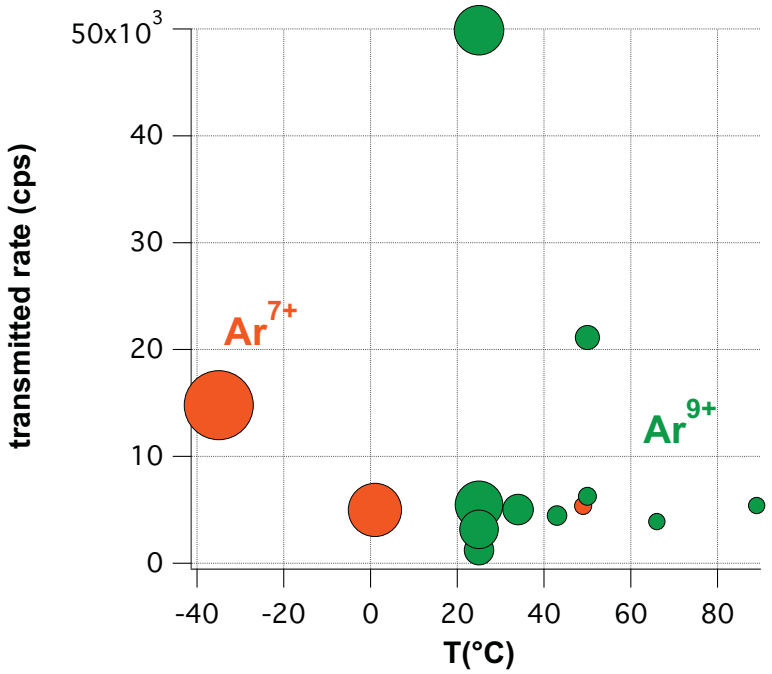

Figure II-19: Guiding power parameter
The graph gives an impression of the phenomenon's systematics. Each bubble corresponds to one Gaussian fit result with its area related to the guiding power. Most of the data are measured with Ar^{9+} (green) ions, just at lower temperatures Ar^{7+} (orange) ions have been used.

The width of the fitted Gaussians, visualised by circles (figure II-19) makes the trends easily visible. On the one hand, an increasing rate leads to an enhancement of the guiding effect, and on the other, lower temperatures, thus lower electrical conductivity, as well, increases the capillary's guiding power. The different kinds of ions are shown in different colours. The guiding power values for the Ar^{7+} were scaled up by 19%, according to the scaling laws from the literature [158], in order to be comparable with the Ar^{9+} results. The very large guiding power at -35°C is unfortunately not very reliable, because there the capillary was tilted only towards one side, thus the centre position is not very well defined.

Ar^{9+}				Ar^{7+}		
R (kcps)	T (°C)	σ (°)		R (kcps)	T (°C)	σ (°)
1.2	25	1.1		5	1	2.4
5.4	89	0.34		5.4	49	0.4
5.4	25	2.1		14.8	-35	3.3
50	25	2.2				
3.2	25	1.6				
21	50	0.8				
5	34	1.1				
4.5	43	0.5				
6.3	50	0.4				
3.9	66	0.3				

Table II-1: Fit results of the temperature dependent transmission curves
Results of the Gaussian fits to the measured transmission curves. The values for Ar^{7+} are scaled up by 19% in order to improve comparability (see text).

As already mentioned before, instabilities of the transmitted current appeared from time to time, but it is still unclear, whether these are systematic effects inside the capillary, or possibly linked to fluctuations in the primary beam, as similar behaviour has been found for a variety of temperatures and/or beam intensities. But some effects could clearly be linked to the conductivity.

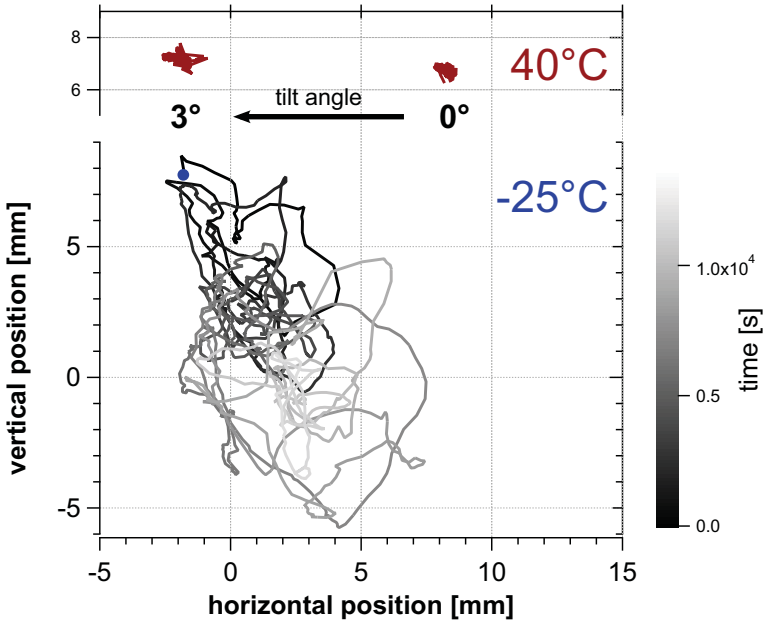

Figure II-20: Beam spot movement on the PSD
Centre positions of the beam spot at the PSD are shown for two capillary temperatures and two tilt angles. For the cold sample, only the 3° tilt curve is shown. Here, the time-evolution is colour-coded.

A quite impressive illustration of a different behaviour can be seen (figure II-20), when comparing the transmitted beam spot position on the detector for the cooled capillary and the room temperature case. In the figure, one can see the movement for a 3° tilted capillary at -25°C. These measurements were performed, using 4.5 keV Ar^{7+} projectiles. For comparison, the same plot is shown for a 40°C heated capillary, in order to show the difference. The lines show the centre positions of the measured lateral position distributions on the PSD. The time evolution is colour coded. The movement occurs similarly for 0° tilt angle. The corresponding graph is omitted just for clarity, because of the overlap with the other one. It is important to note, that the charging history is a crucial point. In the presented case, the capillary has been discharged prior to the measurement. After cooling down / heating up, the beam was turned on time-synchronised with the recording, thus $t = 0$ agrees with the charging time. Because the tilt angle is needed, it was necessary to determine the straight direction before each measurement. This happened at elevated temperatures (between 40°C and 50°C) via transmission maximisation. Right afterwards, the capillary was brought to its scheduled temperature with the ion beam being turned off. The discharging at these high temperatures is expected to be much shorter than the actual time to cool down the capillary, which is on a timescale of hours. Thus, the capillary can be considered as being discharged.

The massive movement on the PSD corresponds to emission angles out of the capillary of several degrees, which can only be explained by a charge-patch in the exit region of the capillary, moving around. Because of the low conductivity, the dynamic equilibrium cannot be reached. Instead a patch is forming, deflecting the beam too much for a smooth behaviour, which again hits the surface at another position, producing the next patch. One might also think of a scenario, where the charge density becomes too large, causing some kind of

discharge or at least enhanced transport, as e.g. suggested by others (see e.g. [142, 143, 180]).

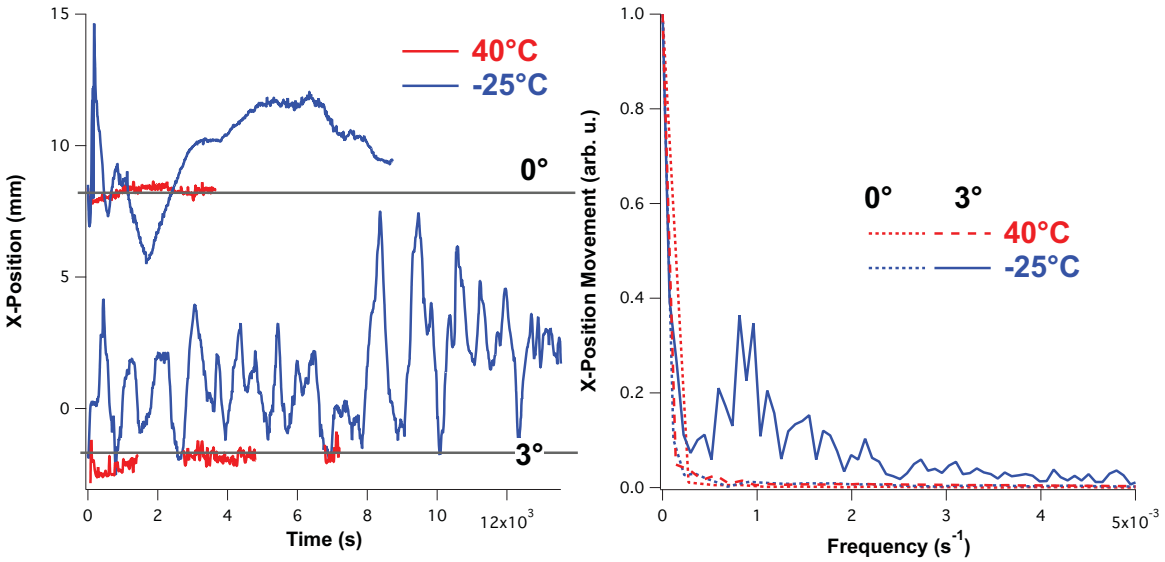

Figure II-21: Erratic movement on the PSD
The position on the detector is shown as a function of time for two tilt angles as well as for two different capillary temperatures (40°C in red, -25°C in blue). The corresponding FFTs (right) reveal the periodic nature for the 3° tilted, cold capillary.

We can take a closer look at the behaviour described above, by plotting the time-dependence of the beam spot position on the PSD (figure II-21). The shown graphs are based on the same data as in figure II-20, but only the position along the x-axis (tilting direction) is plotted as a function of time. The difference between the hot (red) and the cold (blue) capillary is evident. An additional feature is the impression, that the movement is of an oscillating nature. In fact, when looking at the corresponding fast Fourier transform (FFT) (figure II-21, right), one can see, that the 3° tilted, cold capillary shows a nice peak at about 0.09 mHz periodicity.

This oscillatory behaviour reminds one to some extent of similar periodic transmission fluctuations seen for different geometries [142, 143]. At the same time, one has to mention, that the corresponding transmission rates did not show such strong fluctuations. Again, there was no clear evidence, that the observed transmission variations are related to the guiding. This still remains an open question. Only the movement on the detector could clearly be linked to the capillary's temperature.

At another occasion, when the beam movement was detected for the first time, strong variations in the rate had actually been observed, as shown in figure II-22. This specific measurement was done at the lowest temperatures possible with the experimental setup, namely -35°C. Still, the possibility remains, that variations in the primary beam were the driving force of the fluctuations observed, but at least the fluctuations seem to occur preferably at low temperatures.

Meanwhile, the qualitative behaviour has also been shown by simulations [194], which agree with some of the measured curves quite well.

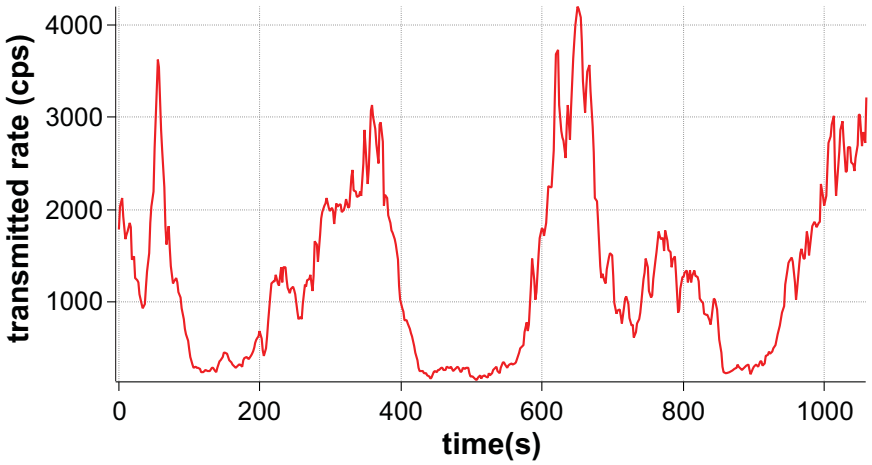

Figure II-22: Transmitted rate instabilities at -35°C
The line directly shows a transmitted rate as a function of time for a capillary at -35°C under an tilt angle of about 1°. As a result of the pronounced movement of the beam spot, it even left the active detector area in between, causing one of the count-rate-drops.

In contrast to the presented erratic behaviour, one obtains a completely different picture when cooling down a charged capillary. We did a number of measurements, where the starting situation was a heated and charged capillary. After determining the straight direction, the capillary was cooled down slowly by usually significantly less than 0.5°C per minute while the ion beam was left turned on.

Under these circumstances, neither the erratic movement on the PSD was observed in that magnitude as in the other case, even when reaching the lowest possible temperatures, nor was a systematic increase of transmission fluctuations detectable.

On the contrary, we could reach stable transmission at temperatures as low as -30°C without major movements of the beam spot. One possible explanation for this, is the fact, that existing charge-patches can be held stable even when the conductivity does not allow the self-controlled build-up of such a patch. This can just happen, as long as the ion losses into the wall material, leading to further charging, does not depend on the charge transport, but only on the actual charge density. Practically, one could think of freezing the existing charge-patches, which can therefore keep up stable transmission working even at very low conductivity.

The situation is illustrated in figure II-23, where in the left panel the direct comparison between the beam spot movement on the PSD is shown for both cases, the one, where the temperature was first set to -25°C before sending the ion beam through the capillary, and the other, where the capillary was cooled down slowly while an ion beam was transmitted through the capillary. The corresponding temperature as a function of time is shown in the right panel. Before these measurements, the capillary was aligned at an elevated temperature (40°C-50°C) with respect to the incident ion beam. The corresponding beam spot movement plots are included in the figure for comparison (see upper part of the left panel).

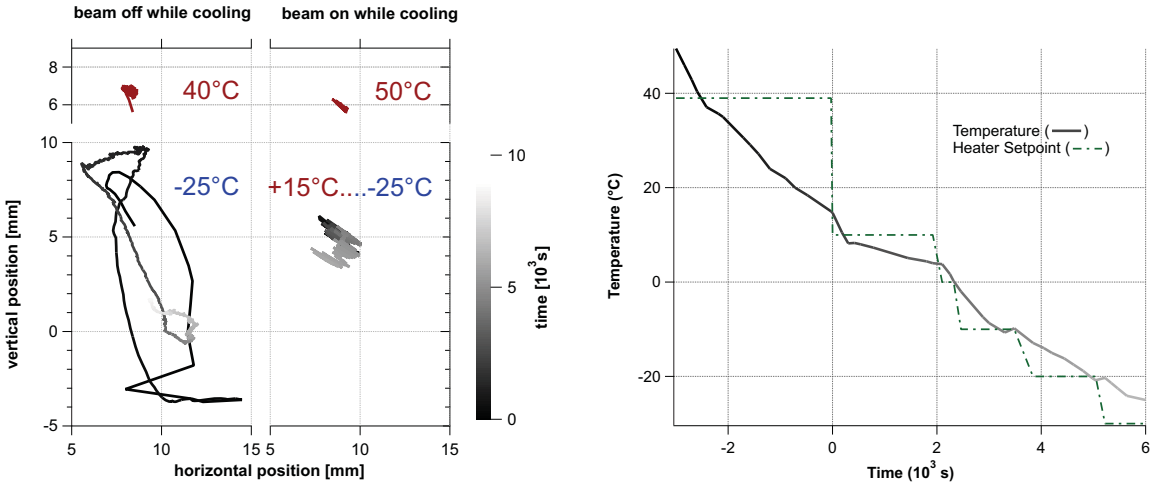

Figure II-23: Charge patch freezing - comparison between beam on/off while cooling

The beam spot movement is illustrated (left) as a function of time (colour coded). In the upper part of the figure, the transmitted spot position is shown for the heated case, right before cooling down. The corresponding temperature evolution for the smooth cooling case is shown (right) in conjunction with the heater settings, which were applied to thermalise from time to time.

II.5 Charge Transport

Because of the interests discussed in the last sections, we wanted to gain proper knowledge about the actual conductivity of the used glass, especially its behaviour as a function of temperature. Therefore, the resistivity / conductivity was measured in a simple experiment.

The actual methodology was chosen according to the DIN standards DIN IEC 93 [195].

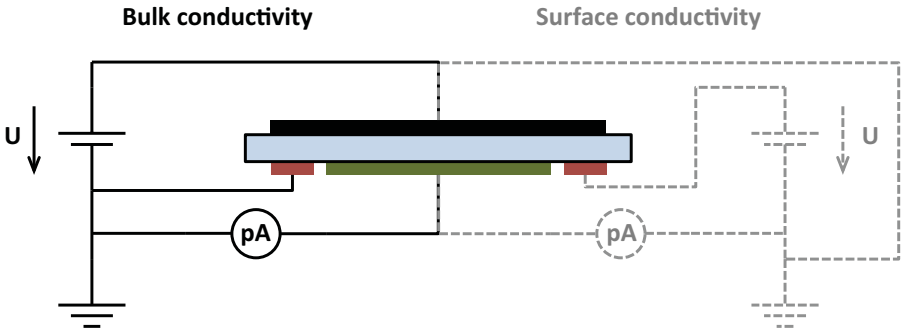

Figure II-24: Conductivity measurement
Schematic illustration of the electrical circuit used for measuring the bulk conductivity (solid lines) as well as surface conductivity (dashed lines). The glass sample (blue) is covered on one side with a circular electrode (black). On the opposite side, a ring electrode (red) is surrounding a central circular electrode (green).

The basic electrical circuit is shown in figure II-24. We used samples of the same composition as the capillaries: a borosilicate glass under the trademark Duran [193]. Graphite electrodes in a circular shape were applied to the specimen. On one side, one single electrode covers some area, on the other, a smaller circular electrode opposes the first one. It is surrounded by a ring of the same outer diameter, as the electrode on the opposite side.

In accordance to the DIN standard, the bulk conductivity is measured by grounding the outer ring, and applying a voltage between the other electrodes. The current is measured with a pico-amperemeter (Keithley 6485). We applied voltages between a few volts and 1 kV with an external power supply (Hewlett Packard 6516A). For determining the surface conductivity, the measuring voltage is applied between the ring and the inner circular electrode. A second kind of geometry was used, where the electrodes were applied to the inside and the outside, respectively, of a glass tube. There again, three electrodes were used to determine the bulk and surface conductivity independently.

From the applied voltage U and the measured current I, we obtain the specific conductivity

$$\sigma_b = \frac{s}{A}\frac{I}{U} \tag{33}$$

where s denotes the sample thickness and the effective area A, corresponding the overlap between the two opposite electrodes.
For the surface conductivity one obtains

$$\sigma_s = \frac{g}{l}\frac{I}{U} \tag{34}$$

where the gap distance between the outer ring and the inner circular electrode is denoted g, and the effective circumference l, corresponding to the outer ring electrode's inner diameter. Similar laws can be found for the tube-shaped sample geometry, which is not shown here in more detail.

In order to avoid any influence from the surrounding, the measurements were actually performed in vacuum. Therefore, stainless steel wires held the specimen

inside a standard DN 40 CF tee-piece, which was evacuated prior to the measurements using a turbo molecular pump. The vacuum vessel was heated and cooled later on, respectively, from the outside by electrical heaters on the one hand, or a fridge on the other. By this, a temperature range from about -18°C to 90°C could be covered. The actual sample temperature was monitored by a K-type thermocouple, which was attached to the glass sample.

A detailed description of the sample geometries and the measurement procedures can be found in [196].

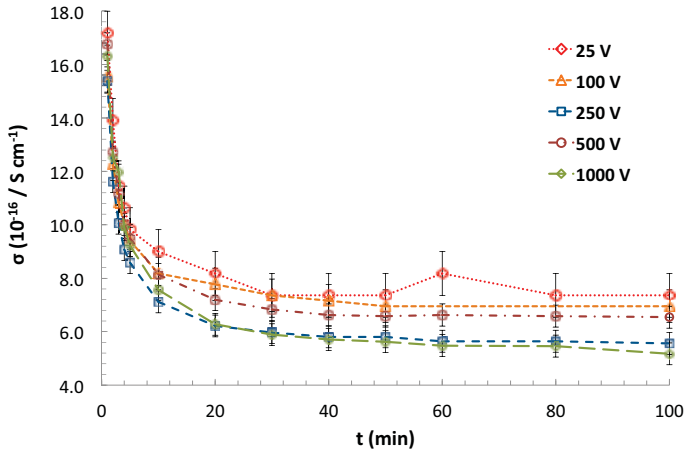

Figure II-25: Time dependency of the glasses electrical conductivity
The measured bulk conductivity as a function of time. The time $t = 0$ corresponds to the time the voltage is turned on.

When applying a voltage to the sample, the measured current starts to drop immediately, showing some exponential-like behaviour, as can be seen in figure II-25. Only after hours, an equilibrium value would be reached. Charge transport in glasses is a complex phenomenon, mainly based on the cations in the glass. The observed time dependence can be attributed to polarization effects (see e.g. [197] for a topical review). One can see, that the effect shows a weak dependence of the applied voltage.

For the presented conductivity measurement data, a voltage of 100 V was applied; this has been chosen as a compromise between avoiding high field effects on the one hand and electronic noise problems in the very low current regime, on the other.

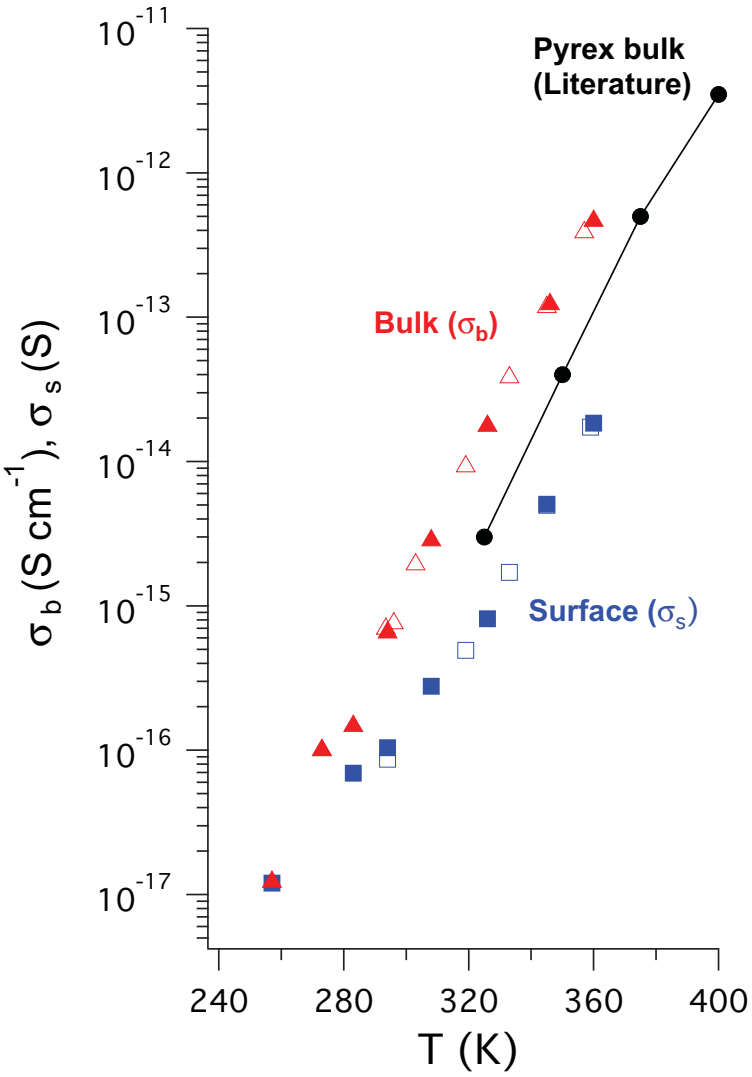

Figure II-26: Temperature dependence of the glasses specific conductivity
Results for surface- (blue) as well as bulk (red) conductivity measurements. Measurements done in vacuum (filled symbols) are shown in comparison to corresponding measurements in ambient (open symbols). Included data from the literature [198] show values for Pyrex (Type 7740), another borosilicate glass (black).

The resulting conductivity data are shown in figure II-26. Interestingly, in contrast to other materials (see e.g. [199] for Mylar), the surface conductivity is up to an order of magnitude lower, than the according bulk conductivity. At lower temperatures, however, the temperature dependence differs, leading to a crossing at about 248 K.

A comparison with total conductivity data of another borosilicate (Pyrex, Type 7740) from the literature [198] shows similar behaviour as a function of temperature, but a slightly different magnitude. Concerning the temperature dependence, however, the relative change is comparable.

II.6 The bigger picture – possible applications of Capillary Guiding

Capillaries are in fact already in use, especially for the precise placement of a swift ion beam in micro-dosimetry experiments [200]. Whether or not guiding plays any role in the beam formation is still not completely clear, but rather unlikely, since the involved energies are too high to influence the projectiles significantly by charging potentials.

Another field, where capillaries might be of value, is the nano-structuring of surfaces. As shown in section I.3, a beam of highly charged ions can be used, to place well defined single defects on a length-scale of several nanometers. This high efficient process, where each single ion impact causes a single defect, could be utilised, for high-resolution ion beam lithography, avoiding any kinetic collision cascade.

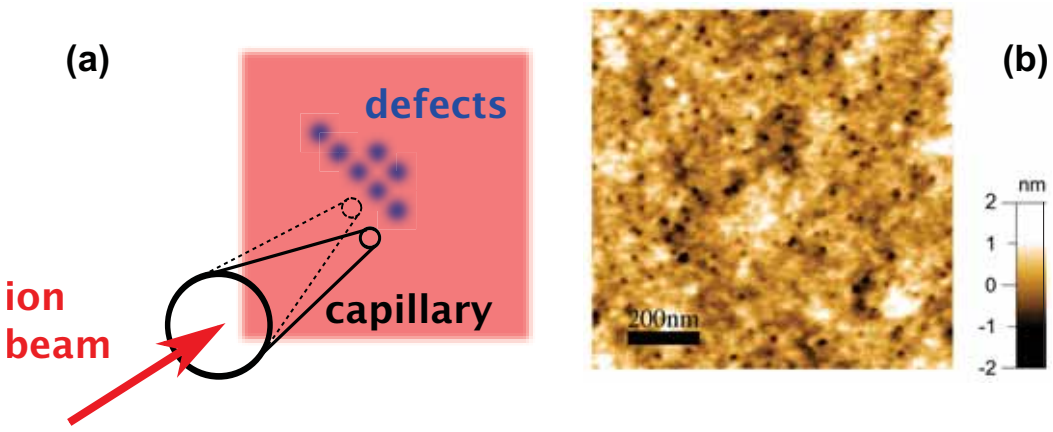

Figure II-27: Possible application for a single capillary
A tapered capillary might be used for enhancing the quality of a HCI beam, and at the same time ensure proper placement on a sample surface (left). An example, where nano-holes are created (right), shows well-defined holes in a thin film of PMMA on a Si substrate.

For doing so, of course, a high-quality highly charged ion beam is needed , with a spatial resolution of the order of tens of nanometres. One step towards this goal could be the utilisation of a capillary, which is motion controlled by some micro-mechanics, like a Piezo-drive. It is more applicable, to have the capillary fixed and use a moveable sample stage, just like in a standard SPM. Due to the possibility of detecting a single HCI impact by observation of the emitted electrons (see e.g. [88]), the placement of single defect is possible with a resolution given by the outlet diameter of the capillary. Due to progress in the manufacturing processes, it seems possible to reach diameters of the order of 100 nm soon.

II.7 The next steps – Beyond

Still there remain a lot of questions concerning capillary guiding. One key issue to a more complete theoretical understanding is the missing surface definition

inside the capillary. Up to now, no surface characterisation or cleaning procedures were applied, in order to guarantee proper surface conditions.

The strong temperature dependence of the capillary's conductivity could, therefore, act as a key feature for allowing sputter cleaning in the future. Heating a sample up to a temperature high enough to avoid charging even at high incident currents might enable the use of a sputter gun to prepare the inner surface. This might especially be applicable to tapered capillaries, which are, as discussed in the above section, a promising candidate as an ion optical tool for future highly charged ion surface lithography.

For a more profound understanding, temperature dependent measurements are still necessary, especially concerning tapered capillaries. There are efforts going on right now to provide new information about the special behaviour, those tapered samples show when changing the material's conductivity.

From the experimenter's point of view, one key issue during the measurements presented in this work was the lack of stability of the primary ion beam. It turned out, that the high requirements to the beam could hardly be fulfilled, resulting in short term, as well as long-term instabilities. Whereas variations on a short time scale can be fought against successfully, especially long term drift of the beam damaged a lot of measurements, leading to considerable extra time of experiments. Unfortunately, due to a lack of direct beam monitoring, it was hard to judge on the stability of the beam reaching the capillary, since instabilities in the transmission can also be attributed to the guiding itself, as we learned from the experiments. Therefore, for future experiments, it is highly recommended to install a primary beam monitor, which uses e.g. the secondary electrons at the entrance aperture as monitored particles. A channeltron right next to the capillary entrance, with a slightly positive voltage applied to the front, could therefore provide a count-rate, proportional to the incident ion flux.

One of the ideas for future applications is the utilisation of capillaries as an ion optical unit in a deceleration stage. A key for lithography by highly charged ions is to provide slow projectiles, in order to avoid any collisional damage to the sample. Since most ion sources provide projectiles of several keV kinetic energy, decelerating the beam via electrostatic fields is commonly used. A nice possibility, worth to be investigated in more detail, is the direct application of a capillary inside such a decelerating field in order to, at least partially, compensate the beam widening due to the deceleration. This could enhance the beam focusing in the latest stage of deceleration, right before impinging on the surface, allowing to possibly achieve better resolution by simple means without the necessity for sophisticated beam optics.

II.8 Summary

Eventually we succeeded to prove the validity of the guiding effect's concepts up to macroscopic length-scales also for a single, straight, glass capillary. The strength of the effect, the capillary's guiding power, can be influenced significantly by changing the material's conductivity. This can be achieved by changing the capillary's temperature. Therefore, cooling the capillary can be used to enhance the guiding effect. However, at low temperatures, the onset of guiding, i.e. the initial charging phase, does not lead to stable conditions (at least

not within the observation times used in this work). Nevertheless, it turns out, that already established charge-patches can be frozen by cooling down the system slowly. This might lead the way to enhanced guiding properties also at very low beam intensities.

DANK

...sei zu aller erst einmal an die Fördereinrichtungen gerichtet, die meine Arbeit finanziell unterstützt haben. Ohne die finanzielle Grundlage wäre es sicherlich nicht möglich gewesen, diese Erkenntnisse zu gewinnen und bei internationalen Konferenzen auch zu vertreten.

Dabei sind gleich mehrere Institutionen zu nennen. Untersuchungen zur Interaktion von Ionen mit fusions-relevanten Oberflächen wurden über die Österreichische Akademie der Wissenschaften gefördert (KKKÖ, EURATOM). Ganz besonders möchte ich die Bedeutung des europäischen Netzwerkes ITS-LEIF unterstreichen, das sich mit der Physik niederenergetischer Ionen beschäftigte und über einen Zeitraum von einigen Jahren substanziell zur Erforschung verschiedener Phänomene im Zusammenhang mit Ionen-Oberflächen-Wechselwirkung beigetragen hat und aus dessen Mitteln auch Teile meiner Arbeit finanziert wurden. Dabei möchte ich persönlich den Koordinator des Netzwerkes, Prof. Bernd Huber, sowie die zentrale Sekretärin, Frau Christiane Malot, hervorheben und mich auf diesem Wege für die unzähligen Male bedanken, bei denen die beiden sich auch für mich eingesetzt bzw. mich unterstützt haben.

Ganz besonderen Dank und meine tiefe Wertschätzung möchte ich meinem Chef, Prof. Friedrich Aumayr, zu Teil werden lassen. Nicht nur, dass er mich sehr in meinem Entschluss bestärkt hat, dieses Doktorats-Studium zu verfolgen, hat er darüber hinaus auch wirklich erstklassige und hingebungsvolle Betreuungsarbeit geleistet, mir viele wissenschaftliche Erfahrungen, aber auch Reisen zu Forschungseinrichtungen und Konferenzen ermöglicht, was ganz sicher keine Selbstverständlichkeit ist. Ich danke Dir, lieber Fritz, für all die Mühe, die Du für mich getrieben hast und hoffe, auch Dir im Endeffekt ein Gefühl der Zufriedenheit ob meiner abgeschlossenen Arbeit bereiten zu können.

Aber bei einem Chef bleibt es ja meist nicht, so gibt es da natürlich noch unseren Institutsvorstand, Prof. Herbert Störi, der mir seinen unglaublichen Reichtum an Erfahrung im Umgang mit Projektabwicklungen und Vakuumtechnik zur Seite stellte, und mich so in der Planung und Abwicklung der Laborinfrastruktur-Erneuerung im Ionenstrahl-Beschleuniger Labor AUGUSTIN unschätzbar unterstützt hat. Ohne seine Mitwirkung wäre dies alles sicherlich nicht so reibungsarm möglich gewesen. Auch seine tatkräftige Unterstützung bei experimentellen Arbeiten werde ich natürlich nicht vergessen.

Am Institut für Angewandte Physik (vormals Allgemeine Physik) der TU Wien gibt es zahlreiche ‚gute Geister', die für das Funktionieren aller Abläufe, Bestellungen, Reparaturen, bis hin zu den Reiseabrechnungen und Urlaubskoordinationen zuständig sind, und ihre Tatkraft für alle Mitarbeiter und Studierenden zur Verfügung stellen – Friedrich Beringer, Manuela Marik und nicht zuletzt Mag. Christine Toupal-Pinter, Ihr seid ein wirklich sehr gutes Team der Administration, und ich bin Euch für die sehr gute Abwicklung so mancher manchmal eher lästiger Materie und das gute Arbeitsklima wirklich dankbar.

Was wäre schließlich ein Experiment, ohne die unschätzbare Mithilfe unseres Elektronikers Paul Berlinger. Er hat immer ein offenes Ohr für Probleme, bietet in Sekundenschnelle Lösungsvorschläge und steht mit Rat und Tat bei jedem auch noch so kniffligen Problem zur Seite. Vielen Dank für die vielen Reparaturen, die jedes Mal auf's Neue den Betrieb eines Experimentes sicherstellen konnten.

Selbstverständlich kommt ein wissenschaftlicher Versuch auch nicht ohne gefertigte mechanische Bauteile aus. Unsere Werkstätten-Mannschaft, Wolfgang Beck, Herbert Schmidt und Rainer Gärtner; das sind Spezialisten für das Große, wie auch das Kleine, wenn es um die Erarbeitung von mechanischen Lösungen geht. Dabei hat sich der eine oder andere von ihnen schon mal selbst übertroffen. Vielen Dank Euch Dreien für die vielen, vielen Male, in denen Ihr nicht nur präzise nach Plan gearbeitet habt, sondern Euch auch zusätzlich mit Eurer Expertise eingebracht habt, um eine optimale Lösung zu ermöglichen!

Und wenn niemand mehr weiter weiß, dann geht man am besten zu Prof. Michael Schmied - der weiß Rat! Es ist beinahe unglaublich, aber ich könnte mich nicht erinnern, ihn jemals um eine Antwort verlegen erlebt zu haben. Lieber Michael, alleine schon für mein Staunen über den Reichtum Deiner Erfahrungen und Ideen, die Du jederzeit auch mit anderen teilst, würde ich Dir danken wollen, aber zusätzlich hast Du nicht bloß einmal auch tatenreich unsere Vorhaben unterstützt, was noch extra hervorgehoben sein will.

Wenn nun ein Experiment steht, so will es auch betrieben werden. Im Laufe der Jahre sind nun tatsächlich viele Studenten an den verschiedenen Experimenten beteiligt gewesen, die hier in dieser Arbeit vorgestellt werden. Und selbst wenn nicht alles immer so gut läuft und durchaus der eine oder andere Versuch gescheitert ist, so haben doch alle fleißig mitgearbeitet und teilweise außergewöhnliche Leistungen erzielt. Ich danke selbstverständlich allen, die mitgewirkt haben; ganz besonders Friedrich Ladinig und Elisabeth Gruber, die wirklich außergewöhnlichen Einsatz gezeigt haben bzw. immer noch beweisen und auch das eine oder andere Wochenende investiert haben. Und natürlich gehört hier auch Paulus Naderer genannt, der sich wirklich in äußerstem Maß bemüht, das AUGUSTIN-Labor zu verbessern, wo es nur geht und sich voller Tatendrang den kniffligsten Aufgaben stellt. Wenn es um die Tätigkeiten im Labor geht, dann nehme ich gerne auch MSc. Réka Bereczky in die Liste der herausragenden Helfer auf, die mehrmals bei ihren Messaufenthalten in Wien nicht bloß praktische Arbeit am Experiment geleistet hat, sondern darüber hinaus auch mit ihrer fröhlichen und hingebungsvollen Art zu einem wirklich guten Klima und einer lustigen Zeit beigetragen hat.

Ich danke Euch allen von Herzen für Eure Aufopferung, Euren Fleiß und auch für das wirklich tolle und sehr nette Arbeitsklima und den vielen Spaß, den wir gemeinsam hatten und haben. Nicht zu vergessen ist DI Katharina Igenbergs, die nicht nur für unablässige Versorgung mit Kaffee kämpfte und damit die Produktivität der Gruppe unermesslich steigerte, sondern auch immer wieder, ob der Schilderung ihrer Probleme, zum Nachdenken über physikalische Grundlagen anregte und uns damit alle auf Trab hielt. Vielen Dank!

Bei den vielen Messaufenthalten in Frankreich wäre sicherlich nicht alles so gut gelaufen, wenn ich nicht stets auf die Unterstützung der Crew bauen hätte können. Prof. Marcel Toulemonde, Prof. Bernd Huber, Dr. Jimmy Rangama und Dr. Arek Lawicky, Ihr habt wirklich sehr professionell gearbeitet und uns immer wieder eine wirklich schöne, angenehme, aber auch produktive Zeit in Caen ermöglicht. Merci beaucoup! Gleiches gilt für das Team der Heidelberg EBIT, Prof. José Crespo und Dr. Rainer Ginzel, sowie die tolle Betreuung am Forschungszentrum Dresden-Rossendorf durch Dr. Rene Heller und Prof. Stefan Facsko. Nochmals meinen herzlichen Dank an Euch alle für die gute Betreuung und die darüber hinaus gehenden Hilfestellungen! In diesem Zusammenhang denke ich gerne auch an die lustigen Seiten der Messaufenthalte mit Dr. Walter Meissl und DI Robert Ritter, deren Faszination für Poker mich selbst immer wieder in

Erstaunen versetzt. Von Dir, Walter, konnte ich, trotz unserer kurzen Zusammenarbeit, unglaublich viel lernen und mir ein Beispiel an der Professionalität und hartnäckigen Herangehensweise nehmen; Robert, Du bist ein so geduldiger und genau arbeitender Mensch, wie man es sich für AFM Untersuchungen nicht besser wünschen könnte; und der beste Arnold-Immitator weit und breit. Vielen Dank für die angenehme und spannende Zusammenarbeit!

Von Herzen dankbar bin ich DI Katharina Dobeš für eine wirklich schöne gemeinsame Zeit hier am Institut. Im Laufe von vielen gemeinsamen Stunden im Labor hier und andernorts hast Du, liebe Kathi, mein Dasein sowohl bei den verschiedensten Diskussionen zu technisch-physikalischen Problemstellungen, als auch bei privaten Gesprächen und nicht zuletzt bei sportlichen Aktivitäten sehr bereichert. Die enge Freundschaft, die sich zwischen uns entwickelt hat, ist eine Stütze für mich und gibt immer wieder aufs Neue Anlass zu großer Freude. Ohne die Unterstützung meiner Familie und Freunde, wäre es mir freilich nicht in dieser Art möglich gewesen, hierher zu gelangen. Ich kann nicht alle Freunde, die mich in der Zeit der Entstehung dieser Arbeit aufgebaut und gestützt haben aufzählen, aber ich weiß, dass sich jeder Betroffene darüber im Klaren ist und meinen aufrichtigen Dank verspürt. Selbstverständlich haben meine Eltern einen nicht unwesentlichen Beitrag dazu geleistet, dass ich meine Dissertation letztlich abschließen kann. Für all die Unterstützung danke ich Euch von Herzen!

Eine Extraportion Dank verdient sicherlich meine Frau Claudia für ihre Extraportion an Geduld und Verständnis, sowie Liebe und Zuneigung, die sie mir in all den Jahren entgegen gebracht hat. Ich liebe Dich und danke Dir für jeden gemeinsamen Tag! Und meine lieben kleinen Kinderleins, Elena und Paul, Ihr zwei werdet hier auch verewigt – alleine schon für die Mitarbeit im Labor, aber natürlich auch für die wundervollen Stunden, die wir abseits der Arbeit gemeinsam erlebt haben und die Kraft, die Ihr mir dadurch geschenkt habt.

Um abschließend noch ein wenig Verwirrung zu stiften, richte ich noch meinen herzlichsten Dank an Leila (und ihren Widerpart Emil), die mich ein Stück meines Weges begleitet haben und eine Bereicherung für mein ganz persönliches Universum sind! ☺

감사합니다

BIBLIOGRAPHY

[1] R. Bereczky, G. Kowarik, F. Aumayr, and K. Tökesi, Nuclear Instruments and Methods in Physics Research Section B: Beam Interactions with Materials and Atoms **267**, 317 (2009).
[2] S. Facsko, W. Meissl, R. Heller, R. Wilhelm, A. S. El-Said, G. Kowarik, R. Ritter, and F. Aumayr, Journal of Physics: Conference Series; Xxvi International Conference on Photonic, Electronic and Atomic Collisions **194** (2009).
[3] R. Ginzel, S. G. Higgins, P. Mrowcynski, P. Northway, M. C. Simon, H. Tawara, J. R. C. Lopez-Urrutia, J. Ullrich, G. Kowarik, R. Ritter, W. Meissl, C. Vasko, C. Goesselsberger, A. S. El-Said, and F. Aumayr, Nuclear Instruments and Methods in Physics Research Section B-Beam Interactions with Materials and Atoms **268**, 2972 (2010).
[4] D. Kovacs, and D. Diesing, Physical Review B **81**, 1098 (2010).
[5] D. Kovacs, A. Golczewski, G. Kowarik, F. Aumayr, and D. Diesing, Physical Review B **81** (2010).
[6] G. Kowarik, R. J. Bereczky, F. Aumayr, and K. Tőkési, Nuclear Instruments and Methods in Physics Research Section B: Beam Interactions with Materials and Atoms **267**, 2277 (2009).
[7] G. Kowarik, M. Brunmayr, and F. Aumayr, Nuclear Instruments and Methods in Physics Research Section B: Beam Interactions with Materials and Atoms **267**, 2634 (2009).
[8] G. Kowarik, E. Gruber, K. Iskratsch, and F. Aumayr, Nuclear Instruments and Methods in Physics Research Section B: Beam Interactions with Materials and Atoms **269**, 964 (2011).
[9] J. Lorincik, Z. Sroubek, M. Brunmayr, G. Kowarik, and F. Aumayr, Applied Surface Science **255**, 6303 (2009).
[10] S. N. Markin, D. Primetzhofer, S. Prusa, M. Brunmayr, G. Kowarik, F. Aumayr, and P. Bauer, Physical Review B **78**, 195122 (2008).
[11] T. Peters, C. Haake, D. Diesing, D. A. Kovacs, A. Golczewski, G. Kowarik, F. Aumayr, A. Wucher, and M. Schleberger, New Journal of Physics **10**, 073019 (2008).
[12] R. Ritter, G. Kowarik, W. Meissl, A. S. El-Said, L. Maunoury, H. Lebius, C. Dufour, M. Toulemonde, and F. Aumayr, Vacuum **84**, 1062 (2010).
[13] R. Ritter, G. Kowarik, W. Meissl, L. Suss, L. Maunoury, H. Lebius, C. Dufour, M. Toulemonde, and F. Aumayr, Nuclear Instruments & Methods in Physics Research Section B-Beam Interactions with Materials and Atoms **268**, 2897 (2010).
[14] P. Sigmund, *Stopping of heavy ions - A theoretical approach* (Springer, 2004), Vol. 204, pp. 1.
[15] F. Aumayr, and H. P. Winter, *Potential electron emission from metal and insulator surfaces* (Springer Berlin / Heidelberg, 2007), Vol. Volume 225.
[16] D. Hasselkamp, H. Rothard, K. O. Groeneveld, J. Kemmler, P. Varga, and H. Winter, *Particle induced electron emission II* (Springer, 1992), Vol. 123.
[17] G. Lakits, F. Aumayr, M. Heim, and H. Winter, Physical Review A **42**, 5780 (1990).
[18] P. Tiwald, C. Lemell, G. Wachter, and J. Burgdörfer, Journal of Physics: Conference Series **257** (2010).
[19] G. Kowarik, Diplomarbeit, TU Wien, (2007), unpublished
[20] Zeiss Helium Ion Microscope. 2011; Available from: http://www.smt.zeiss.com/C1256E4600307C70/ContainerTitel/Orion_Plus/$File/orion.html.
[21] H. Eder, A. Mertens, K. Maass, H. Winter, H. P. Winter, and F. Aumayr, Physical Review A **62**, 052901 (2000).
[22] J. Limburg, S. Schippers, R. Hoekstra, R. Morgenstern, H. Kurz, M. Vana, F. Aumayr, and H. P. Winter, Nuclear Inst. and Methods in Physics Research B **115**, 237 (1996).
[23] S. Ullah, A. H. Dogar, M. Ashraf, and A. Qayyum, Chinese Physics B **19** (2010).
[24] N. Bundaleski, H. Khemliche, P. Rousseau, A. Cassimi, L. Maunoury, and P. Roncin, Journal of Physics: Conference Series **163**, 012091 (2009).
[25] M. Vana, F. Aumayr, P. Varga, and H. P. Winter, Nuclear Instruments and Methods in Physics Research Section B: Beam Interactions with Materials and Atoms **100**, 284 (1995).
[26] M. Vana, and et al., EPL (Europhysics Letters) **29**, 55 (1995).
[27] H. Eder, F. Aumayr, and H. Winter, Nuclear Instruments and Methods in Physics Research B **154**, 185 (1999).
[28] R. A. Baragiola, E. V. Alonso, and A. O. Florio, Physical Review B **19**, 121 (1979).
[29] J. Lindhard, and M. Scharff, Physical Review **124**, 128 (1961).
[30] W. Ploch, Zeitschrift für Physik A Hadrons and Nuclei **130**, 174 (1951).
[31] R. A. Baragiola, E. V. Alonso, J. Ferron, and A. Oliva-Florio, Surface Science **90**, 240 (1979).
[32] C. Kittel, *Introduction to Solid State Physics* (John Wiley & Sons, 2011).
[33] N. W. Ashcroft, and N. D. Mermin, *Solid State Physics* (Harcourt College Publishers, 1976).

[34] E. S. Parilis, L. M. Kishinevsky, N. Y. Turaev, B. E. Baklitzky, F. F. Umarov, V. K. Verleger, S. L. Nizhnaya, and I. S. Bitensky, *Atomic collisions on solid surfaces* (Elsevier Science, 1993).
[35] E. V. Alonso, R. A. Baragiola, J. Ferr\'on, M. M. Jakas, and A. Oliva-Florio, Physical Review B **22**, 80 (1980).
[36] F. Aumayr, and H. Winter, Philosophical Transactions of the Royal Society A **362**, 77 (2004).
[37] A. L. Morton, and et al., Physica Scripta **1988**, 157 (1988).
[38] H. D. Hagstrum, Physical Review **89**, 244 (1953).
[39] J. P. Briand, L. de Billy, P. Charles, S. Essabaa, P. Briand, R. Geller, J. P. Desclaux, S. Bliman, and C. Ristori, Physical Review Letters **65**, 159 (1990).
[40] E. Galutschek, E. Salzborn, F. Aumayr, and H. P. Winter, High Energy Physics and Nuclear Physics-Chinese Edition **31**, 66 (2007).
[41] E. Galutschek, Dissertation, Technische Universität Wien, (2005), unpublished
[42] H. Eder, Dissertation, Technische Universität Wien, (2000), unpublished
[43] M. Brunmayr, Diplomarbeit, Technische Universität Wien, (2008), unpublished
[44] J. Schou, Physical Review B **22**, 2141 (1980).
[45] D. J. Manura. SIMION8.0. 2008; Available from: http://www.simion.com.
[46] W. Meissl, Dissertation, TU Wien, (2008), unpublished
[47] Webelements. 2011; Available from: http://webelements.com/copper/physics.html.
[48] SolidWorks. 2005; Available from: http://www.solidworks.com/.
[49] E. Gruber, Bachelor Thesis, Technische Universität Wien, (2009), unpublished
[50] R. Neu, R. Dux, A. Kallenbach, T. Pötterich, M. Balden, J. C. Fuchs, A. Herrmann, C. F. Maggi, M. O'Mullane, R. Pugno, I. Radivojevic, V. Rohde, A. C. C. Sips, W. Suttrop, and A. Whiteford, Nuclear Fusion **45**, 209 (2005).
[51] M. Mayer, R. Behrisch, H. Plank, J. Roth, G. Dollinger, and C. M. Frey, Journal of Nuclear Materials **230**, 67 (1996).
[52] J. Roth, E. Tsitrone, and A. Loarte, Nuclear Instruments and Methods in Physics Research Section B: Beam Interactions with Materials and Atoms **258**, 253 (2007).
[53] N. Schupfer, D. D. T. sr, R. Khanal, S. Kuhn, F. Aumayr, S. F. da Silva, and H. P. Winter, Plasma Physics and Controlled Fusion **48**, 1093 (2006).
[54] H. D. Hagstrum, Physical Review **104**, 1516 (1956).
[55] H. D. Hagstrum, Phys.Rev. **96**, 336 (1954).
[56] *Handbook of Chemistry and Physics* (CRC Press.
[57] L. M. Kishinevsky, Radiation Effects **19**, 23 (1973).
[58] U. A. Arifov, L. M. Kishinevskii, â. S. Mukhamadiev, and â. S. Parilis, Soviet Physics -- Technical Physics (engl. transl.) **18** (1973).
[59] N. Moslemzadeh, and S. D. Barrett, Surface Science **600**, 2299 (2006).
[60] J. B. Hasted, Journal of Applied Physics **30**, 22 (1959).
[61] T. F. Moran, and J. B. Wilcox, The Journal of Chemical Physics **68**, 2855 (1978).
[62] C. Lemell, A. Arnau, Burgd, ouml, and J. rfer, Physical Review B **75**, 014303 (2007).
[63] J. E. Valdés, J. C. Eckardt, G. H. Lantschner, and N. R. Arista, Physical Review A **49**, 1083 (1994).
[64] E. A. Figueroa, E. D. Cantero, J. C. Eckardt, G. H. Lantschner, J. E. Valdés, and N. R. Arista, Physical Review A **75**, 010901 (2007).
[65] I. Mertig, and et al., Journal of Physics F: Metal Physics **10**, 407 (1980).
[66] D. E. Eastman, Physical Review B **2**, 1 (1970).
[67] H. Eder, M. Vana, F. Aumayr, and H. P. Winter, Review of Scientific Instruments **68**, 165 (1997).
[68] G. Lakits, A. Arnau, and H. Winter, Physical Review B **42**, 15 (1990).
[69] I. C. Gebeshuber, S. Cernusca, F. Aumayr, and H. P. Winter, International Journal of Mass Spectrometry **229**, 27 (2003).
[70] J. I. Juaristi, C. Auth, H. Winter, A. Arnau, K. Eder, D. Semrad, F. Aumayr, P. Bauer, and P. M. Echenique, Physical Review Letters **84**, 2124 (2000).
[71] W. Meissl, D. Winklehner, F. Aumayr, M. C. Simon, R. Ginzel, J. R. C. López-Urrutia, B. S. J. Ullrich, and J. Burgdörfer, e-Journal of Surface Science and Nanotechnology **6** (2008).
[72] A. Mertens, S. Lederer, K. Maass, H. Winter, J. St√ ∂ ckl, H. P. Winter, and F. Aumayr, Physical Review B - Condensed Matter and Materials Physics **65**, 1324101 (2002).
[73] J. Stöckl, T. Suta, F. Ditroi, H. P. Winter, and F. Aumayr, Physical Review Letters **93** (2004).
[74] K. Töglhofer, F. Aumayr, and H. P. Winter, Surface Science **281**, 143 (1993).
[75] F. Aumayr, G. Lakits, and H. P. Winter, Applied Surface Science **47**, 139 (1991).
[76] J. Burgdörfer, P. Lerner, and F. W. Meyer, Phys.Rev.A **44**, 5674 (1991).
[77] K. Töglhofer, F. Aumayr, H. Kurz, H. Winter, P. Scheier, and T. D. Märk, Nuclear Instruments and Methods in Physics Research Section B: Beam Interactions with Materials and Atoms **88**, 44 (1994).

[78] A. Billebaud, D. Dauvergne, M. Fallavier, R. Kirsch, J. C. Poizat, J. Remillieux, H. Rothard, and J. P. Thomas, Nuclear Instruments and Methods in Physics Research Section B: Beam Interactions with Materials and Atoms **112**, 79 (1996).
[79] A. M. Borisov, E. S. Mashkova, and E. S. Parilis, Vacuum **66**, 145 (2002).
[80] H. P. Winter, M. Vana, C. Lemell, and F. Aumayr, Nuclear Instruments and Methods in Physics Research Section B: Beam Interactions with Materials and Atoms **115**, 224 (1996).
[81] S. Markin, D. Primetzhofer, and P. Bauer, Physical Review Letters **103** (2009).
[82] U. Even, P. J. de Lange, H. T. Jonkman, and J. Kommandeur, Physical Review Letters **56**, 965 (1986).
[83] F. A. Fernandez-Lima, V. T. Pinnick, S. Della-Negra, and E. A. Schweikert, Surface Interface Analysis **43** (2011).
[84] E. Hendell, and U. Even, The Journal of Chemical Physics **103**, 9045 (1995).
[85] O. Kamalou, J. Rangama, J. M. Ramillon, P. Guinement, and B. A. Huber, Review of Scientific Instruments **79**, 063301 (2008).
[86] H. Rothard, K. Kroneberger, E. Veje, A. Clouvas, J. Kemmler, uuml, rgen, P. Koschar, N. Keller, S. Lencinas, P. Lorenzen, O. Heil, D. Hofmann, and K.-O. Groeneveld, Physical Review B **41**, 3959 (1990).
[87] S. V. Verkhoturov, M. J. Eller, S. Della-Negra, R. D. Rickman, J. E. Lockleard, and E. A. Schweikert, Surface Interface Analysis **43** (2011).
[88] W. Meissl, M. C. Simon, J. R. Crespo Lopez-Urrutia, H. Tawara, J. Ullrich, H. P. Winter, and F. Aumayr, Review of Scientific Instruments **77**, 093303 (2006).
[89] M. C. Simon, Diplomarbeit, TU Wien, (2006), unpublished
[90] J. R. Crespo López-Urrutia, B. Bapat, I. Draganić, B. Feuerstein, D. Fischer, H. Lörch, R. Moshammer, J. Ullrich, R. D. DuBois, and Y. Zou, Hyperfine Interactions **146-147**, 109 (2003).
[91] E. Steinbauer, private communication, 2010
[92] F. Aumayr, G. Lakits, and H. Winter, Applied Surface Science **47**, 139.
[93] O. Benka, A. Schinner, and T. Fink, Physical Review A **51**, 2281 (1995).
[94] V. Bernigaud, O. Kamalou, A. Lawicki, M. Capron, R. Maisonny, B. Manil, L. Maunoury, J. Rangama, P. Rousseau, J.-Y. Chesnel, L. Adoui, and B. A. Huber, Bulletin de l'Observatoire Astronomique de Belgrade **84**, 3 (2008).
[95] A. Duvenbeck, and A. Wucher, Physical Review B (Condensed Matter and Materials Physics) **72**, 165408 (2005).
[96] A. Arnau, F. Aumayr, P. M. Echenique, M. Grether, W. Heiland, J. Limburg, R. Morgenstern, P. Roncin, S. Schippers, R. Schuch, N. Stolterfoht, P. Varga, T. J. M. Zouros, and H. P. Winter, Surface Science Reports **27**, 113 (1997).
[97] F. Aumayr, and H. Winter, e-Journal of Surface Science and Nanotechnology **1**, 171 (2003).
[98] T. Schenkel, A. V. Hamza, A. V. Barnes, and D. H. Schneider, Progress in Surface Science **61**, 23 (1999).
[99] F. Aumayr, A. S. El-Said, and W. Meissl, Nuclear Instruments and Methods in Physics Research Section B: Beam Interactions with Materials and Atoms **266**, 2729 (2008).
[100] S. Facsko, R. Heller, A. S. El-Said, W. Meissl, and F. Aumayr, Journal of Physics: Condensed Matter **21**, 224012 (2009).
[101] W. Meissl, M. C. Simon, J. R. Crespo LÛpez-Urrutia, H. Tawara, J. Ullrich, H. P. Winter, and F. Aumayr, Nuclear Instruments and Methods in Physics Research Section B: Beam Interactions with Materials and Atoms **256**, 520 (2007).
[102] J. Burgdörfer, P. Lerner, and F. W. Meyer, Physical Review A **44**, 5674 (1991).
[103] J. Burgdörfer, and C. Lemell, *Theoretical Concepts and Methods for Electron Emission from Solid Surfaces* (Springer Berlin / Heidelberg, 2007), Vol. Volume 225.
[104] H. Winter, and F. Aumayr, Journal of Physics B-Atomic Molecular and Optical Physics **32**, R39 (1999).
[105] R. Morgenstern, and J. Das, Europhysics News **25**, 3 (1994).
[106] H. Winter, and F. Aumayr, Europhysics News **33**, 215 (2002).
[107] A. S. El-Said, R. Heller, W. Meissl, R. Ritter, S. Facsko, C. Lemell, B. Solleder, I. C. Gebeshuber, G. Betz, M. Toulemonde, W. Möller, J. Burgdörfer, and F. Aumayr, Physical Review Letters **100**, 237601 (2008).
[108] A. S. El-Said, W. Meissl, M. C. Simon, J. R. Crespo Lopez-Urrutia, I. C. Gebeshuber, M. Lang, H. P. Winter, J. Ullrich, and F. Aumayr, Nuclear Inst. and Methods in Physics Research B **256**, 346 (2007).
[109] A. S. El-Said, W. Meissl, M. C. Simon, J. R. Crespo Lopez-Urrutia, C. Lemell, J. Burgdörfer, I. C. Gebeshuber, H. P. Winter, J. Ullrich, C. Trautmann, M. Toulemonde, and F. Aumayr, Nuclear Inst. and Methods in Physics Research B **258**, 167 (2007).
[110] C. Lemell, A. S. El-Said, W. Meissl, I. C. Gebeshuber, C. Trautmann, M. Toulemonde, J. Burgdörfer, and F. Aumayr, Solid State Electronics **51**, 1398 (2007).

[111] R. Heller, S. Facsko, R. A. Wilhelm, and W. Möller, Physical Review Letters **101**, 096102 (2008).
[112] L. Porte, C. H. de Villeneuve, and M. Phaner, Journal of Vacuum Science & Technology B: Microelectronics and Nanometer Structures **9** (1991).
[113] L. Porte, M. Phaner, C. H. de Villeneuve, N. Moncoffre, and J. Tousset, Nuclear Instruments & Methods in Physics Research Section B-Beam Interactions with Materials and Atoms **44**, 116 (1989).
[114] R. Coratger, A. Claverie, A. Chahboun, V. Landry, F. Ajustron, and J. Beauvillain, Surface Science **262**, 208 (1992).
[115] K. Mochiji, S. Yamamoto, H. Shimizu, S. Ohtani, T. Seguchi, and N. Kobayashi, Journal of Applied Physics **82**, 6037 (1997).
[116] G. Hayderer, S. Cernusca, M. Schmid, P. Varga, H. Winter, and F. Aumayr, Physica Scripta **T92**, 156 (2001).
[117] J. R. Hahn, and H. Kang, Physical Review B - Condensed Matter and Materials Physics **60**, 6007 (1999).
[118] T. Meguro, A. Hida, M. Suzuki, Y. Koguchi, H. Takai, Y. Yamamoto, K. Maeda, and Y. Aoyagi, Applied Physics Letters **79**, 3866 (2001).
[119] E. Sideras-Haddad, T. Schenkel, S. Shrivastava, T. Makgato, A. Batra, C. D. Weis, A. Persaud, R. Erasmus, and B. Mwakikunga, Nuclear Instruments and Methods in Physics Research Section B: Beam Interactions with Materials and Atoms **267**, 2774 (2009).
[120] N. Nakamura, M. Terada, Y. Nakai, Y. Kanai, S. Ohtani, K. I. Komaki, and Y. Yamazaki, Nuclear Instruments and Methods in Physics Research, Section B: Beam Interactions with Materials and Atoms **232**, 261 (2005).
[121] M. Terada, N. Nakamura, Y. Nakai, Y. Kanai, S. Ohtani, K. I. Komaki, and Y. Yamazaki, Nuclear Instruments and Methods in Physics Research, Section B: Beam Interactions with Materials and Atoms **235**, 452 (2005).
[122] B. An, S. Fukuyama, K. Yokogawa, and M. Yoshimura, Japanese Journal of Applied Physics, Part 1: Regular Papers and Short Notes and Review Papers **39**, 3732 (2000).
[123] R. Minniti, L. P. Ratliff, and J. D. Gillaspy, Phys. Scripta **T92**, 22 (2001).
[124] M. Tona, H. Watanabe, S. Takahashi, Y. Fujita, T. Abe, S. Jian, N. Nakamura, N. Yoshiyasu, C. Yamada, M. Sakurai, and S. Ohtani, Journal of Physics: Conference Series **58**, 331 (2007).
[125] Z. G. Wang, C. Dufour, S. Euphrasie, and M. Toulemonde, Nuclear Instruments and Methods in Physics Research, Section B: Beam Interactions with Materials and Atoms **209**, 194 (2003).
[126] H. Ogiso, W. Mizutani, S. Nakano, H. Tokumoto, and K. Yamanaka, Applied Physics A: Materials Science Processing **66**, 1155 (1998).
[127] D. C. Parks, R. Bastasz, R. W. Schmieder, and M. Stockli, Journal of Vacuum Science & Technology B: Microelectronics and Nanometer Structures **13**, 941 (1995).
[128] T. Hagen, S. Grafstrom, J. Ackermann, R. Neumann, C. Trautmann, J. Vetter, and N. Angert, Journal of Vacuum Science & Technology B: Microelectronics and Nanometer Structures **12**, 1555 (1994).
[129] S. Grafström, J. Ackermann, T. Hagen, R. Neumann, and O. Probst, Journal of Vacuum Science & Technology B: Microelectronics and Nanometer Structures **12**, 1559 (1994).
[130] C. A. Vasko, Diplomarbeit, TU Wien, (2009), unpublished
[131] J. D. Gillaspy, D. C. Parks, and L. P. Ratliff, Journal of Vacuum Science & Technology B: Microelectronics and Nanometer Structures **16**, 3294 (1998).
[132] R. M. Papaléo, M. R. Silva, R. Leal, P. L. Grande, M. Roth, B. Schattat, and G. Schiwietz, Physical Review Letters **101**, 167601 (2008).
[133] IMS. Homepage of IMS Nanofabrication AG. 2011; Available from: http://www.ims.co.at/.
[134] F. Grossmann, R. Heller, M. Kreller, U. Kentsch, S. Landgraf, V. P. Ovsyannikov, M. Schmidt, F. Ullmann, and G. Zschornack, Nuclear Instruments and Methods in Physics Research Section B: Beam Interactions with Materials and Atoms **256**, 565 (2007).
[135] S. Gumpenberger, Bachelor Thesis, TU Wien, (2009), unpublished
[136] N. Stolterfoht, J. H. Bremer, V. Hoffmann, R. Hellhammer, D. Fink, A. Petrov, and B. Sulik, Physical Review Letters **88** (2002).
[137] Y. Yamazaki, Nuclear Instruments and Methods in Physics Research Section B: Beam Interactions with Materials and Atoms **193**, 516 (2002).
[138] S. Ninomiya, Y. Yamazaki, F. Koike, H. Masuda, T. Azuma, K. Komaki, K. Kuroki, and M. Sekiguchi, Physical Review Letters **78**, 4557 (1997).
[139] Y. Yamazaki, Nuclear Instruments and Methods in Physics Research Section B: Beam Interactions with Materials and Atoms **258**, 139 (2007).
[140] K. Schiessl, W. Palfinger, K. Tőkési, H. Nowotny, C. Lemell, and J. Burgdörfer, Physical Review A **72** (2005).
[141] K. Schiessl, W. Palfinger, C. Lemell, and J. Burgdorfer, Nuclear Instruments and Methods in Physics Research Section B: Beam Interactions with Materials and Atoms **232**, 228 (2005).

[142] G. P. Pokhil, K. A. Vokhmyanina, and A. I. Mironchik, Journal of Surface Investigation. X-ray, Synchrotron and Neutron Techniques **3**, 326 (2009).
[143] G. P. Pokhil, K. A. Vokhmyanina, L. A. Zhilyakov, T. Ikeda, Y. Kanai, Y. Iwai, T. M. Kojima, and Y. Yamazaki, Bulletin of the Russian Academy of Sciences: Physics **72**, 638 (2008).
[144] N. Stolterfoht, V. Hoffmann, R. Hellhammer, Z. Pei, D. Fink, A. Petrov, and B. Sulik, Nuclear Instruments and Methods in Physics Research Section B: Beam Interactions with Materials and Atoms **203**, 246 (2003).
[145] N. Stolterfoht, R. Hellhammer, Z. D. Pesic, V. Hoffmann, J. Bundesmann, A. Petrov, D. Fink, and B. Sulik, Vacuum **73**, 31 (2004).
[146] Y. Iwai, Y. Kanai, Y. Nakai, T. Ikeda, H. Oyama, K. Ando, H. Masuda, K. Nishio, M. Nakao, and H. A. Torii, Nuclear Instruments and Methods in Physics Research Section B: Beam Interactions with Materials and Atoms **205**, 762 (2003).
[147] Y. Morishita, Y. Kanai, K. Ando, R. Hutton, T. Brage, H. A. Torii, K. Komaki, H. Masuda, K. Ishii, and F. B. Rosmej, Nuclear Instruments and Methods in Physics Research Section B: Beam Interactions with Materials and Atoms **205**, 758 (2003).
[148] K. Tökési, L. Wirtz, C. Lemell, and J. Burgdörfer, Nuclear Instruments and Methods in Physics Research Section B: Beam Interactions with Materials and Atoms **164-165**, 504 (2000).
[149] N. Stolterfoht, R. Hellhammer, Z. D. Pesic, V. Hoffmann, J. Bundesmann, A. Petrov, D. Fink, B. Sulik, M. Shah, K. Dunn, J. Pedregosa, and R. W. McCullough, Nuclear Instruments and Methods in Physics Research Section B: Beam Interactions with Materials and Atoms **225**, 169 (2004).
[150] C. Lemell, K. Schiessl, H. Nowotny, and J. Burgdorfer, Nuclear Instruments and Methods in Physics Research Section B: Beam Interactions with Materials and Atoms **256**, 66 (2007).
[151] N. Stolterfoht, R. Hellhammer, J. Bundesmann, D. Fink, Y. Kanai, M. Hoshino, T. Kambara, T. Ikeda, and Y. Yamazaki, Physical Review A **76** (2007).
[152] R. T. R. Kumar, X. Badel, G. Vikor, J. Linnros, and R. Schuch, Nanotechnology **16**, 1697 (2005).
[153] M. Sahana, P. Skog, G. Vikor, R. Kumar, and R. Schuch, Physical Review A **73** (2006).
[154] F. Allen, A. Persaud, S. Park, A. Minor, M. Sakurai, D. Schneider, and T. Schenkel, Nuclear Instruments and Methods in Physics Research Section B: Beam Interactions with Materials and Atoms **244**, 323 (2006).
[155] S. Mátéfi-Tempfli, M. Mátéfi-Tempfli, L. Piraux, Z. Juhász, S. Biri, É. Fekete, I. Iván, F. Gáll, B. Sulik, G. Víkor, J. Pálinkás, and N. Stolterfoht, Nanotechnology **17**, 3915 (2006).
[156] P. Skog, I. Soroka, A. Johansson, and R. Schuch, Nuclear Instruments and Methods in Physics Research Section B: Beam Interactions with Materials and Atoms **258**, 145 (2007).
[157] R. Hellhammer, J. Bundesmann, D. Fink, and N. Stolterfoht, Nuclear Instruments and Methods in Physics Research Section B: Beam Interactions with Materials and Atoms **258**, 159 (2007).
[158] N. Stolterfoht, R. Hellhammer, J. Bundesmann, and D. Fink, Physical Review A **77** (2008).
[159] N. Stolterfoht, R. Hellhammer, Z. Juhász, B. Sulik, V. Bayer, C. Trautmann, E. Bodewits, A. de Nijs, H. Dang, and R. Hoekstra, Physical Review A **79** (2009).
[160] J. Frenkel, Physical Review **54**, 647 (1938).
[161] Y. Kanai, M. Hoshino, T. Kambara, T. Ikeda, R. Hellhammer, N. Stolterfoht, and Y. Yamazaki, Physical Review A **79** (2009).
[162] P. Skog, H. Q. Zhang, and R. Schuch, Physical Review Letters **101** (2008).
[163] N. Stolterfoht, R. Hellhammer, D. Fink, B. Sulik, Z. Juhász, E. Bodewits, H. Dang, and R. Hoekstra, Physical Review A **79** (2009).
[164] Z. Juhász, B. Sulik, R. Rácz, S. Biri, R. J. Bereczky, K. Tökési, A. Kövér, J. P.´s, and N. Stolterfoht, Physical Review A **82** (2010).
[165] H.-Q. Zhang, P. Skog, and R. Schuch, Physical Review A **82** (2010).
[166] Z. Juhasz, B. Sulik, S. Biri, I. Ivan, K. Tokesi, E. Fekete, S. Matefitempfli, M. Matefitempfli, G. Vikor, and E. Takacs, Nuclear Instruments and Methods in Physics Research Section B: Beam Interactions with Materials and Atoms **267**, 321 (2009).
[167] N. Stolterfoht, R. Hellhammer, J. Bundesmann, and D. Fink, Nuclear Instruments and Methods in Physics Research Section B: Beam Interactions with Materials and Atoms **267**, 226 (2009).
[168] K. Schiessl, W. Palfinger, K. Tokesi, H. Nowotny, C. Lemell, and J. Burgdorfer, Nuclear Instruments and Methods in Physics Research Section B: Beam Interactions with Materials and Atoms **258**, 150 (2007).
[169] N. Stolterfoht, R. Hellhammer, Z. J.´sz, B. Sulik, E. Bodewits, H. M. Dang, and R. Hoekstra, Physical Review A **82** (2010).
[170] R. Hellhammer, Z. D. Pešic, P. Sobocinski, D. Fink, J. Bundesmann, and N. Stolterfoht, Nuclear Instruments and Methods in Physics Research Section B: Beam Interactions with Materials and Atoms **233**, 213 (2005).
[171] M. Fürsatz, W. Meissl, S. Pleschko, I. C. Gebeshuber, N. Stolterfoht, H. Winter, and F. Aumayr, Journal of Physics: Conference Series **58**, 319 (2007).

[172] R. Hellhammer, P. Sobocinski, Z. Pesic, J. Bundesmann, D. Fink, and N. Stolterfoht, Nuclear Instruments and Methods in Physics Research Section B: Beam Interactions with Materials and Atoms **232**, 235 (2005).
[173] N. Stolterfoht, R. Hellhammer, Z. Pesic, V. Hoffmann, J. Bundesmann, A. Petrov, D. Fink, and B. Sulik, Surface and Coatings Technology **196**, 389 (2005).
[174] G. Víkor, R. T. R. kumar, Z. D. Pešic̀, N. Stolterfoht, and R. Schuch, Nuclear Instruments and Methods in Physics Research Section B: Beam Interactions with Materials and Atoms **233**, 218 (2005).
[175] T. Ikeda, Y. Kanai, T. M. Kojima, Y. Iwai, T. Kambara, Y. Yamazaki, M. Hoshino, T. Nebiki, and T. Narusawa, Applied Physics Letters **89**, 163502 (2006).
[176] T. Nebiki, D. Sekiba, H. Yonemura, M. Wilde, S. Ogura, H. Yamashita, M. Matsumoto, K. Fukutani, T. Okano, and J. Kasagi, Nuclear Instruments and Methods in Physics Research Section B: Beam Interactions with Materials and Atoms **266**, 1324 (2008).
[177] A. Cassimi, L. Maunoury, T. Muranaka, B. Huber, K. R. Dey, H. Lebius, D. Lelièvre, J. M. Ramillon, T. Been, and T. Ikeda, Nuclear Instruments and Methods in Physics Research Section B: Beam Interactions with Materials and Atoms **267**, 674 (2009).
[178] R. Nakayama, M. Tona, N. Nakamura, H. Watanabe, N. Yoshiyasu, C. Yamada, A. Yamazaki, S. Ohtani, and M. Sakurai, Nuclear Instruments and Methods in Physics Research Section B: Beam Interactions with Materials and Atoms **267**, 2381 (2009).
[179] M. Kreller, G. Zschornack, and U. Kentsch, Nuclear Instruments and Methods in Physics Research Section B: Beam Interactions with Materials and Atoms **269**, 1032 (2011).
[180] T. Ikeda, Y. Kanai, T. M. Kojima, Y. Iwai, Y. Kanazawa, M. Hoshino, T. Kobayashi, G. P. Pokhil, and Y. Yamazaki, Journal of Physics: Conference Series **88**, 012031 (2007).
[181] A. Milosavljević, G. Víkor, Z. Pešić, P. Kolarž, D. Šević, B. Marinković, S. Mátéfi-Tempfli, M. Mátéfi-Tempfli, and L. Piraux, Physical Review A **75** (2007).
[182] S. Das, B. Dassanayake, M. Winkworth, J. Baran, N. Stolterfoht, and J. Tanis, Physical Review A **76** (2007).
[183] B. S. Dassanayake, S. Das, R. J. Bereczky, Todblack, eacute, K. si, and J. A. Tanis, Physical Review A **81**, 020701 (2010).
[184] K. Schiessl, K. Tőkési, B. Solleder, C. Lemell, and J. Burgdörfer, Physical Review Letters **102** (2009).
[185] A. R. Milosavljević, J. Jureta, G. Víkor, Z. D. Pešić, D. Šević, M. Mátéfi-Tempfli, S. Mátéfi-Tempfli, and B. P. Marinković, EPL (Europhysics Letters) **86**, 23001 (2009).
[186] B. S. Dassanayake, R. J. Bereczky, S. Das, A. Ayyad, K. Tökési, and J. A. Tanis, Physical Review A **83** (2011).
[187] P. Skog, H. Q. Zhang, N. Akram, I. L. Soroka, C. Trautmann, and R. Schuch, Journal of Physics: Conference Series **194**, 132030 (2009).
[188] G. Sun *et al.*, Physical Review A **79** (2009).
[189] L. Chen, X. Lv, J. Jia, M. Ji, P. Zhou, G. Sun, J. Wang, Y. Chen, F. Xi, Y. Cui, J. Shao, X. Qiu, Y. Guo, and X. Chen, Journal of Physics B: Atomic, Molecular and Optical Physics **44** (2011).
[190] RoentDek. 2011; Available from: http://www.roentdek.com.
[191] KMax. 2008; Available from: http://www.sparrowcorp.com/.
[192] I. Pro. IGOR Pro 6.0. 2010; Available from: http://www.wavemetrics.com.
[193] Duran. 2011; Available from: http://www.duran-group.com.
[194] G. Kowarik, R. J. Bereczky, C. Lemell, J. Burgdörfer, and F. Aumayr, to be published (2011).
[195] DIN IEC 93, Prüfverfahren für Elektroisolierstoffe - Spezifischer Durchgangswiderstand und spezifischer Oberflächenwiderstand von festen, elektrisch isolierenden Werkstoffen, 1983
[196] J. Waclawek, Projektarbeit, TU Wien, (2011), unpublished
[197] A. K. Jonscher, Journal of Physics D: Applied Physics **32**, R57 (1999).
[198] P. Love, Journal of Physics C: Solid State Physics **16**, 5985 (1983).
[199] Mylar - Product Information. 2011; Available from: http://usa.dupontteijinfilms.com/informationcenter/downloads/Electrical_Properties.pdf.
[200] Y. Yamazaki, *Book of Abstracts* (HCI-15, Shanghai, 2010).